Impurity Transport Study by means of Tracer-Encapsulated Pellet Injection

Konstantin V. Khlopenkov

Thesis for the degree of

Doctor of Philosophy

Department of Fusion Science

School of Mathematical and Physical Science

The Graduate University for Advanced Studies

1998

Abstract

Understanding of the heat and particle transport processes is highly important since it determines the feasibility of controlled fusion. The particle transport in plasma can be analyzed by observing the motion of impurity ions introduced artificially into plasma, which are different species from the main plasma ions. This can be done by impurity pellet injection when the source profile of the impurity is created along t path of the pellet ablation. The pellet should be made of a low-Z material such as lithium in order to provide a fast and complete ionization of the injected impurity. This essentially simplifies the calculations as the source term in the particle balance equation can be neglected.

Experiments with Li pellet injection into Heliotron E plasmas have brought important information about main characteristics of Li ions during the pellet ablation and also about the transport properties of Li ions after the injection. The transport coefficients have been calculated by simulating the experimental data by means of the impurity transport code, taking into account the impurity puffing from the wall and the impurity recycling. However, because of the non-local initial source of lithium ions, there is no clear transient process to analyze and the transport task requires an account of a variety of factors.

As an accurate diagnostic for local particle transport, a new method of TECPEL (tracer-encapsulated cryogenic pellet) injection is proposed, which provides reliable information about transport in plasmas without the need for complex measurements of all the plasma parameters. With this method, the local transport is measured directly by observing evolution of a small particle source as tracer, which is initially localized within a limited plasma volume. The tracer particles are deposited locally by the TECPEL, which consists of a small core as the tracer of a light atom and the major outer layer of a frozen hydrogen isotope. When such a pellet enters the plasma, the outer layer is ablated first, which allows the tracer core to reach the central plasma region with a higher temperature. This results in a more intensive ablation of the core providing the necessary localization of the deposited tracer ions. It is shown that in this case, the diffusion coefficient can be calculated analytically from experimentally observed evolution of the impurity density.

A device for production and acceleration of tracer-encapsulated cryogenic pellet has been constructed and tested experimentally. For a technical demonstration of the device operation, a 240 μm diameter carbon sphere is encapsulated in a ∅3×3 mm cylindrical hydrogen pellet. The accelerated TECPEL is photographed from two perpendicular directions simultaneously. From the obtained images, the 3D geometry of TECPEL has been reconstructed and found to be consistent with the projected

dimensions. Thus, the proof-of-principle of the device operation has been successfully demonstrated.

As application for the existing fusion devices with a medium size plasma, an alternative configuration of the pellet made of non-cryogenic materials has been proposed. The idea of the tracer-encapsulated solid pellet (TESPEL) injection will be still advantageous if the emission of the core ions can be observed on the background emission of the major pellet ions. From various TESPEL configurations tested, the most appropriate one has been selected in the form of a polystyrene shell (300μm diameter and 50 μm wall thickness) containing a lithium hydride core (50 μm diameter). This configuration has been experimentally realized and the produced TESPEL shave been successfully accelerated with conservation of the TESPEL's integrity. Calculation of the TESPEL ablation rate has demonstrated that the obtained TESPEL dimensions and achieved pellet velocities are appropriate for injection into a medium size plasma.

For proving the essential concept of the new diagnostic method, a series of experiments with TESPEL injection has been carried out for the case of CHS plasmas. The light emission from the ablating pellet is registered in H_α and Li I (or Li II) lines with high time resolution, and the spatial resolution is provided by the CCD photography. From these measurements, the information is obtained about the exact location and width of the deposition of tracer material, and this confirmed that a good localization of the tracer has been achieved. The experimentally measured TESPEL ablation rate is compared with the calculation based on the impurity pellet ablation model, and a good agreement has been found.

Behavior of the tracer ions deposited locally in the core plasma region was observed by CXRS method using the heating neutral beam as a source of neutral atoms for the charge-exchange reaction with Li^{3+} ions. The observed diffusion was found to be consistent with the theoretical calculations, and the experimental data have been simulated by means of the impurity transport code for obtaining the transport coefficients. The difference in the diffusion coefficient for various plasma configurations is discussed.

Thus, a new diagnostic method for particle transport study with TESPEL has been experimentally implemented for the first time. The results from CHS have proved the new diagnostic concept from the both viewpoints of the production method of a tracer-encapsulated pellet and observation of the transport properties of the tracer particles.

Table of Contents

1. INTRODUCTION

1.1. Importance of transport measurement

One of the most important properties of plasmas in magnetic confinement devices is the plasma transport. The characteristic times of particles and heat conservation or, simply, the plasma confinement is merely determined by the transport processes. The physics of the plasma transport is far from being established and still remains an important subject to be understood. The clarification of the mechanism itself is an interesting challenge for theoretical physics. Recently, however, an understanding of the transport has become critical mainly from the practical point of view. For t reliable design of an appropriate fusion machine or even a commercial reactor, prediction of its plasma confinement based on an accurate knowledge of the plasma transport becomes crucial.

Based on widely observed scaling laws, a longer confinement time can be achieved with a larger size of the plasma. Thus, the apparent way to ensure the performance of a designed reactor is to make the designed parameters such as the plasma volume, the magnetic field strength, and the heating power as large as possible. Recently, this path became hard to follow because of a new era of huge machines like ITER. The design and construction of the first experimental thermonuclear reactor is going to absorb funds from several industrial countries to cover the total estimated costs of $10 billion. Besides the financial difficulties, the ITER project is not universally popular among scientists, and this is due partly to some doubts that the machine will provide the required plasma confinement and can reach the expected power output. So, the plasma transport has to be clarified not only for the plasma theory but also from the viewpoint of practical reactor construction, so as to provide much improved accuracy in the machine design.

The variety of theoretical models of the plasma transport can hardly explain the experimentally observed phenomena. At the same time, lack of accurate experimental information makes the analysis of transport very complicated. There are many methods of transport analysis based on experimental data, and some of them will be reviewed in the following section.

In this work a new method is proposed as an accurate diagnostic for particle transport. It provides reliable information about transport in plasmas without the need for complex measurements of all the plasma parameters.

Before coming to the details of this new method, let us briefly review the general principles of the existing methods of studying plasma transport.

1.2. Common methods of studying transport in plasmas

Methods of studying the transport phenomena in plasmas can be classified as static and dynamic. The static methods are based on the consideration of the stationary balance equations, while the dynamic methods employ the analysis of the transient phenomena. Both approaches have their own advantages, which will be discussed below.

A general static method considers the reverse task solution for the system of transport equations averaged on the magnetic surface with radius r [1-3]:

$$\frac{\partial n}{\partial t}+\frac{1}{r}\frac{\partial}{\partial r}r\Gamma_n = S \tag{1.1}$$

$$\frac{3}{2}\frac{\partial}{\partial t}(nT_e)+\frac{1}{r}\frac{\partial}{\partial r}r\left(q_e+\frac{5}{2}T_e\Gamma_n\right)-\frac{\Gamma_n}{n}\frac{\partial}{\partial r}(nT_e)=Q_{OH}+P_e-Q_{ei}+Q_e \tag{1.2}$$

$$\frac{3}{2}\frac{\partial}{\partial t}(nT_i)+\frac{1}{r}\frac{\partial}{\partial r}r\left(q_i+\frac{5}{2}T_i\Gamma_n\right)-\frac{\Gamma_n}{n}\frac{\partial}{\partial r}(nT_i)=P_i+Q_{ei}+Q_i \tag{1.3}$$

where n is plasma density; Γ_n – particle flux; S – particle source; T_e and T_i – electron and ion temperatures; q_e and q_i – electron and ion heat fluxes; Q_{OH} – ohmic heating power (if present); P_e and P_i – additional heating power for electrons and ions (if present); Q_{ei} – heat exchange between electrons and ions; Q_e and Q_i – other heat sources and sinks for electrons and ions. Equation(1.1) is a particle balance equation and equations(1.2), (1.3) are electron and ion heat balance equations, respectively. The particle and heat fluxes are determined through the density and temperature gradients, respectively, with transport coefficients as proportionality coefficients:

$$\Gamma_n = -D\frac{\partial n}{\partial r}-nV, \tag{1.4}$$

$$q_e = -\kappa_e\frac{\partial T_e}{\partial r}=-\chi_e n\frac{\partial T_e}{\partial r}, \tag{1.5}$$

$$q_i = -\kappa_i\frac{\partial T_i}{\partial r}\equiv-\chi_i n\frac{\partial T_i}{\partial r}, \tag{1.6}$$

where D and V are diffusion coefficient and pinch velocity, $\kappa_{e,i}$, $\chi_{e,i}$ – heat and temperature conductivity for electrons and ions.

The equations (1.1)–(1.3) are written in the approximation of the cylindrical geometry, assuming axial symmetry and neglecting the inertia and viscosity of ions and electrons. The system of equations (1.1)–(1.3) can be completed with Ohmic law and Maxwell equations if the electric current density is also a subject of the calculation.

Solution of the defined set of the equations is aimed at the determination of the transport coefficients D, V, χ_e, χ_i, which describe the transport in plasma and, in general, define the plasma confinement. This task can be fulfilled by means of direct simulation of the equations (1.1)–(1.3) assuming some specific values for the transport coefficients and comparing the simulated evolution of n, T_e, T_i with the experimental data. The correct expressions for the transport coefficients are resolved by adjusting the input values and achieving the best agreement with the experimental data.

Although the simulation of the full system of equations (1.1)–(1.3) is possible, it is rather complicated and often not necessary. Therefore the above equations need to be simplified further for particular plasma conditions. One of the common simplifications can be made from the following relation observed experimentally:

$$\chi_e >> \chi_i . \tag{1.7}$$

This allows to consider electron and ion heat transport independently or simply focus only on the electron heat balance equation (1.2).

For the stationary plasma conditions, the time derivatives can be neglected (which is an advantage of the static methods) and, assuming zero particle source S (for the core plasma), the particle balance (1.1) gives zero particle flux Γ_n. Thus, equation (1.2) becomes much simplified:

$$\frac{1}{r}\frac{\partial}{\partial r}\left(r\chi_e^{PB} n \frac{\partial T_e}{\partial r} \right) = Q_{OH} + P_e - Q_{ei} + Q_e \tag{1.8}$$

Here χ_e^{PB} denotes electron temperature conductivity derived from the power balance. The accurate consideration of this equation requires information about stationary profiles for not only density and temperature, but also for all terms in the right-hand side of the equation. Thus, the experimental data on the profiles of the ion temperature, absorbed power of the additional heating, radiation losses, etc. should be available. This is a weak point of the static methods of the transport analysis, since the reliable measurement of all these parameters is often complicated or not possible.

Because of the difficulties with application of the static methods, recently the dynamic methods become widely used for studying the transport phenomena. Dynamic methods are applicable when considering the time evolution of the perturbation of a plasma parameter (such as density or temperature). The magnitude of the perturbation should be large enough for the higher signal/noise ratio, but much smaller than the magnitude of the parameter in equilibrium state, so as to assume that

the static terms in the balance equations remain unchanged. Then the electron temperature can be written as a sum of the two parts: the unperturbed profile and the changing perturbation:

$$T_e(r,t) = T_{e0}(r) + \tilde{T}_e(r,t) \tag{1.9}$$

After substituting this to the equation (1.2) one can obtain a more simplified equation for the perturbed component:

$$\frac{3}{2}\frac{\partial}{\partial t}\left(n\tilde{T}_e\right) = \frac{1}{r}\frac{\partial}{\partial r}\left(r n \chi_e \frac{\partial \tilde{T}_e}{\partial r}\right) \tag{1.10}$$

(We neglect here the terms that are weaker than the dominant term with the second derivative of $\tilde{T}_e$.)

Now the problem is limited to solving the equation (1.10) with a given initial profile $\tilde{T}_e(r,0)$. Note, that Eq. (1.10) is defined within a factor of the absolute value of $\tilde{T}_e$ that means that the absolute value of the temperature is not significant and only the measurement of the relative change is necessary. This is typical for the dynamic methods and advantageous comparing to the static methods, since the absolute calibration of the experimental data is not required.

There is a variety of the dynamic methods that differ in the origin of the perturbation being studied. Among the first, there were the methods that utilized sawtooth oscillations of the electron temperature [4-7]. An advantage of such methods is the use of the natural source of the perturbation in plasma, i.e. internal disruption, so that there is no need to create the perturbation, but it is only necessary to monitor the change in the temperature profile by using standard diagnostics.

The perturbation $\tilde{T}_e(r,0)$ can be represented as consisting of two parts: negative inside the region $r < r_S$ (r_S is the radius of the sawtooth phase inversion) and positive for $r > r_S$. The temperature conductivity χ_e can be obtained from the time delay of the heat wave propagation at different radii. It is also possible, with some assumptions, to estimate χ_e from the sawtooth oscillation period [4]:

$$\overline{\chi}_e = \frac{3}{2}\frac{r_s^2}{T_{ST}}, \tag{1.11}$$

where T_{ST} is the sawtooth oscillation period and $\overline{\chi}_e$ is the electron temperature conductivity averaged within $r < r_S$.

Another kind of dynamic methods uses additional heating of the plasma as a source of the temperature perturbation [8-10]. In this case there is no perturbation of the plasma density, which is advantageous compared to the sawtooth oscillations, since the electron balance equation can be solved independently.

In case of the pellet injection, there are two simultaneous perturbations: negative for the temperature and positive for the density. Similar to the previous case, it is possible to derive χ_e from the cooling wave propagation, but the process is more

complicated because of the simultaneous change of the electron temperature and plasma density. If the diffusion is slower than the heat conductivity ($D << \chi_e$) then one can analyze the fast temperature change assuming the density quasi constant [11]. Besides this, the current density is also assumed to be unchanged during the short time of heat diffusion (compared to the much longer characteristic time of the current diffusion). If the temperature perturbation is approximated as a negative δ-function then χ_e at the plasma axis can be obtained as [12]

$$\chi_{e0} = \frac{3r_0^2}{8\Delta t} \tag{1.12}$$

where r_0 is a radius of initial perturbation and Δt is the time delay of the cooling wa propagation from $r = r_0$ to $r = 0$. We will consider this routine more in detail in section 1.4.

It is also possible to estimate χ_e from the temperature relaxation during the longer time scale, when the shape of temperature profile has been restored and the magnitude is recovering exponentially [11]. In this case, the characteristic time of the central temperature relaxation τ_{eff} is connected with the energy life time of electrons as

$$\tau_{Ee} = \frac{5}{2}\tau_{eff} \tag{1.13}$$

and the average value of $\overline{\chi}_e$ can be estimated from the following expression

$$\overline{\chi}_e \cong \frac{a_l^2}{4\tau_{Ee}} = \frac{a_l^2}{10\tau_{eff}} \tag{1.14}$$

Regarding the particle transport, from equations (1.1) and (1.4) one can write the following expression:

$$\frac{\partial n}{\partial t} = \frac{1}{r}\frac{\partial}{\partial r} r\left(D\frac{\partial n}{\partial r} + V n\right) + S \tag{1.15}$$

And using the similar substitution for the perturbed component as (1.9)

$$\tilde{n}(r,t) = n(r,t) - n_0(r) \tag{1.16}$$

one can write

$$\frac{\partial \tilde{n}}{\partial t} = \frac{1}{r}\frac{\partial}{\partial r} r\left(D\frac{\partial \tilde{n}}{\partial r} + V\tilde{n}\right) \tag{1.17}$$

Equation (1.17) is very similar to the equation (1.10) and it can be analyzed in the same way as the methods of obtaining χ_e described above.

There is a variety of sources of the density perturbation, but the most common one is the pellet injection [13, 14]. The density evolution is considered in a longer time scale comparing to the heat wave propagation. Using the experimental data of $n(r, t)$ and assuming D and V constant in time it is possible to solve numerically the reverse task of finding the profiles $D(r)$ and $V(r)$ from the equation (1.17) [15, 16]. The accuracy of this procedure becomes low when the left-hand side of the equation

(1.17) is much smaller than the terms on the right, meaning that the density change should be fast enough.

It is important to mention, that in practice the substitution of (1.16) makes sense when the value of the perturbation $\tilde{n}(r,t)$ exceeds the accuracy of the experimental measurement of $n(r, t)$ for the full range of r and t. Furthermore, for a clear separation of the equation (1.17) on the static and dynamic part, the gradient terms in (1.17) should not be much smaller than those in (1.15). In other words, the perturbation $\tilde{n}(r,t)$ should be rather localized.

These conditions are better satisfied when considering the density evolution of impurity ions artificially introduced into the plasma, when the constant component $n_0(r)$ is insignificant. Another advantage of the impurity transport analysis is that it is not directly affected by the fluctuations of the background plasma density (caused by gas puffing, NBI, etc.) if the density of impurity ions is low comparing to the plasma density.

The impurity atoms can be injected into the plasma by means of a laser blow-off method [17]. In this method the blow-off impurities enter the plasma through scrape-off layer, which makes difficult an estimation of the total amount of the injected impurities. Thus, a quantitative analysis is rather complicated although a qualitative observation of the impurity transport is possible.

Impurity pellet injection has also been used to measure the particle transport [18, 19]. This method gives intrinsically a broad source profile of the impurity distribution, which is created along the path of the pellet ablation. This needs also a complicated analysis and accurate experimental measurements of the subsequent evolution of the impurity profile. For the material of impurity pellet, a light atom (like lithium, etc.) is more preferable because of the faster full ionization of its ions at the typical plasma conditions. This results in a very low rate of atomic processes during diffusion, which yields a negligibly small source term S in Eq. (1.15).

In Chapter 2 we shall discuss the experiments with injection of lithium pellets into the plasma of Heliotron E device [20] and present the results of the impurity transport simulation.

Summarizing the review of the methods of transport analysis, it is necessary to emphasize the following:

1) Equations of the particle and heat transport can be analyzed separately if the heat diffusion is faster than the particle diffusion.
2) Static methods of the heat transport analysis are applicable only if the experimental information about all the plasma parameters is available. Dynamic methods require a certain perturbation for the analysis and can be applied to non-calibrated experimental data.
3) In general, the balance equations can be solved only numerically. The analytical

solution requires several assumptions about the plasma parameters and about the form of the initial perturbation.

4) The transport coefficients can be calculated with a higher accuracy when the terms with derivatives are dominant in the balance equations. It means that the perturbation should be fast developing and localized.
5) The particle transport can be measured more correctly by analyzing the evolution of low Z impurity ions artificially introduced into plasma, which are different species from the main plasma ions.

1.3. Concept of Tracer-Encapsulated Pellet Injection

The problem of measuring the particle transport with higher accuracy can be solved by the new method of the tracer-encapsulated pellet injection (also referred to as double-layer pellet injection). The concept of multi-shell pellet for the diagnostics was discussed qualitatively in Reference 21 and a more detailed calculation of the pellet ablation was carried out in Reference 22.

The essential point of the diagnostics is based upon the poloidally and toroidally localized particle source as a tracer within a limited small volume of about $1 cm^3$ in the plasma. The tracer particles are deposited by a tracer-encapsulated cryogenic pellet (TECPEL) which consists of a small core as the tracer of a light atom and the major outer layer of the frozen hydrogen isotope which is the same species as the bulk plasma ions. The ions which are not contained in the plasma intrinsically, such as lithium, can be used for tracing the particle motion.

When such a pellet enters the plasma, the outer layer of hydrogen isotope is ablated first, which allows the TECPEL's core to reach the central plasma region with a higher temperature. This results in a more intensive ablation of the core providing the necessary localization of the deposited tracer ions. Calculation of the pellet penetration and deposition width of the tracer will be discussed later in section 4.2.

The principle of particle transport diagnostics by means of the TECPEL is shown in Fig. 1. At the first stage after injection, the tracer ions will flow approximately along the magnetic field lines being affected by $\vec{E} \times \vec{B}$ drift and other effects. The motion of the tracer ions can be detected by various methods, such as a charge exchange recombination spectroscopy (CXRS) array with high time and spatial resolution at the location of neutral beam used for plasma heating. After a short time, the distribution of the tracer ions equalizes poloidally and toroidally forming an annular domain of particles localized at a certain plasma radius. In a longer time scale,

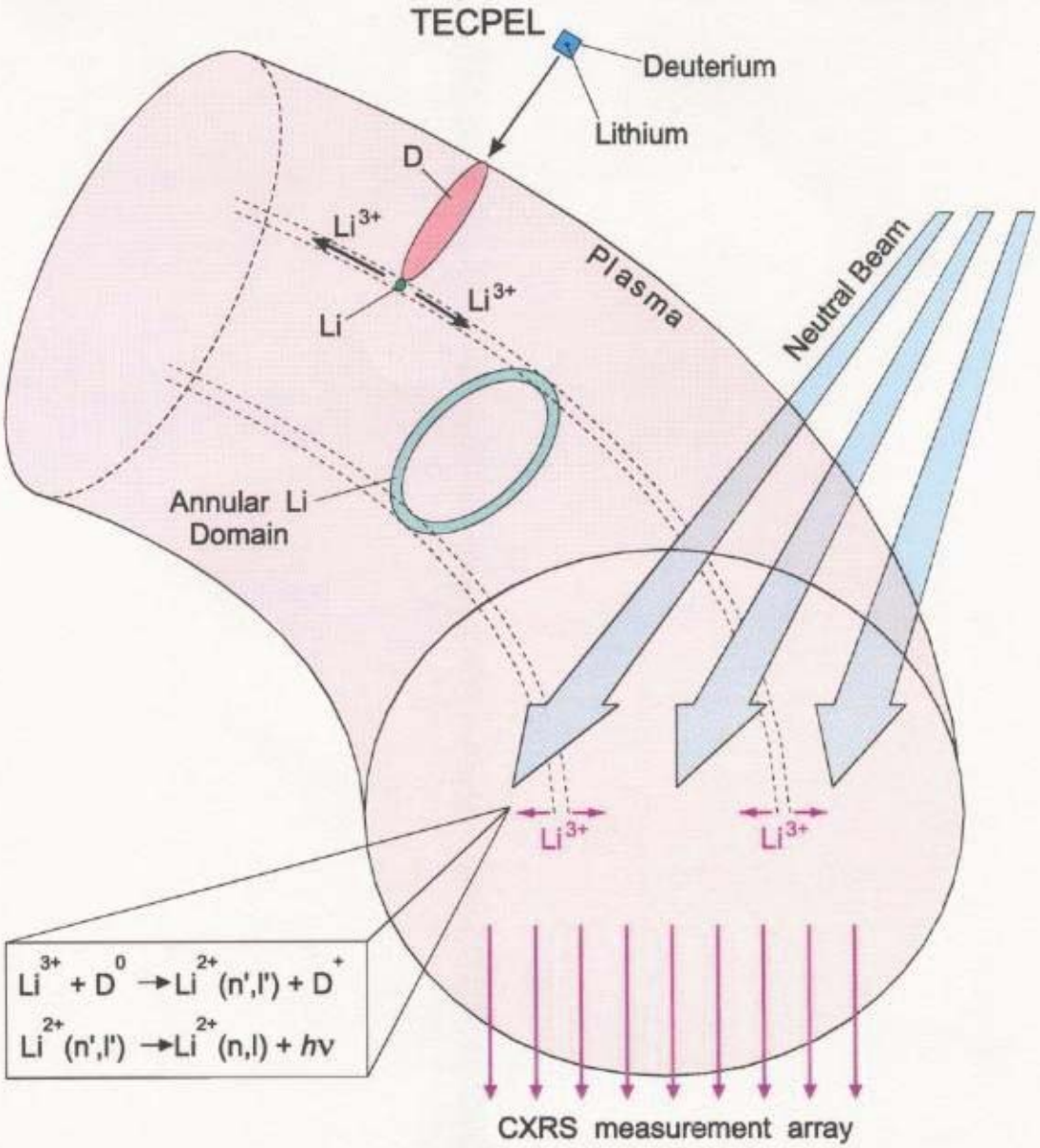

Fig. 1. Schematic view showing the basic principle of particle transport diagnostics by means of a tracer-encapsulated pellet.

particles on such a surface will move inward and outward in radial direction due to the particle diffusion and pinch effect. By monitoring this motion, it is easy to measure accurately the radial transport in post-injection plasma, owing to the very local deposition of the tracer particles. The following two sections explain the method of calculating the diffusion coefficient directly from the observed motion of the deposited tracer ions.

In Chapter 3 we shall describe the process of manufacturing of the TECPEL made of frozen hydrogen with a carbon core and discuss the experiments with the test

acceleration and photographing of TECPEL.

Several alternative configurations of the tracer-encapsulated solid pellet (TESPEL) are reviewed in Chapter 4 and their advantages are compared. In Chapter 5 we shall present the first results of experiments with injection of such pellets into real plasma and discuss the results of impurity transport simulation based on the obtained data.

Now, let us describe the procedure of calculating the diffusion coefficient directly from the observed motion of the deposited tracer ions.

1.4. Calculation of transport coefficients.

As it was mentioned in section 2, the problem of calculating the particle diffusion is reduced to solving the equation

$$\frac{\partial n}{\partial t} = \frac{1}{r}\frac{\partial}{\partial r} r\left(D\frac{\partial n}{\partial r} + V n \right) \tag{1.18}$$

(Here n denotes the density of the tracer ions.)

Initial profile of the deposited tracer ions can be approximated as a δ-function:

$$n(r,0) = N_0\, \delta(r_0) \tag{1.19}$$

where r_0 is the radius where the tracer was deposited and N_0 is a total amount of tracer particles. Suppose that the value of r_0 is known and we are monitoring the change of $n(t)$ at a certain radius r_1.

During some time after injection, $n(r)$ remains peaked and the diffusion term in (1.18) dominates over the term with pinch (as will be shown below), which therefore can be neglected. Within the limited region $r_0 < r < r_1$ we can assume D to be constant or interpret it as averaged in that region. So, the transport equation can be written as

$$\frac{\partial n}{\partial t} = \frac{D}{r}\frac{\partial}{\partial r}\left(r\frac{\partial n}{\partial r} \right) \tag{1.20}$$

It is worth to mention that the heat balance equation (1.10) can also be simplified in the following way. When obtaining expression (1.11) it was assumed [4] that $n \cong \text{const}$ and χ_e was averaged within the considered area, which made possible to take both n and χ_e out of the gradient brackets. In fact, this can be justified with a weaker assumption that $n\chi_e \cong \text{const}$, which is due to the widely observed dependence for the anomalous χ_e (known as Alcator scaling [23]):

$$\chi_e \cong \frac{5\cdot 10^{17}}{n}\ \text{cm}^2\cdot\text{s}^{-1} \tag{1.21}$$

And, assuming that the density is changing much slower than the temperature, we have:

$$\frac{3}{2}\frac{\partial \tilde{T}_e}{\partial t} = \frac{\chi_e}{r}\frac{\partial}{\partial r}\left(r\frac{\partial \tilde{T}_e}{\partial r}\right) \tag{1.22}$$

Now it is dear that equations(1.20) and (1.22) have identical solution if the diffusion D is taken as equivalent to $\frac{2}{3}\chi_e$.

The common solution of the equation (1.20) can be found as [4]:

$$n(r,t) = \frac{N_0}{2Dt}\exp\left(-\frac{r^2}{4Dt}\right)\int_0^{a_r} n(r',0)\exp\left(-\frac{r'^2}{4Dt}\right) I_0\left(\frac{rr'}{2Dt}\right) r'\,dr' \tag{1.23}$$

where $I_0(x)$ is the modified Bessel function.

In general, the integration in this expression can not be carried out analytically, but since the initial profile $n(r, 0)$ is the δ-function, this easily comes to:

$$n(r,t) = \frac{N_0 r_0}{2Dt}\exp\left(-\frac{r^2 + r_0^2}{4Dt}\right) I_0\left(\frac{r r_0}{2Dt}\right) \tag{1.24}$$

Behavior of the function $n(r, t)$ is clarified by Fig. 2, where different curves for various values of r and t are shown. It is seen that the time curve at any radius r achieves the maximum after a certain delay, which is longer for larger r. Such curves

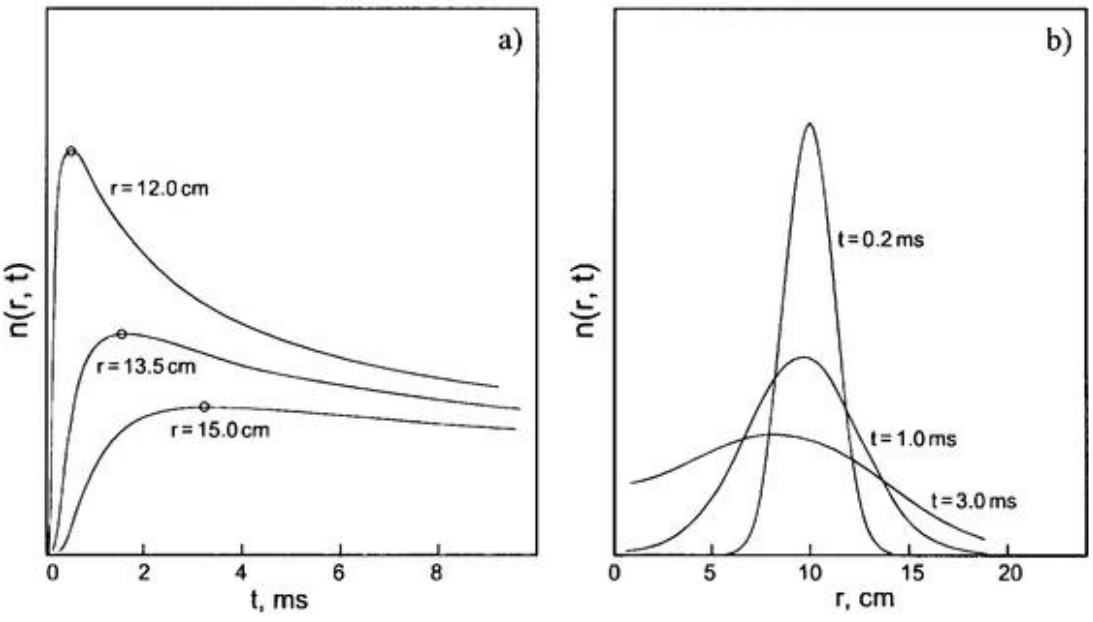

Fig. 2. Different shapes of $n(r, t)$ calculated from (1.24) for $r_0 = 10$ cm and $D = 0.4$ m^2/s. a) Time curves at different radii. Points of maximal values are indicated by small circles. b) Profiles at different moments of time.

can be obtained experimentally if $n(r, t)$ is observed from a set of points with different radial positions.

Although there is always some uncertainty in experimental measurements, the peak of a time dependence can usually be detected easily. Thus, it is of the practical interest to calculate the diffusion coefficient D from the time t of arrival of the density peak to a certain radius r.

Maximum of $n(r, t)$ is achieved when

$$\frac{\partial n}{\partial t} = \frac{N_0 r_0}{8 D^2 t^3} \exp\left(-\frac{r^2 + r_0^2}{4 D t}\right)\left(P(r,t) - Q(r,t)\right) = 0, \tag{1.25}$$

which is equivalent to

$$P(r,t) - Q(r,t) = 0 \tag{1.26}$$

where

$$P(r,t) = \left(r^2 + r_0^2 - 4 D t\right) I_0(x), \tag{1.27}$$

$$Q(r,t) = 2 r r_0 I_1(x) \tag{1.28}$$

and

$$x = \frac{r r_0}{2 D t} \tag{1.29}$$

At this point, we should note that the absolute value of the density (defined by N_0) has no effect on the solution of Eq.(1.26), hence the experimental data of $n(r, t)$ do not need to be calibrated.

It is not possible to transform equation (1.26) so as to express its root directly. The zero-order approximation can be found when $r_0 \to 0$. Then, the Bessel functions $I_1(x) \to 0$ and $I_0(x) \to 1$, and the root of equation (1.26) becomes

$$t_0 = \frac{r^2 + r_0^2}{4 D} \tag{1.30}$$

Since r and r_0 are involved in (1.26) symmetrically, it is approximated with the root t_0 when either $r << r_0$ or $r_0 << r$.

Now we shall find the next order approximation to the root t as a correction to t_0 by expanding (1.26) in a Taylor series around the point t_0:

$$P(t) - Q(t) = P(t_0) - Q(t_0) + (t - t_0)\frac{\partial}{\partial t}\left(P(t) - Q(t)\right)\Big|_{t=t_0} + \ldots \tag{1.31}$$

The left side of this equation as well as $P(t_0)$ is equal to zero. So, after simple transformations one can obtain:

$$t = \alpha(s) t_0 \quad \text{with} \quad \alpha(s) = 1 - \frac{1}{1 - (s - 1/s) I_0(s)/I_1(s)} \tag{1.32}$$

and

$$s = \frac{2 r r_0}{r^2 + r_0^2} \tag{1.33}$$

Now let us consider the other extreme case when $r \to r_0$ that means that the observation point is located very close to the origin of the perturbation. Clearly, in this

case the sought time t will be very small and the parameter x in (1.29) becomes large. For a large argument the Bessel functions have the following approximations:

$$I_0(x)=\frac{e^x}{\sqrt{2\pi x}}\left(1+\frac{1}{8x}+\ldots\right),\quad I_1(x)=\frac{e^x}{\sqrt{2\pi x}}\left(1-\frac{3}{8x}-\frac{5}{27x^2}+\ldots\right) \tag{1.34}$$

(For $I_1(x)$ one extra term was added in expansion (1.34), as it does not complicate the result.) With these substitutions equation (1.26) becomes a quadratic equation for t and can be solved directly:

$$t=\beta(s)t_0, \tag{1.35}$$

$$\beta(s)=\frac{1}{26}\left(135s-27-3\sqrt{3}\sqrt{27-686s+1091s^2}\right) \tag{1.36}$$

Curves for $\alpha(s)$ and $\beta(s)$ are shown in Fig. 3. For $s \ll 1$ (i.e. when r strongly differs from r_0) the function $\alpha(s)$ should be used, while the function $\beta(s)$ is for $s \approx 1$ (i.e. when r is close to r_0). The relative errors (from comparison with numerical solution) e_α and e_β of the approximations $\alpha(s)$ and $\beta(s)$, respectively, are also shown in the lower part of Fig. 3. It is seen, that for all values of parameter s, the error is below 10%, which means that the used approximations are quite appropriate. The largest error is achieved when r differs from r_0 in about two times and $s \approx 0.8$. In

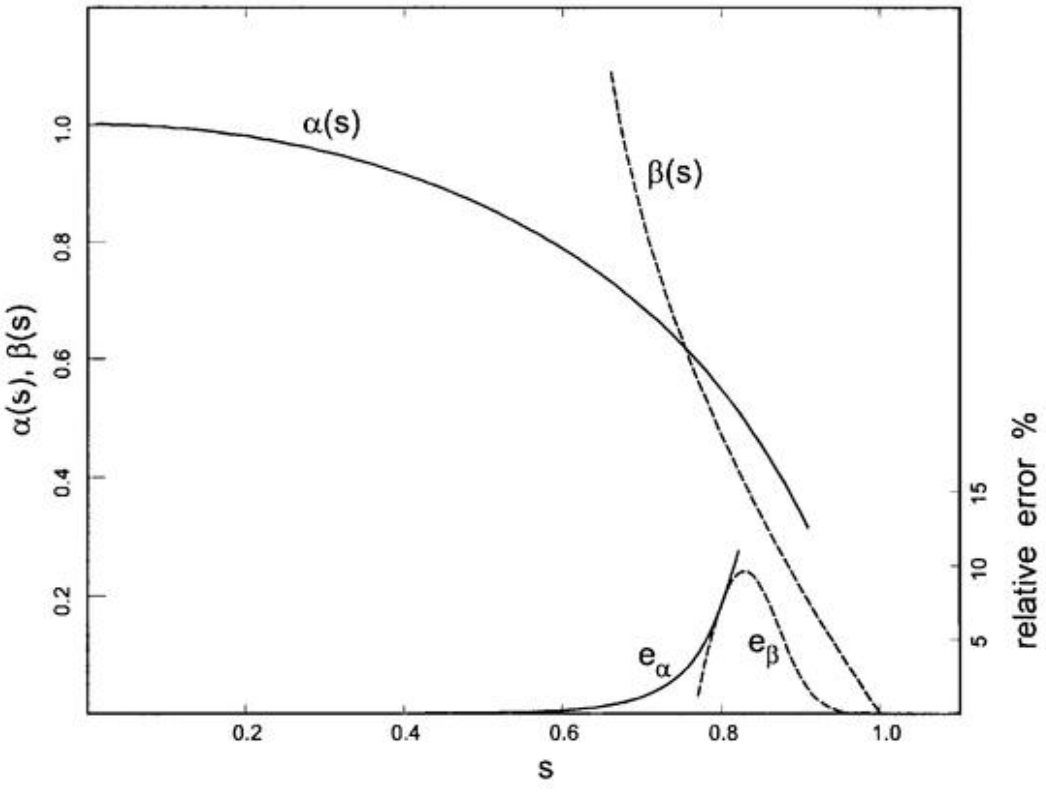

Fig. 3. Functions $\alpha(s)$ and $\beta(s)$ used for calculation of t. In the lower part of the plot the relative error curves are shown.

practice, the case when r is close to r_0 is more relevant, because of the larger magnitude of the perturbation and easier detection of its peak (as discussed in the next section).

Thus, the time t should be calculated from (1.32) or (1.35) depending on the value of the parameter s. In both cases the expression (1.30) is used, and therefore, one can easily invert the formula and calculate the diffusion D from the experimental values of t, r and r_0:

$$D = \frac{r^2 + r_0^2}{4t} \times \begin{cases} \alpha(s), & \text{for} \quad s < 0.8 \\ \beta(s), & \text{for} \quad s > 0.8 \end{cases} \tag{1.37}$$

In the beginning of this section, the pinch velocity V in the Eq. (1.18) has been neglected. Calculations show that the diffusion term is at least several times larger than the term with V (for a typical value of V of a few meters per second) in the initial phase of the evolution. More exactly, this is valid at any radius where parameter $s \geq 0.7$ and during the time until the maximum of $n(r, t)$ is achieved. These conditions are easily satisfied for the present task, when measuring the time of maximum at a radius r close to r_0.

1.5. Calculation of diffusion for non-zero deposition width.

The described above method allows to calculate the diffusion coefficient for the hypothetical situation when the initial perturbation is concentrated in one point of minor radius r_0. Although this case is practically unreal, the method can still be utilized for the case when the tracer deposition width Δr is not equal to zero.

It is seen from Fig. 2b that at some early time $t = \tau$ the decaying profile $n(r, \tau)$ has a bell-like shape, which is very appropriate for approximating of the tracer deposition profile. It means that the initial perturbation profile $n(r, 0)$ can be considered as one transient phase $n(r, \tau)$ of the found earlier solution of the diffusion task (See Eq. (1.24)). Clearly, all the following phases of such a profile will conform to the formula (1.24) with a shifted time axis. A certain profile $n(r, t_{exp})$ measured experimentally will be achieved earlier than the time t_{theor} calculated from (1.37) by the time shift τ:

$$t_{exp} = t_{theor} - \tau \tag{1.38}$$

Now it is necessary to express τ in terms of the given deposition width Δr, i.e. the characteristic width of the profile $n(r, \tau)$. For that, one should make the following transformations to the function $n(r, t)$ of Eq. (1.24), which can be written as:

$$n(r, \tau) = \frac{2 N_0 r_0^2}{\sigma} \exp\left(-\frac{r^2 + r_0^2}{\sigma} \right) I_0\left(\frac{2 r r_0}{\sigma} \right) \tag{1.39}$$

where $\sigma = 4\tau D$.

Approximation of the deposition profile with $n(r, \tau)$ is valid for small τ when the profile remains bell-shaped and compact in r (as the one in Fig. 2b at $t = 0.2$ ms). For small τ, one can use previous expansion (1.34) of $I_0(x)$ for $x >> 1$ and after simple transformations obtain

$$n(r,\tau) \sim \frac{1}{\sqrt{r}} \exp\left(-\frac{(r-r_0)^2}{\sigma}\right) \tag{1.40}$$

Here the square root dependence on r is much weaker than the exponent and can be neglected. The exponent in (1.40) has a typical Gaussian bell form with the center at r_0 and the half-width of $\sqrt{\sigma}$. Thus, the characteristic width of the profile $n(r, \tau)$ (with attenuation in e times) is

$$\Delta r = 4\sqrt{\tau D} \tag{1.41}$$

After substitution of this relation to (1.38) and using Eq. (1.37) for t_{theor} one can finally obtain

$$D = \frac{1}{4t}\left(\left(r^2 + r_0^2\right) \times \begin{bmatrix} \alpha(s), & \text{for } s < 0.8 \\ \beta(s), & \text{for } s > 0.8 \end{bmatrix} - \frac{\Delta r^2}{4}\right) \tag{1.42}$$

where t is the measured time moment of the maximal density at radius r;
r_0 and Δr are the center and the characteristic width of the initial perturbation;
$\alpha(s)$ and $\beta(s)$ are calculated from Eqs. (1.32) and (1.36), respectively.

When $\Delta r \to 0$, the formula (1.42) reduces to Eq. (1.37) and therefore it can be considered as an extension of Eq. (1.37) for the case of non-local tracer deposition.

It should be noted that for large values of Δr, expression (1.42) may become negative. This can be easily understood, because for a wide deposition profile (like the one in Fig. 2b at $t = 1.0$ ms) the density at a certain observation radius r may have already passed the maximum by the time τ (i. e. $\tau > t_{theor}$), as it is seen in Fig. 2a for $r = 12$ cm and $\tau = 1.0$ ms. This may happen for the observation points located close to the origin of perturbation r_0.

On the other hand, the curvature of the time dependence at the time of its maximum becomes larger when r is closer to r_0 (as it is seen from Fig. 2a). Obviously, for a larger curvature, the density peak can be detected more distinctly from the experimental signal containing noise. However, the nearest to r_0 location $r = r_{min}$ is limited by the above described situation with the non-zero deposition width Δr. The location $r = r_{min}$ can be calculated from Eq. (1.42) by setting the difference in the brackets equal to zero.

For smaller values of Δr, the observation point can be located closer to r_0 and the time of density peak can be measured more accurately resulting in a smaller error when calculating the diffusion. This clearly indicates the importance of the high localization of tracer deposition.

1.6. Summary

In this chapter we have discussed the necessity of the accurate measurement of the transport in plasma and reviewed several methods of the transport analysis. It was demonstrated that the methods studying the transient transport processes are more appropriate when the experimental information about all the plasma parameters is deficient for a complete transport model. The transport coefficients can be calculated more accurately when the perturbation being studied is rather localized and fast developing. As regards to the particle transport, it can be measured more correctly by analyzing the evolution of low-Z impurity ions artificially introduced into plasma, which are different species from the main plasma ions.

For the accurate diagnostics of the particle transport, the method of tracer-encapsulated pellet injection is very promising. By creating the highly localized impurity tracer source in the plasma core, the method allows measuring the particle transport both in parallel and in perpendicular to the magnetic field lines.

The procedure of analytical calculation of the diffusion coefficient from the experimentally observed density evolution was described, which is applicable for a point origin of the initial perturbation. The method was also extended for the case when the initial density perturbation has a small but finite width and can be approximated with a bell-shaped Gaussian curve. It was shown that with more compact distribution of the tracer deposition the diffusion can be calculated with smaller errors. This proves the idea that the deposition of the tracer particles in plasma should be very localized.

2. LITHIUM PELLET INJECTION

2.1. Introduction

It was shown in Chapter 1 that the particle transport in plasma can be analyzed by observing the motion of impurity ions introduced artificially into plasma, which are different species from the main plasma ions. This can be done by impurity pellet injection when the source profile of the impurity is created along the path of the pellet ablation. The radial distribution of the impurity ions and the pellet penetration into plasma are determined by the pellet ablation rate, which should be calculated from experimental data. The impurity transport study is also important for measuring the confinement of the impurity itself as the accumulation of impurity in plasma leads to a degradation of the plasma quality and results in a shorter energy confinement time.

It was also mentioned that the pellet should be made of a low Z material such as lithium in order to provide a fast and complete ionization of the injected impurity and achieve a very low rate of the atomic processes. This essentially simplifies the calculations since the source term in the particle balance equation can be neglected.

Lithium has another advantage due to its high chemical activity. Being coated on the plasma limiter or divertor it is capable of absorbing the other impurities (mainly, oxygen) from the plasma, thus reducing the impurity recycling and improving the plasma quality [24]. Experiments with lithium pellet injection with the purpose of coating on the plasma divertor have been extensively performed on TFTR [25] and have revealed a remarkable improvement of the plasma confinement.

In case of the helical magnetic configuration of Heliotron E the lithium pellet injection experiments pursued the following objectives:

1) Measure the response of the main plasma parameters during the injection and a possible change in global plasma confinement due to injection;
2) Analyze the behavior of lithium ions during the pellet ablation and in a longer time scale. Perform a numerical simulation of the experimentally measured lithium ion density evolution by means of impurity transport code.
3) Compare the ablation properties of Li pellet during EC H and NBI heated currentless plasma.
4) Study the plasma-wall interaction related to the lithium coating on the wall;

Before discussing the experimental setup and obtained results, let us describe the construction of the lithium pellet injector and the pellet loading routine.

2.2. Construction of the pellet injector

The schematic view of the lithium pellet injector is shown in Fig. 4. Prior the injection a set of 30 pellets is loaded into the disk *1* of the magazine *2*. This procedure of loading and details of the construction of the magazine will be discussed below. After the pulse of the propellant gas from the shooting valve *3* with duration of 2-4 ms and pressure of 30-50 atm, a pellet *4* located on the shooting axis is accelerated and goes through the removable barrel *5*, manual valve *6*, and the main barrel *7*. The inner diameters of the removable barrel and the main barrel are 1.0 mm. The length of the acceleration path of the pellet is 1.2 m. Then the pellet crosses the beam of He-Ne laser *8* expanded by the beam expander *9*. The light from the beam expander goes to the light detector *10* that has two input slits at 5.5 mm distance and this allows a rough

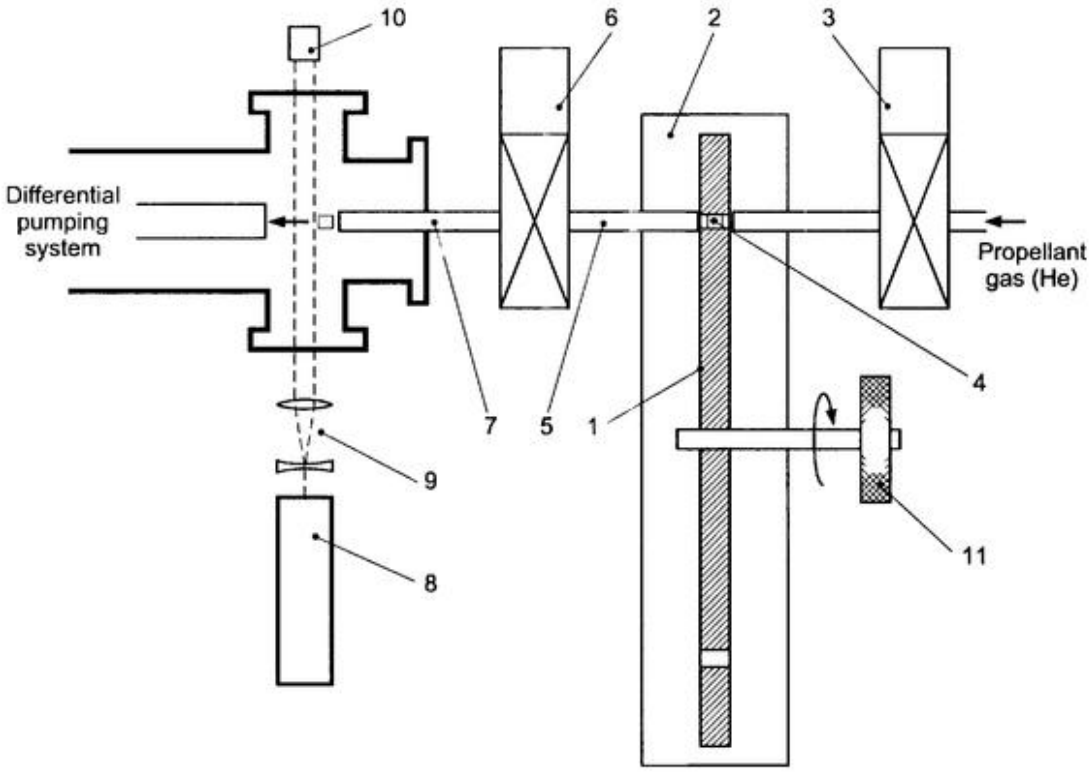

Fig. 4. Schematic view of the lithium pellet injector.

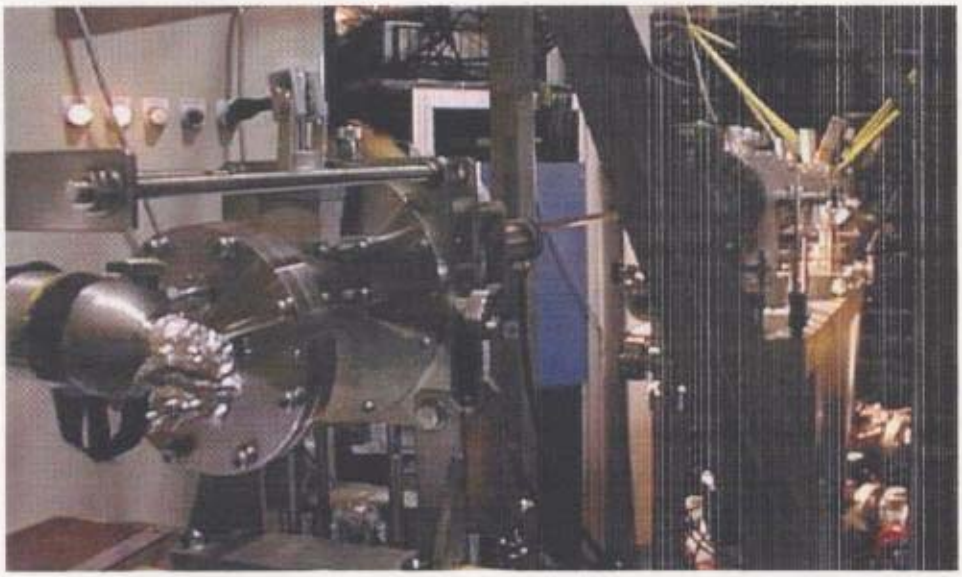

Fig. 5. Photo of lithium pellet injector with differential pumping system.

estimation of the pellet velocity. The accurate measurements were made by the time difference of the light detector signal and the plasma density increase due to the injected pellet. After each shot the disk in the magazine is manually rotated by the handle *11* so as to position the next pellet.

A photo of the pellet injector with differential pumping system is shown in Fig. 5. The differential pumping system consists of four vacuum chambers isolated by gate-valves. Three of them are pneumatic type gate-valves with closing time of 0.5–1 s and the nearest to the injector is electromagnetic gate-valve with closing time of about 0.05 s for a faster cut-off of the propellant gas wave following the pellet. The four guide tubes are 0.14 m, 1.5 m, 0.4 m, and 2.7 m long, respectively. The inner diameters of these guide tubes are 2.27 mm, 4 mm, 7.53 mm, and 10.7 mm, respectively. The gap distances between the guide tubes were calculated so as to allow a pellet to pass the gaps safely for the typical scattering of the pellet trajectory of within 1° in full angle.

To load the pellets into the magazine the latter is dismounted from the injector (See Fig. 6). For that, the valve *1* is closed and the accelerating valve *2* is removed. Then the nut *3* is removed and the magazine *4* with the removable barrel *5* is shifted from the "main position" to the "dismount position". A pair of O-rings *6* maintains the vacuum isolation. Then the manual gate valve *7* is closed and prevents air from coming into the differential pumping system. Finally, the magazine *4* is separated at points *8* and now it can be used to load the pellets.

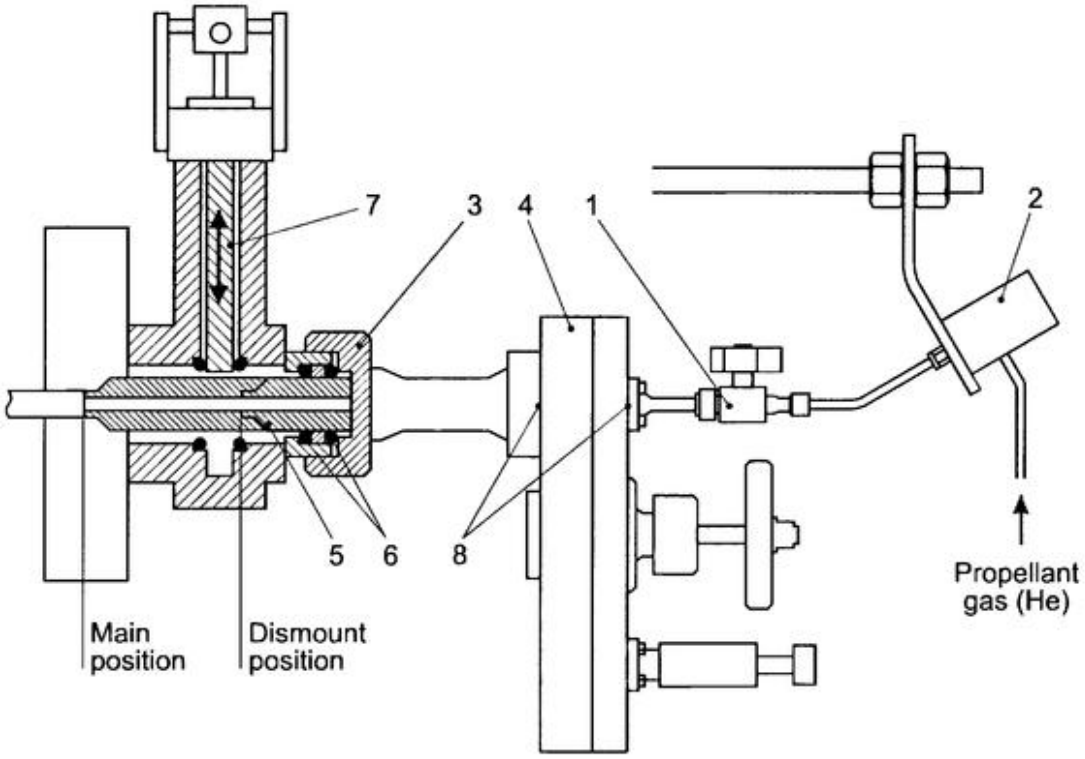

Fig. 6. Principle of dismounting of the pellet magazine.

2.3. Preparation and loading of the lithium pellets

The pellet production routine described below is similar to that used on TFTR where rather large (∅2×2 mm size) cylindrical lithium pellets were produced for the injection [26]. For the Heliotron E plasma, the Li pellet size should be much smaller implying a higher accuracy requirement during the pellet production and handling. The process was also improved with respect to maintaining Li pellet purity.

2.3.1. Physical and chemical properties of lithiu

Because of its high chemical activity, lithium reacts quickly with oxygen and water from the air and slower with nitrogen. This makes impossible any operation with lithium on the open air. In the nitrogen atmosphere due to the interaction with N_2 lithium slowly turns into lithium nitride Li_3N, warms up and reacts quicker. This does

not allow to use nitrogen gas for preserving lithium purity. It seems that only the noble gas atmosphere can resolve this problem. The other way to conserve lithium may be in keeping it in a non-active liquid. Besides water lithium reacts with many organic substances except for hydrocarbons and some others. Therefore it is possible to use light liquid hydrocarbons such as hexane to avoid the contact of lithium with the outer atmosphere. At the same time these liquids are very volatile and quickly disappear during the vacuum pumping thus satisfying to the high vacuum conditions.

The physical properties of lithium also make operation with it very difficult. Lithium is a soft but very sticky metal. Being pressed on a steel plate lithium fills in the harshness of the metal surface and easily sticks to it. After that the complete cleaning of the polluted surface is possible only by washing in a water. Among the most inert to the lithium stickiness materials are nickel and nickel oxide (NiO).

2.3.2. Operation in the glove-box.

According to the above remarks all the work with lithium is performed in the hermetic glove-box filled with helium gas (See Fig. 7). It has a 15 cm size cubic sluice *1* from organic glass with two doors *8* that can be hermetically closed. The sluice can be pumped out to low vacuum through valve *3* and filled with helium. The vacuum level in the sluice is monitored by the vacuum gauge *4*. By means of such a

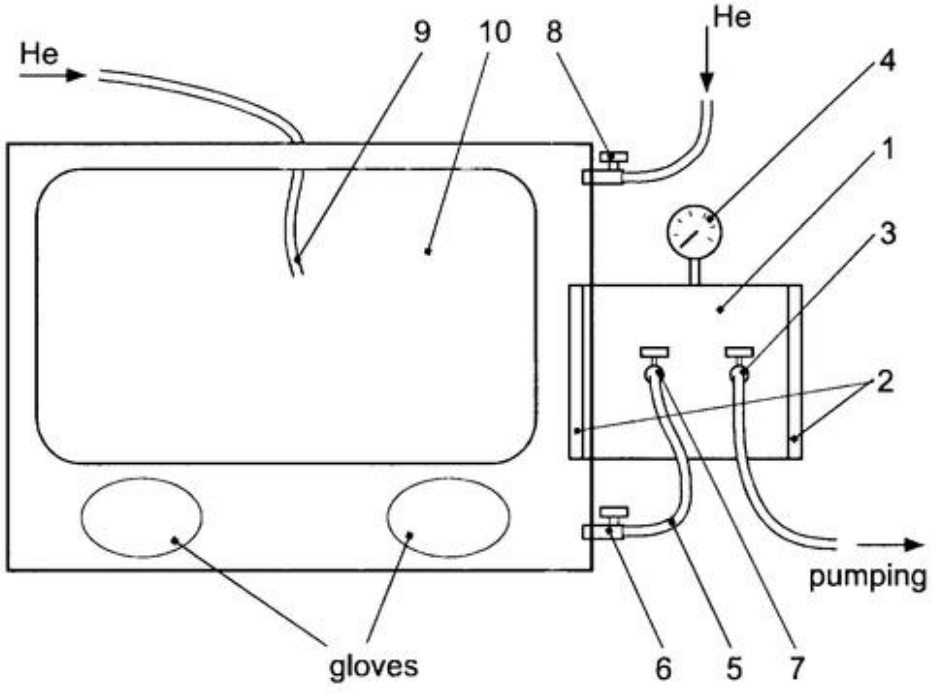

Fig. 7. Schematic view of the glove-box.

sluice it is possible to insert and remove necessary utensils and the magazine itself without direct contact of the inside atmosphere of the glove-box with the outside air.

To simplify the connection of the pipes the pumping of the glove-box and filling of the sluice are performed through the pipe *5*. The valve *6* is always open and the valve *7* is open only for equalizing the pressure in the sluice and the glove-box. The helium supply to the glove-box is performed mainly through the valve *8*.

The construction of the glove-box does not allow a complete evacuating of its atmosphere and subsequent filling with helium gas. To solve this problem a polyethylene balloon of a size bigger than the glove-box is put into the glove-box in the compressed state. Then a pipe *9* that goes inside and supplies helium is inserted into the balloon and fills it with helium. Thus the balloon occupies almost the whole space of the glove-box while the old atmosphere is pumped out through the pipe *5*. Then the filling is stopped and the remaining free space is ventilated with helium through the valve *8* for a few minutes. After that the balloon is blown out and removed from the glove-box through the sluice. After such a process the purity of helium atmosphere keeps the surface of a cleaned lithium piece gleaming for about 15 minutes.

2.3.3. Loading of the Li pellets.

Because of the lithium softness it is very easy to produce a thin (~1 mm) lithium layer by pressing a piece of lithium between two thick metal plates, which are covered by nickel or nickel oxide to reduce adhesion to lithium. It is also good to moisten the surfaces of the plates with liquid hexane before pressing. After that the prepared lithium layer is used for punching out the pellets by means of a special pipe with inner diameter 1 mm, outer diameter 3 mm, and length about 120 mm. The working edge of the pipe is sharpened at 45°.

To prolong the life time of the lithium purity, the lithium layer is placed in a shallow hexane bath when punching out the pellets. Finally, the pellets are loaded into the disk as shown in Fig. 8. The pellet *1* is pushed out of the pipe by means of the ∅1 mm wire when the pipe is set upon the next hole in the disk *4*. The exact positioning of the disk with pellets is provided by a special stopper *3* with spring. The disk *4* has a radial set of corresponding hollows *5*. The O-rings *4* are designed to prevent the propellant gas from getting into the magazine during the injection. Another function of these O-rings is to isolate the inner space *7* with pellets from the outer atmosphere. In fact, only 29 pellets are loaded, and the hole at the shooting axis is left empty. After the magazine is removed from the glove-box, the inner space of the disk with pellets is pumped out through the hole *6*. Thus, 29 pellets are isolated from the air and the magazine can be mounted back on the pellet injector. In this state the loaded pellets may remain during 20–30 hours before the injection. After that the injection may

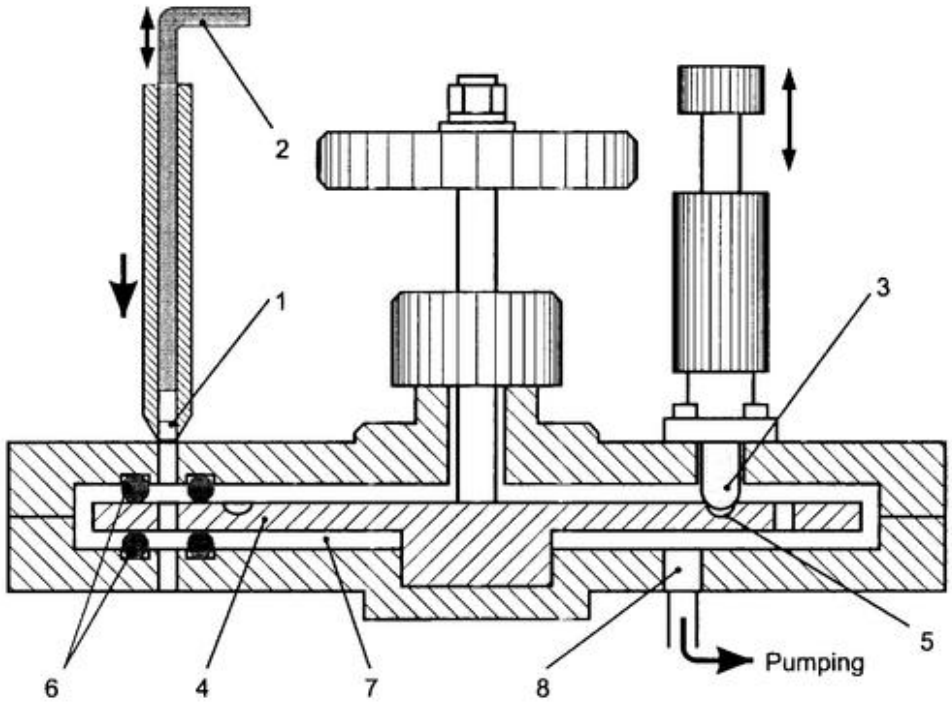

Fig. 8. Method of loading Li pellet into the disk of the magazine.

become difficult as lithium slowly absorbs impurities from the stainless steel of the disk and adheres to it.

2.4. Testing of lithium pellet injector

The main purpose of the laboratory tests of the lithium pellet injector was to achieve a high reliability of the injection and to define the main reasons that made the injection unstable. Among these reasons it is necessary to mention (in the order of decreasing of their probability):

1) Pellet may fall out from the disk during the mounting of the magazine.
2) Pellet may remain in the disk after the shot of the propellant gas.
3) Pellet may stop at the joint of the removable barrel and the main barrel (see "main position" in Fig. 6).
4) Pellet may stop in the main barrel.

Let us discuss the above problems and their solutions. The first tests were made with the disk having ∅1.1 mm holes. In average 20% of pellets fell out from the disk before the injection due to accidental shakes of the magazine. In the new construction

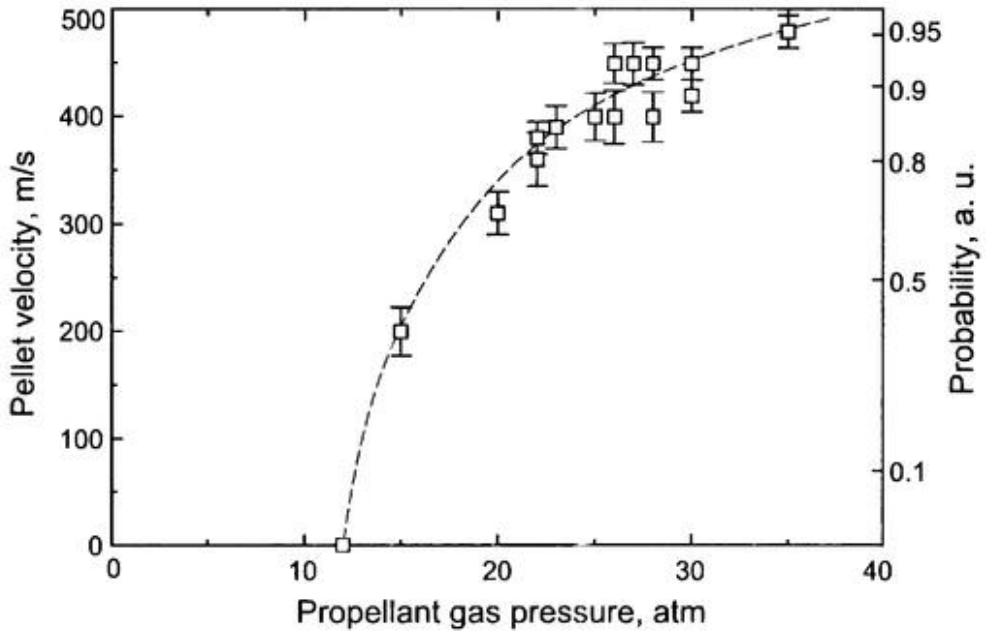

Fig. 9. Achieved velocities of the lithium pellets vs. propellant gas pressure. The right axis shows approximate statistics of the injection reliability.

of the disk the diameter of the holes is 1.0 mm. This allows to reduce the percentage of the losses to 3–5%.

On the other hand, with reduced diameter of the holes, the effect of adhesion of lithium pellets to the disk has increased with simultaneous reduction of the accelerating force. Fig. 9 presents a dependence of the pellet velocity on the propellant gas pressure for the disk with 1.1 mm holes. The error bars represent average errors of measuring the pellet velocity. The right axis of the plot shows the approximate probability of the successful acceleration. A fairly stable injection can be performed if the propellant gas pressure is not less than 25 atm. For the new construction of the disk a pressure of 40 atm is required. It is seen from Fig. 9 that the range of pellet velocities is rather narrow. With higher propellant gas pressure the velocity dependence becomes slower and achieving the velocities higher than 500 m/s is problematic. On the other hand, decreasing of the pressure leads to unstable injection and at the pressure less than 15 atm no pellet can be shot from the disk. Also, as it was mentioned earlier, the stability of injection can be increased by reducing the "waiting" time between the loading of pellets and the injection.

The problems with stopping of the pellets on the acceleration path can be also solved by increasing the propellant gas pressure. Duration of the propellant gas pulse has a weak effect on the dependencies in Fig. 9, since the very first moment of 1–2 ms

is important for the acceleration. Increasing the pulse duration leads to a higher undesirable pressure jump in the differential pumping system.

Summarizing what was said about the Li pellet production and acceleration, the following points should be underlined:

1) Because of its chemical activity lithium should be handled in a glove-box with the noble gas atmosphere (He, Ar, etc.).
2) A special procedure of replacing the glove-box atmosphere allows to achieve high purity of the noble gas.
3) When making the pellets it is better to keep the clean lithium in the liquid hexane so as to maintain its purity.
4) The propellant gas pressure for Li pellets should be not less than 25 atm. For this reason, it is difficult to obtain pellet velocities of less than 400 m/s.

The lithium pellet injector has been installed on Heliotron E and has demonstrated the reliable operation. No increment of light emission of such impurities as nitrogen or oxygen has been observed during the injection, which proves the high purity of the lithium pellets.

2.5. Experimental set-up of lithium pellet injector and observing diagnostics.

Heliotron E is a heliotron/torsatron device with multipolarity l of 2 and toroidal period number m of 19. The major radius is 2.2 m and the poloidal cross-section of the outermost flux surface is elliptical with half axes of 0.16 and 0.25 m. The magnetic field strength is 1.9 T. The wall of the vacuum chamber is exposed to boronization, which is performed by ECH discharge with $B_{10}H_{14}$ and helium [27]. The plasma is initiated by a 106GHz gyrotron with 300 kW power. The frequency corresponds to the second harmonic heating at B = 1.9 T. The plasma is further heated by NBI with acceleration voltage of 23 kV and the power up to 3.5 MW. At the typical plasma condition during the NBI heating the central electron temperature and density are 0.7 keV and 5×10^{19} m^{-3}, respectively.

A schematic view of the experimental layout of the lithium pellet injection on Heliotron E is shown in Fig. 10. A lithium pellet is injected in the equatorial plane and crosses the plasma column at 8° angle to the longer minor radius. Above the injection line an observation port is located for collecting the light from the cloud of the

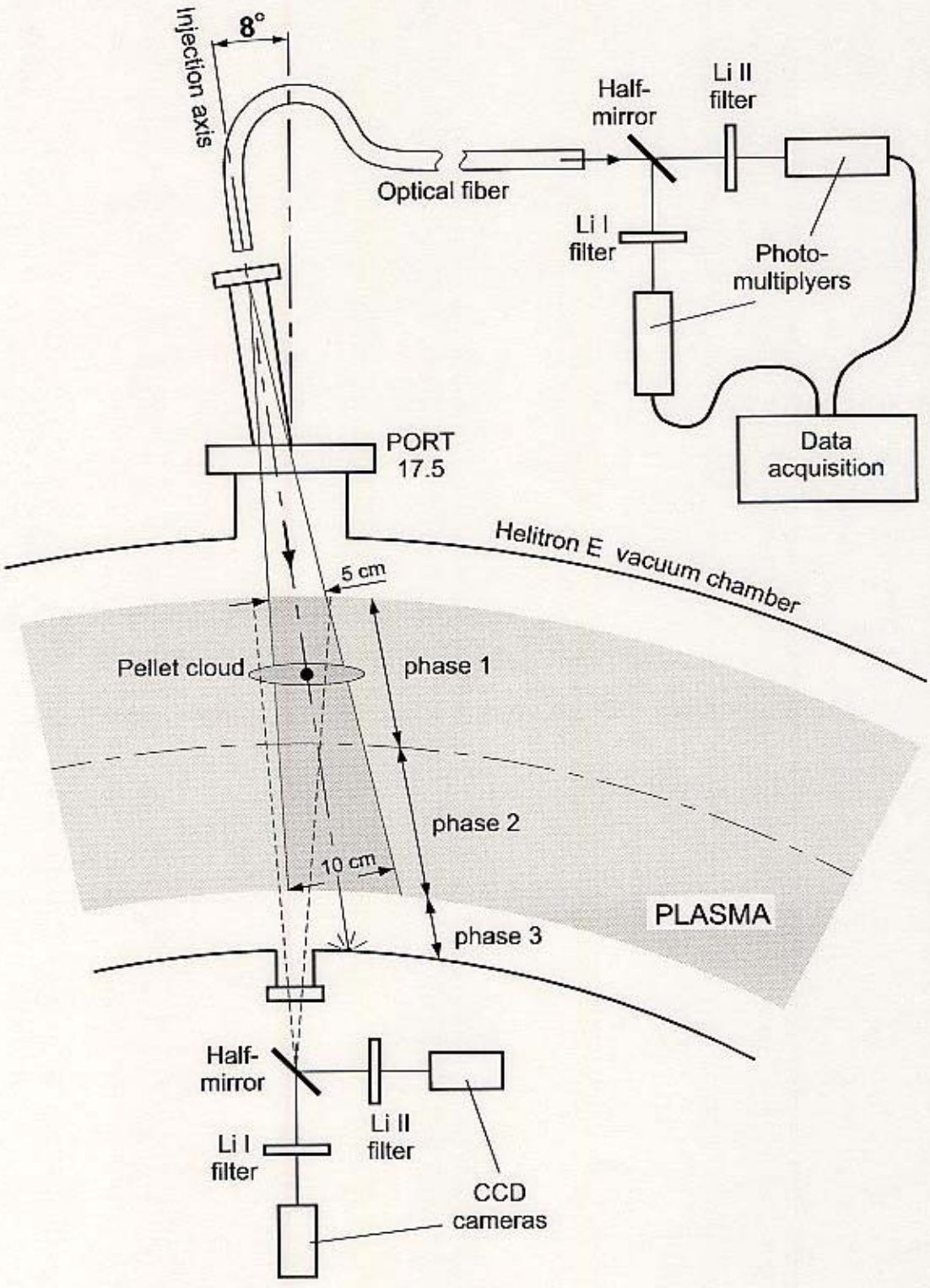

Fig. 10. General layout of the lithium pellet injection experiments on HeliotronE.

ablating pellet. The visible area for this observation point is indicated as a dark gray colored sector in the Figure. It is seen that maximal observed dimension of the pellet cloud ranges from 5 cm at the beginning to 10 cm in the end. The light is transferred by optical fiber to the optical system having a half-mirror and two light filters for Li I and Li II lines (wavelengths $\lambda_1 = 670.6$ nm and $\lambda_2 = 548.5$ nm, respectively). The filtered light is registered by two photo-multipliers and their signals are recorded by the data acquisition system having 12-bit ADC with 0.2 μs time resolution. This allows measuring the lithium cloud luminosity in the two different spectral regions simultaneously in the same location.

At the opposite port a similar optical system is installed including a half-mirror, Li I and Li II filters, and two CCD cameras which record the image (640×240 pixel) of the pellet cloud emission. Because of the long exposure time (~15 ms) the obtained images represent the light integrated during the full time of the pellet ablation. A fast film camera with maximal time resolution of 40 μs has also been used for this purpose. However, the light intensity from the pellet cloud was apparently insufficient for such a short exposure and the obtained images could not be analyzed.

The long time scale diffusion of the lithium ions was measured by observing the Li III emission of Li^{2+} ions originated from the charge exchange recombination of Li^{3+} ions [28]. The transition from ^2G to ^2F (449.9 nm) was measured by a 1.26 m visible spectrometer with a 2-dimensional detector and time resolution of 20ms. The sight-lines of 40 optical fibers crossed the plasma from 1.98 m to 2.42 m on the major radius with spatial resolution of 13 mm. This allowed to obtain the data of the Li ions profile evolution which were used for the impurity transport simulation (See Section 2.7.2). The prominent line (13.5 nm) was registered by a multi-channel vacuum ultraviolet (VUV) spectrometer with 10 ms time resolution.

2.6. Experimental results and discussion

2.6.1. Plasma response to lithium pellet injection

The injection was performed in three types of discharges: NBI heated plasma, ECH heated plasma and NBI+ECH simultaneously heated plasma. Time evolution of the main plasma parameters in a typical discharge with NBI heating is shown in Fig. 11. It includes a signal from the FIR interferometer of a line integral of the

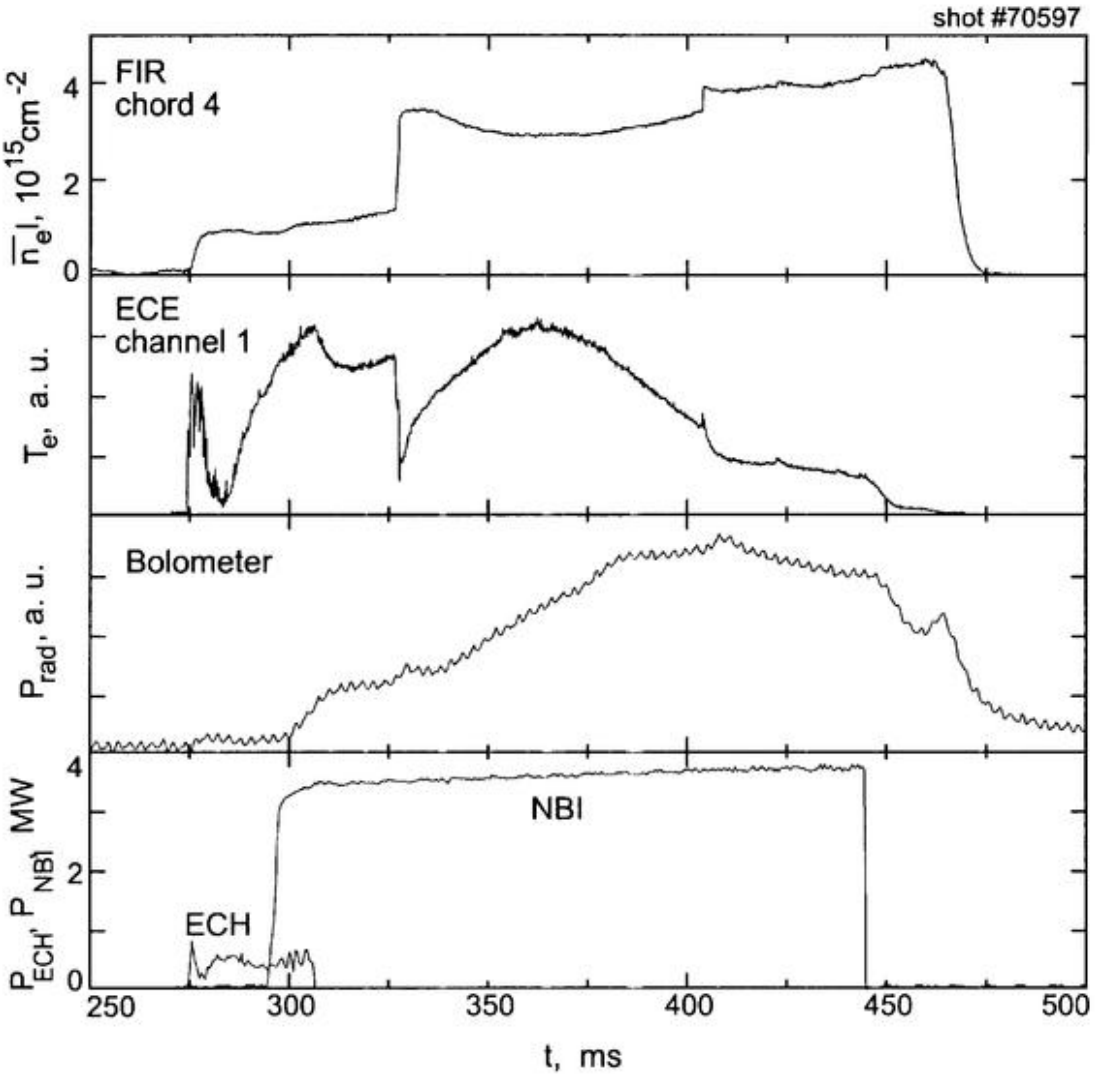

Fig. 11. Temporal dependencies of (a) FIR signal of line density at $r = 2$ cm, (b) ECE second-harmonic signal of electron temperature at $r/a = 0.46$, (c) signal of wide view bolometer, (d) input power of ECH and NBI heating. The Li pellet was injected at $t = 328$ ms.

electron density along the central chord in the poloidal cross section; an ECE signal of the electron temperature; a wide view bolometer signal and the input power of ECH and NBI heating. Estimates show that at the Heliotron E plasma conditions a Li pellet of ∅1×1 mm size (total number of atoms in the pellet is 3.6×10^{19}) deposits in the ECH heated plasma only about 30% of its mass and about 60% in the case of the NB plasma. The latter corresponds to an addition to the average electron density of about 4×10^{13} cm^{-3} and the central density reaches 1.5×10^{14} cm^{-3}. At that moment the ECE signal from the plasma center can be damped because of the cut-off region that appears when the density exceeds 10^{14} cm^{-3}. For this reason Fig. 11 presents a non-central ECE channel (r/a = 0.46).

The changes of electron temperature, density and pressure profiles due to the Li injection in the NBI plasma are shown in Fig. 12. This plot includes the data of several discharges and represents the general response of the temperature and density under similar plasma conditions. The profiles were measured just before the injection and 3–5 ms after. It is clearly seen that the electron pressure $p = nT_e$ increases after injection by about two times. The analogous comparison in the case of ECH discharges (the central electron temperature changes from 1.5 keV to 0.5 keV and the density from 3×10^{13} cm^{-3} to 9×10^{13} cm^{-3}) shows that the plasma response is almost adiabatic, with a conservation of electron pressure.

The increase of electron pressure after injection into NBI-heated plasma may have the following explanation. In the NBI plasma the ion temperature is usually in the range of 700–1200 eV, while the electron temperature especially after injection is 300–500 eV. The estimations show that in the electron heat balance equation the term of the heat exchange with ions is 5–10 times more than the heat diffusion term. At the same time for the case of ECH discharges these terms are comparable. This is due mainly to the relation between electron and ion temperatures and also to the higher

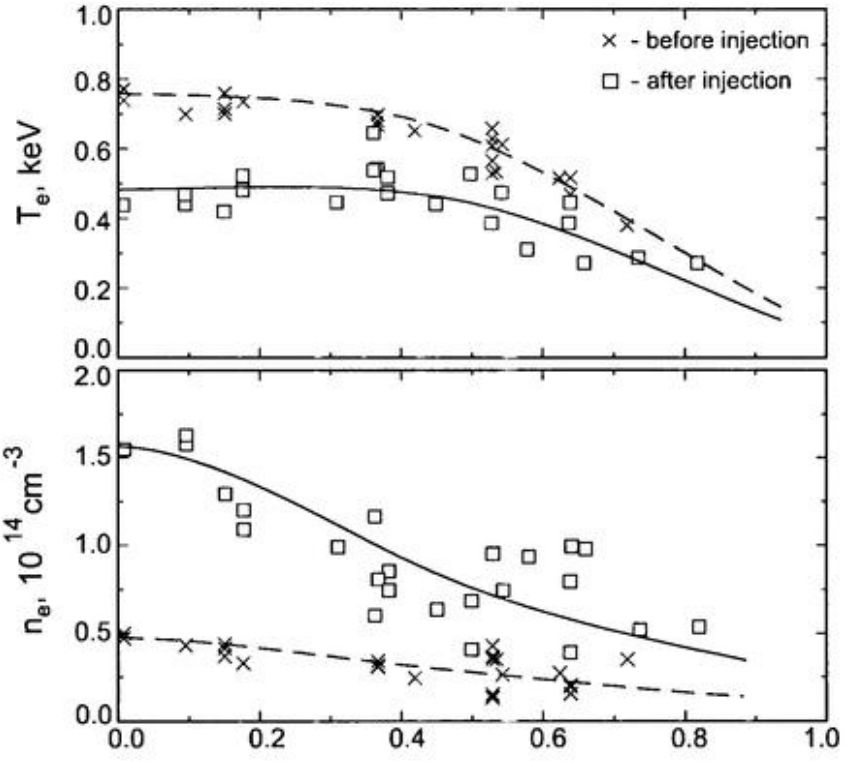

Fig. 12. Profiles of electron temperature and density before (crosses) and after (squares) the Li pellet injection into NBI-heated plasma. Dashed and solid curves show spline approximations of the data before and after injection, respectively.

electron density after injection into NBI plasmas. Therefore we may assume that after injection the electron energy component is fed by the high temperature ions. Another source of such a heating of electrons after injection may come from the fast ions of the neutral beam. First of all, the absolute power deposition of NBI is increased owing to the increase in both density and effective charge Z. Secondly, the critical beam energy of the fast ions is lowered by a factor of 0.57 (for $Z=3$ and $A=7$) which results in a more favorable heating of the electrons.

2.6.2. Emission from the lithium pellet cloud.

The typical time evolution of the lithium cloud emission on Li I and Li II lines during injection into ECH and NBI heated plasma is shown in Fig. 13 with corresponding time dependencies of the interferometer signal for density and ECE signals for the electron temperature. The Li I and Li II signals can be divided in four characteristic phases shown with vertical dashed lines in the Figure. For the known pellet velocity, the duration of the phase 1 corresponds to the pellet flight length of 22 - 28 cm when the pellet moves from the outer plasma edge to the plasma axis. During the phase 2 the pellet goes further to the inner plasma edge. Then, the pellet leaves the plasma and reaches the vacuum vessel wall at the end of phase3. The emission during the phase4 corresponds to the evaporation of the Li particles from the residual pellet.

We should note, that the observed delay Δt of about 200μs between the start of the phase 1 and the response of the interferometer signal can be explained by the difference of 180° in toroidal location of the pellet injector and FIR interferometer. Since the propagation speed of the density perturbation is determined by the thermal energy of ions, one can estimate the temperature of the ions surrounding the ablating pellet:

$$\frac{m_i v^2}{2} = \frac{3}{2} T_i \quad \Rightarrow \quad T_i = \frac{m_i}{3}\left(\frac{\pi R}{\Delta t}\right)^2 \tag{4.1}$$

For a case of deuterium ions, this gives $T_i \approx 8$ eV, which is a typical value for the plasma of the pellet cloud.

Time-integrated images of the lithium pellet cloud recorded by CCD cameras are shown in Fig. 14. Images of Li I and Li II emission are overlapped according to the geometrical configuration. The contour lines indicate the pellet position along the minor radius r and the vertical scale of 1 cm. Due to the oblique observation angle related to the pellet path (See Fig. 10), the scales of horizontal and vertical directions are different. The deviation of the pellet path from the designated direction is within

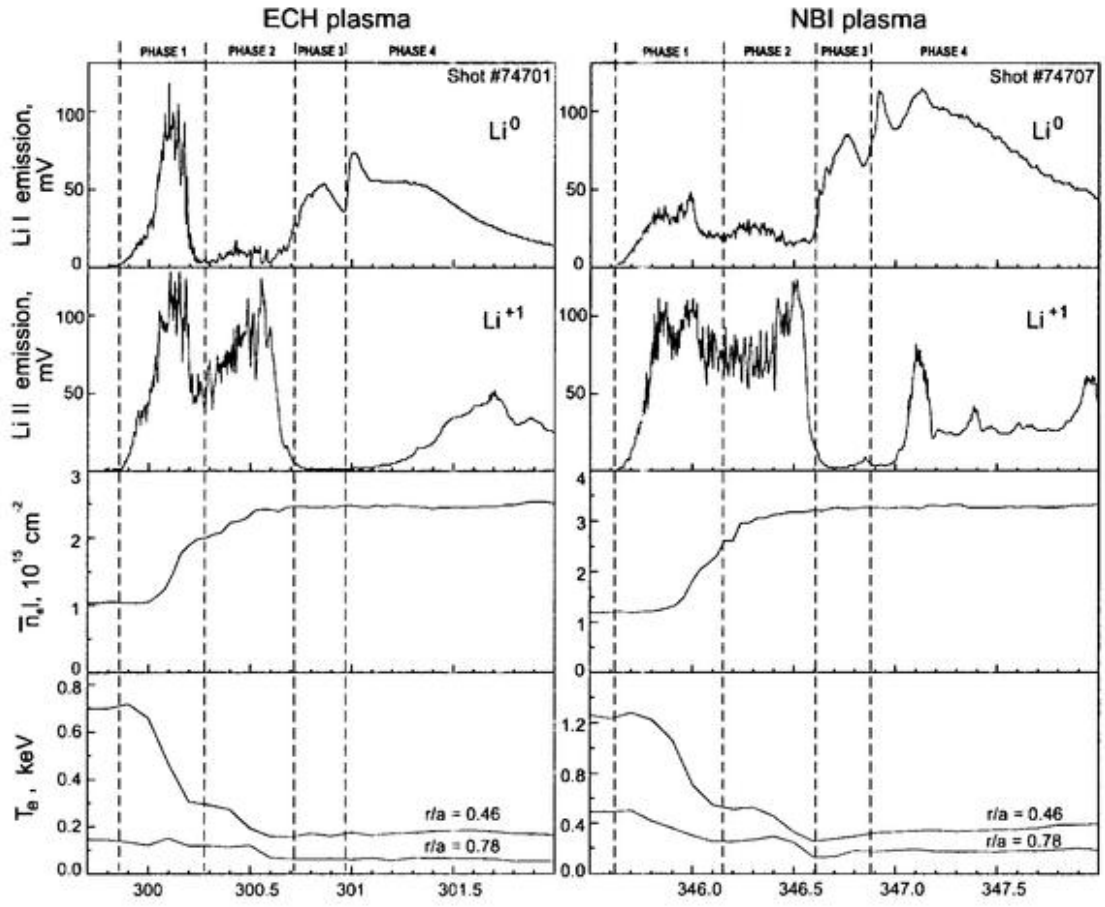

Fig. 13. Temporal dependencies of Li I and Li II emission during the injection into ECH (on the left) and NBI (on the right) heated plasma. Interferometer signal of the line density along the central chord and two ECE signals (at $r/a = 0.46$ and $r/a = 0.78$) of the electron temperature are also shown.

1 cm. The observable area covers the pellet path from the start to $r = -4$ cm (beyond the plasma axis).

It is seen, that Li II trace is much wider than that of Li I, since the Li^+ ions producing the Li II light can move further from the pellet path than the Li neutrals emitting in Li I. The ionization rate coefficient S_0 of Li^0 is about 10^{-7} cm^3/s over the wide range of electron temperatures (See Fig. 15), and $1–4\times10^{-8}$ cm^3/s for Li^+ for the range of $T_e = 50–10^3$ eV. Thus, the ionization time of Li^0, i.e. the life time of Li neutrals $\tau = 1/S_0 n_e$ is 0.5 μs in case of $n_e = 2\times10^{13}$ cm^{-3}, and the length of free expansion of the neutral gas cloud having the temperature of 5 eV is about 5 mm. This corresponds well to the observed width of the Li I trace in Fig. 14 b). The similar estimation for the Li^+ ions gives $\tau \approx 12–50$ μs and the length of 12–48 cm that also

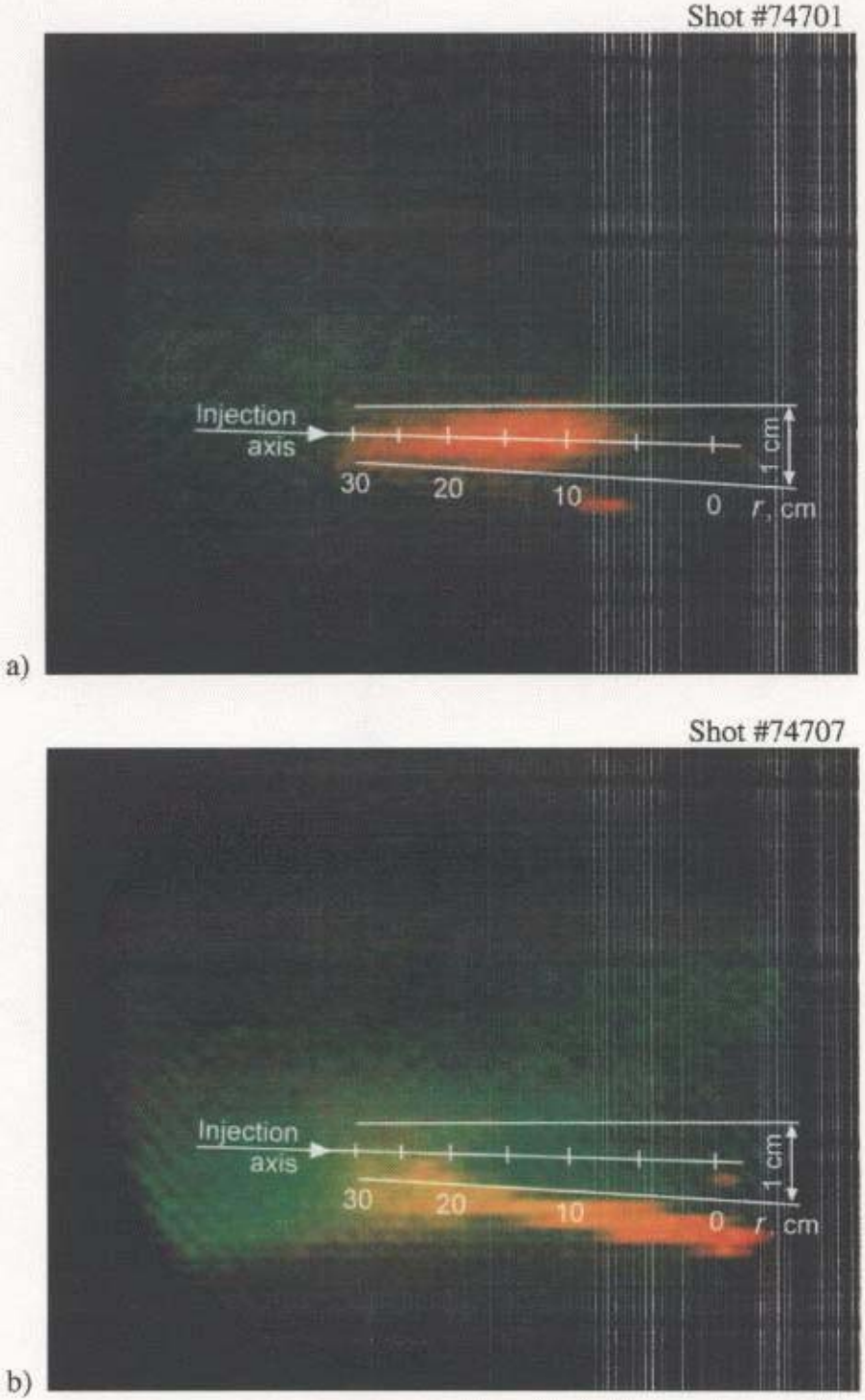

Fig. 14. Time-integrated overlapped images of Li I (red color) and Li II (green color) emission during the pellet injection into ECH (a) and NBI (b) heated plasma. Contour lines indicate the pellet position along the minor radius r and the vertical scale of 1 cm.

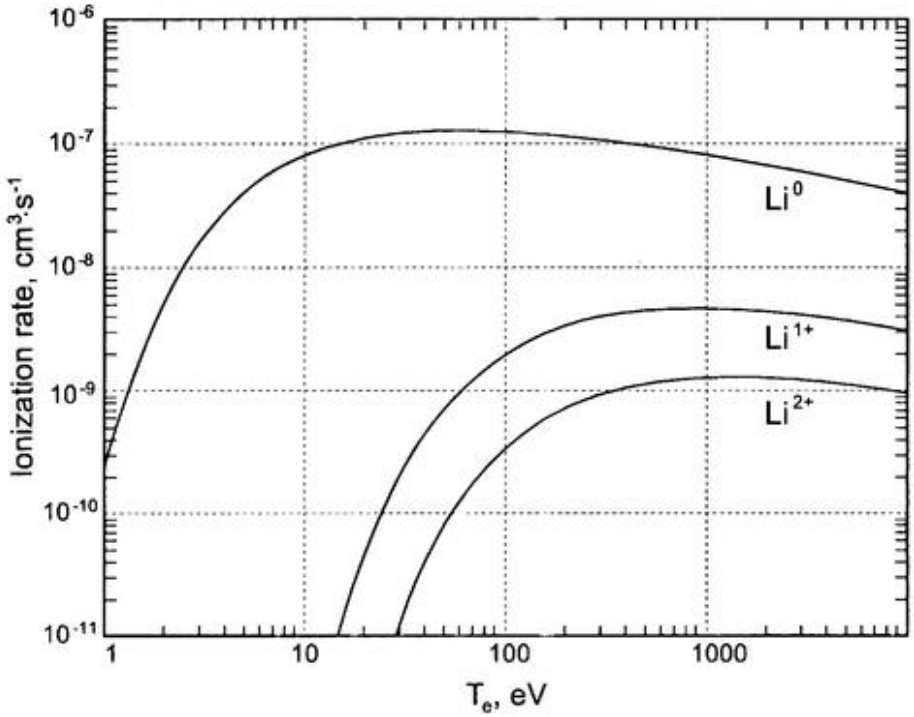

Fig. 15. Ionization rate coefficient for various Li ions versus electron temperature of the background plasma [29].

agrees to the images in Fig. 14. The observed Li I trace is wider for the case of injection into ECH heated plasma, which can be explained by the lower plasma density during the injection and hence longer life time τ of Li^0. On the other hand, the space integrated Li I emission (measured by the photo-multiplier) is also much stronger during the phase 1 for the ECH case than that for NBI. This is seen from Fig. 13 by weighing the Li I intensity during the phase 1 against the one during the phase 4. This is attributed to the intense ablation by the fast (supra-thermal) electrons produced by the ECH [30]. They are soon damped due to the density increase which causes rapid decrease of both the electron temperature and the fast electron population.

The behavior of the time dependencies of Li I and Li II emission shown in Fig. 13 becomes clearer if one analyzes the balance equations for Li^0 and Li^+ similar to (1.1). Because of the space integrated observation, the term with particle flux can be omitted:

$$\frac{\partial n_0}{\partial t} = \dot{N} - S_0 n_0 n_e \tag{4.2}$$

$$\frac{\partial n_1}{\partial t} = S_0 n_0 n_e - S_1 n_1 n_e \tag{4.3}$$

where n_0 and n_1 stand for the amount of Li^0 and Li^+ particles, respectively, in the observable area; n_e is the plasma density; $\dot{N}$ is the pellet ablation rate; S_0 and S_1 are the ionization rates of Li^0 and Li^+. The terms with recombination are neglected in Eqs. (4.2) and (4.3) because of the very low rate of this process comparing to the ionization rate for the wide range of the plasma temperatures. So, the time required for the recombination is much larger than the time necessary for Li ions to diffuse along the magnetic field lines out of the visible area.

After the time $\tau \approx 1/S_0 n_e$ from the start of ablation, the appearance of the new Li^0 particles is compensated by the ionization, hence the ablation rate $\dot{N}$ in Eq. (4.2) is almost completely balanced by the term with ionization:

$$\dot{N} \cong S_0 n_0 n_e \tag{4.4}$$

On the other hand, the Li I intensity $I_{Li\,I}$, i.e. the production rate of Li I photons $\frac{dP_{Li\,I}}{dt}$, is proportional to the excitation rate of the Li^0:

$$I_{Li\,I} = \frac{dP_{Li\,I}}{dt} \sim S_{exc} n_0 n_e \tag{4.5}$$

And using Eq. (4.4) one can write:

$$\dot{N} \sim \frac{dP_{Li\,I}}{dt} \frac{S_0}{S_{exc}} \tag{4.6}$$

Thus, the ablation rate is directly proportional to the measured intensity of the Li I emission, because the ratio of the ionization and excitation rates is approximately the same for the wide temperature range. Similarly, it can be shown that the ablation rate is also proportional to the Li II intensity but with lower accuracy. In section 2.7.1 we shall describe the procedure of deriving the ablation rate from the experimentally observed Li I intensity.

In the end of phase 1 in Fig. 13 the intensity of both Li I and Li II decreases apparently because of the drop in the electron temperature caused by the large amount of particle deposition. (As it was said earlier, this effect is more distinct for the case of ECH plasma.) For such a change of the electron temperature, the ionization rate of Li^+ becomes lower while that for Li^0 almost does not change (See Fig. 15) resulting in a positive balance of Eq. (4.3). The ablation rate is, typically, proportional to 3/2 power of the electron temperature [31] and therefore the balance of Eq. (4.2) becomes negative. This can explain the fact that Li II emission is not suppressed as much as that of Li I and continues with lower intensity. The gradual increase of the Li II intensity during the phase 2 is attributed to the further decrease of the electron temperature. This can also be explained by enlargement of the area of Li^+ cloud visible by the observation system as it is seen fromFig. 10. In the end of phase 2, when the pellet comes to the plasma edge with rather low electron temperature, the Li II emission decreases significantly with simultaneous growth of Li I. This is caused

by the balance shift of Eq. (4.2) to the dominance of ablation rate over the ionization of Li^0, as the latter decreases exponentially with temperature. Moreover, the L^0 life time becomes longer also because of the lower density of peripheral plasma. For these reasons, the Li I intensity is much larger than the Li II during the phase 3. Finally, the strong emission of Li I during the phase 4 is attributed to the pellet-wall impact and evaporation from the residual Li pellet with exponential decay. The Li II emission also appears gradually as a result of ionization of the Li atoms at the plasma edge.

2.6.3. Ablation rate studies and lithium coating on the wall

It may be worth to mention the other results obtained during Li pellet injection.

The pellet ablation rate derived from the time evolution of LiI and Li II intensities was compared to various pellet ablation models [33]. The observed discrepancy between the experimental and modeled ablation rates can arise from the anomalous ablation stimulated by the fast ions during injection into NBI plasma and fast electrons during ECH.

The experiments with Li injection were also made in order to study the plasma–wall interaction related to the lithium coating on the wall. Some improvement of the wall conditioning was expected, as lithium easily absorbs impurities such as oxygen. To check the possible improvement of the plasma purity, Oxygen V line was observed [28]. The lithium coating was confirmed by cumulative increase of Li I emission at the plasma boundary after several successive discharges with Li injection. However, the Oxygen V intensity revealed no noticeable reduction in the relative impurity level normalized by the electron density.

2.6.4. Summary

An injected lithium pellet is not completely evaporated in plasma and deposits about 30% of its mass in the ECH plasma and about 60% during injection into NB heated plasma. The electron pressure is doubled after the injection into NBI plasma and unchanged in case of the ECH. Emission of the pellet cloud was measured simultaneously in Li I and Li II lines with high time resolution. The time integrated images of the pellet cloud in Li I and Li II lines were recorded by CCD cameras and allowed to estimate the typical free path lengths of the Li^0 and Li^+. The time evolution of the Li I and Li II intensities was demonstrated to be in a good agreement with the balance of the pellet ablation rate and ionization rates of Li^0 and Li^+. The wall conditioning by a consecutive lithium pellet injection has revealed no substantial reduction of the impurity contents in the plasma.

2.7. Simulation of impurity transport

2.7.1. Ablation rate normalization and particle deposition profile

The initial radial distribution of the lithium ions deposited by the ablated pellet can be derived from the pellet ablation rate. It was shown earlier that for typical plasma conditions, the Li^0 gas from the ablating pellet can expand to about 5 mm. After that, the Li atoms are ionized and captured by the magnetic field at a certain radius r. Thus, with the accuracy of about 1 cm, the initial number of Li ions located at the magnetic surface with radius r and thickness dr is equal to the amounts of Li atoms $\dot{N}\,dt$ ablated at radii $-r$ and r:

$$\dot{N}(-r)dt + \dot{N}(r)dt = n_{\mathrm{Li}}(r)dV = 4\pi^2 R\frac{a_s}{a_l}n_{\mathrm{Li}}(r)\,r\,dr \tag{2.7}$$

where $n_{\mathrm{Li}}(r)$ is the lithium ion density, R is the major radius, a_s (a_l) are the shorter (longer) minor radius of the ellipse (pellet is injected along a_l).

The relation between time and radius r is determined as

$$t = t_0 + \frac{r}{V_{\mathrm{p}}} \tag{2.8}$$

where t_0 is the time when the pellet passes the plasma axis, V_{p} is a pellet velocity.

Replacing dr by $V_{\mathrm{p}}\,dt$, the profile $n_{\mathrm{Li}}(r)$ is calculated from (2.7) as

$$n_{\mathrm{Li}}(r) = \frac{\dot{N}(-r) + \dot{N}(r)}{4\pi^2 R V_{\mathrm{p}}\frac{a_s}{a_l}r} \tag{2.9}$$

There is a singularity when $r \to 0$, which is resolved by the mentioned above accuracy limit of ~1 cm. Moreover, the pellet may move off the plasma axis because of the trajectory scattering, which is typically within 1° in full angle, resulting in the maximal deviation $\Delta r \approx 1.5$ cm at the plasma center (See, for example, Fig. 14b)).

Thus, the profile (2.9) should be capped within $r < \Delta r$ with conservation of the volume integral:

for $r < \Delta r$ $$n_{\mathrm{Li}}^{\max} = \frac{2}{\Delta r^2}\int_0^{\Delta r} n_{\mathrm{Li}}(r)\,r\,dr, \tag{2.10}$$

where $n_{\mathrm{Li}}(r)$ is calculated from Eq. (2.9).

As it was said in Section 2.6.2, the pellet ablation rate is directly proportional to the light emission of low-charge ions. Therefore, for calculation of the ablation rate, the time dependence of Li I intensity $I(t)$ presented in Fig. 13 was used:

$$\dot{N}(t) = C\, I(t) \tag{2.11}$$

where C is a proportionality coefficient to be found from normalization.

The normalization can be done by integrating Eq. (2.7) for the time period of phase 1 and phase 2 and setting the integral equal to the measured increase of the electron density after the injection. However, the density measurement by FIR interferometer provides information only about the line integral of the density, but not the density profile. The data of Thomson scattering have typically good spatial resolution but only a few measurements in time, which is insufficient if the information about the fast density jump due to the injection is required. For these reasons, the density profile before the injection is expressed as

$$n(r) = n_0 S(r) \tag{2.12}$$

where $S(r)$ defines the shape of the density profile ($S(0) = 1$) that fits to the Thomson data and n_0 is the central density, which is easily obtained (for the given $S(r)$) from the interferometer signal along the central chord just before the injection.

The density profile right after the injection is treated as a sum of (2.12) and $n_{Li}(r)$:

$$n'(r) = n_0 S(r) + Z\, n_{Li}(r) \tag{2.13}$$

where Z is an effective ionization state of the Li ions right after the injection.

The line integral of $n_{Li}(r)$ is now calculated from the interferometer data n_l before and after the injection:

$$2Z \int_0^{a_l} n_{Li}(r)\, dr = n_l' - n_l \tag{2.14}$$

Combining this with $n_{Li}(r)$ from Eqs. (2.9) and (2.10), one can finally obtain a formula for the normalization coefficient C:

$$C = 2\pi^2 R V_p \frac{a_s}{a_l} \frac{1}{Z} \frac{n_l' - n_l}{\int_{\Delta r}^{a_l} \frac{I(-r)+I(r)}{r}\, dr + \frac{2}{\Delta r}\int_0^{\Delta r} \big(I(-r)+I(r)\big)\, dr} \tag{2.15}$$

Thus, the deposition profile of the Li ions $n_{Li}(r)$, which is the initial condition for the transport simulation, is calculated as

$$n_{Li}(r) = \frac{P}{2}\frac{I(-r)+I(r)}{r} \qquad \text{for} \quad r > \Delta r \tag{2.16}$$

$$n_{Li}(r) = \frac{P}{\Delta r^2}\int_0^{\Delta r} \big(I(-r)+I(r)\big)\, dr \qquad \text{for} \quad r < \Delta r \tag{2.17}$$

with parameter

$$P = \frac{1}{Z} \frac{n_l' - n_l}{\int_{\Delta r}^{a_l} \frac{I(-r)+I(r)}{r}\, dr + \frac{2}{\Delta r}\int_0^{\Delta r} \big(I(-r)+I(r)\big)\, dr} \tag{2.18}$$

It should be noted that the parameter Δr, which determines the width of the capped area around $r = 0$ of the initial profile $n_{Li}(r)$, has a weak effect on the subsequent evolution of the lithium ions, because all irregularities on the profile are rapidly smoothed by the diffusion.

It is seen from Eq. (2.16) that the initial distribution of the lithium ions has a peaked form, which means that the shape of the electron density profile after injection is quite different from that of before the injection. Therefore, the Thomson data used for obtaining $S(r)$ profile in Eq. (2.12) should be taken for the plasma before injection.

2.7.2. Simulation of the lithium ions diffusion

Simulation of the diffusion of lithium ions was performed by means of a computer code for impurity transport [34]. The one-dimensional code solves the particle balance equation (1.1) for a set of plasma ions, hydrogen isotopes plus several charge states of one or more impurity elements. The code includes both neoclassical and anomalous transport for toroidal configuration. The particle source is calculated by means of several models of atomic rates for all ion species.

The experimental data of electron and ion temperatures, plasma density, plasma effective charge and others are used as input parameters. Profile of lithium ions deposited by the pellet (calculated from (2.16) and (2.17)) is used as initial condition for the simulation. The particle balance equations is simulated directly with a given values for diffusion coefficient D and pinch velocity V. For a long time scale simulation, the lithium ions are completely ionized and the calculated profile of Li^{3+} is compared with the one measured experimentally. The coefficients D and V are adjusted so as to achieve optimal agreement with experimental profile evolution.

Fig. 16 shows the evolution of Li^{3+} ions profile measured by observing the CXRS emission of Li III line as described in Section 2.5. The first profile (at 370 ms) is smaller than expected because of the integrating interval of 20 ms, while the pellet was injected at 378 ms. The emission is suppressed for two last profiles (at 450 ms and 470 ms) because the NBI was turned off at that time.

Results of the simulation are shown in Fig. 17 as time dependencies of Li^{3+} density at the center. Three simulated curves are shown for different values of the diffusion: $D = 0.1$ m^2/s (dash-dot line), 0.15 m^2/s (solid line), 0.2 m^2/s (dashed line). The inward pinch velocity of 1.0 m/s is the same for these cases. The recycling of Li particles is taken negligibly small for this simulation. These curves are compared to the Li III intensity evolution measured experimentally from CXRS and VUV. It is seen, that the best agreement with the experimental data is achieved for $D = 0.15$ m^2/s.

It should be noted that the form of profiles shown in Fig. 16 can be better reproduced if coefficient D is taken as increasing from center to periphery. In the simulation, this dependence was input in the form of Alcator scaling (See Eq.(1.21)) and therefore, the values of D shown in Fig. 17 should be interpreted as the average of the radial profile.

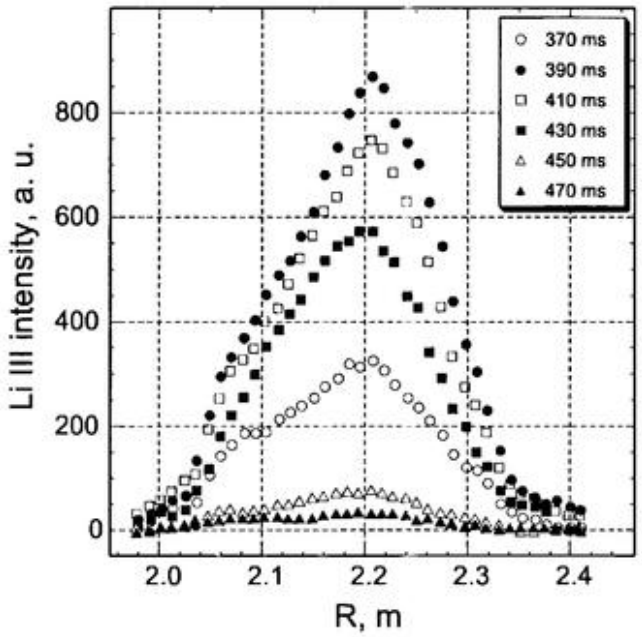

Fig. 16. Profiles of LIII intensity (449.9 nm) from 370 ms to 450 ms. The Li pellet is injected at 378 ms. The magnetic axis is located at $R = 2.2$ m.

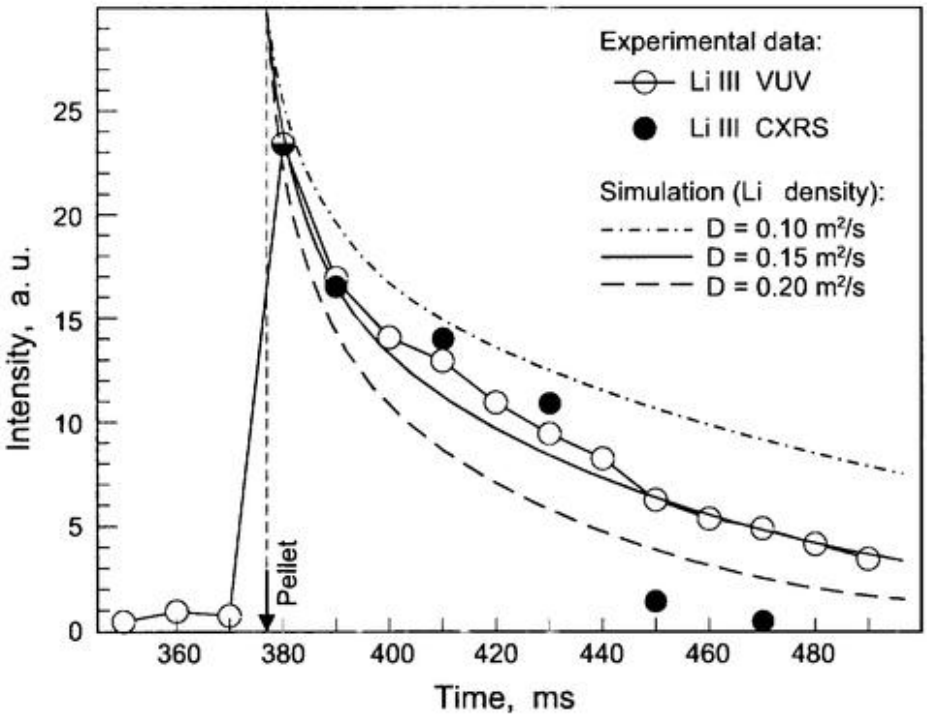

Fig. 17. Time evolution of Li III intensity measured experimentally from CXRS (closed circles) and VUV (open circles). Simulation results are shown as continuous curves. Three different values of D and fixed value of V (1.0 m/s) are given.

2.7.3. Electron density balance and impurity recycling

It was said earlier (see Section 2.6.1) that injection of a lithium pellet results in an increase of the plasma density by a factor of 1.5–3. 0. After the injection, the percentage of Li ions contents in plasma ranges from 16 to 66%. For such a large ratio, the diffusion of Li ions affects significantly the electron density, due to the conservation of electric charge. Thus, the transport of Li ions is very much coupled with the transport of electrons of the background plasma. For this reason, when adjusting the simulation parameters, it is necessary to take into account the evolution of the plasma density as well.

The line integral of electron density calculated according to the simulated Li^{3+} evolution is compared to the experimental data of FIR interferometer in Fig. 18. Note at first, that the plasma density does not show such a steady decay as does the Li III intensity in Fig. 17, that is explained by the increasing total amount of the bulk plasma ions due to the NBI. Therefore, the background ion density was assumed to grow linearly according to the rate of about 2.3×10^{20} ions/s. The other parameters of the simulation are the same as in Fig. 17.

It is seen that after injection, the interferometer signal is slowly going up for about 5 ms before it starts decreasing. For a constant total amount of particles, this could be explained by a rearranging density profile. Namely, the line integral is larger for a more peaked profile with conservation of the volume integral. However, as it was shown in Section 2.7.1, the initial profile of Li^{3+} ions has already a peaked form,

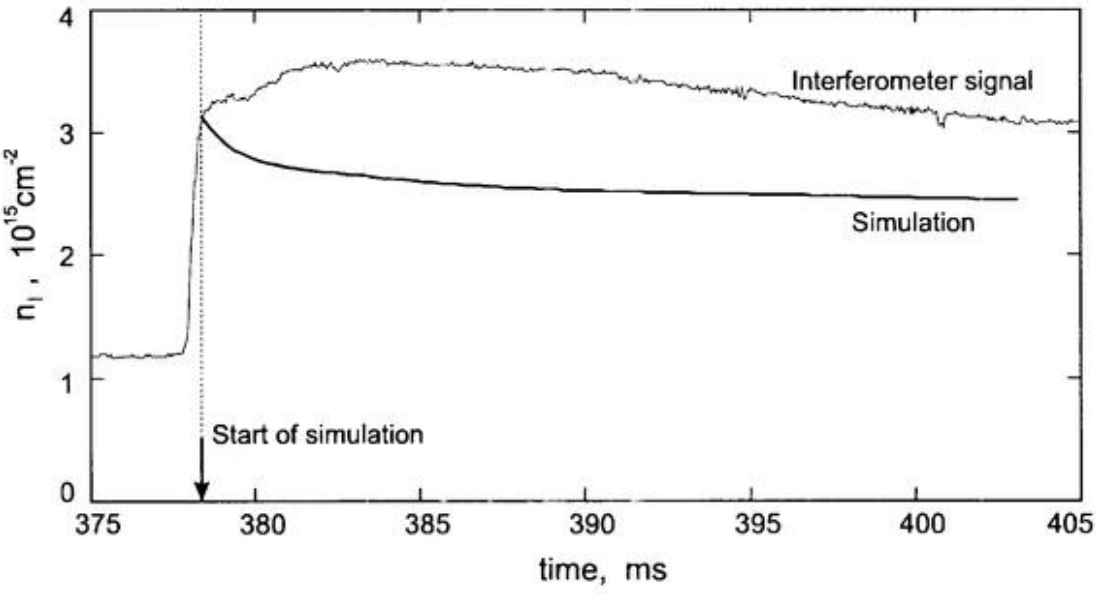

Fig. 18. FIR interferometer signal and the line integral of electron density calculated from the simulated Li^{3+} evolution.

which should apparently be smoothed soon because of the diffusion. This will result in a decrease of the line integral of density, which is demonstrated by the simulated curve in Fig. 18. Moreover, the continuous decay of Li ions contents in plasma also counts in favor of decreasing line integral.

Thus, such an increase of the interferometer signal can be explained only by an extra source of Li^{3+} ions. An origin of this source can be a continuing ionization of partly ionized Li ions remained after injection. However, the full ionization of Li ions can last not longer than a few hundreds microseconds. Another factor, which easily resolves the inconsistency, is a strong source of Li atoms originated from the residual Li pellet on the wall. The rate of such a puffing can be estimated from the time evolution of Li II intensity during phase 4 in Fig. 13, using the normalization obtained in Section 2.7.1. The use of Li II intensity is more correct here than the Li I, since emission of Li^{+} ions at the plasma edge is a clear indicator of the amount of impurity entered the plasma.

Effect of the impurity puffing can be also seen in Fig. 16 as a small addition to the Li III profile at $R = 2.06$–2.08 m, which vanishes after ~40 ms. This corresponds to the inboard side of the torus and agrees with the location of the pellet residual (See Fig. 10). Such an addition, but smaller, is also seen at the opposite side of the profile at $R = 2.31$ m, $t = 370$ ms.

The impurity puffing is effective when the impurity recycling is non-zero. So, the influence of this factor was also included in the analysis. Results of the simulation are presented in Fig. 19. The solid curve corresponds to the simulation when the best agreement with experimental data was achieved. The model included impurity puffing from the pellet residual, recycling coefficient of 0.25 and partially ionized Li ions as initial condition (40% – Li^{2+} ions and 60% – Li^{3+}). Three alternative curves are also shown corresponding to the simulation when each of the factors was switched off in turn. One can see, that the beginning of the experimentally observed evolution (about 10 ms after injection) is reproduced rather well if all three factors are taken into account. The role of each factor at different time scales is also seen: full ionization is completed within a millisecond, evaporation of the pellet residual lasts for 5-10ms, the impurity recycling has continuous effect.

The simulation disagrees with the interferometer signal at longer time scale. At this time, the transient processes are becoming extinct and the electron balance is determined by a variety of other factors that are difficult to estimate, and this is not the purpose of the current study.

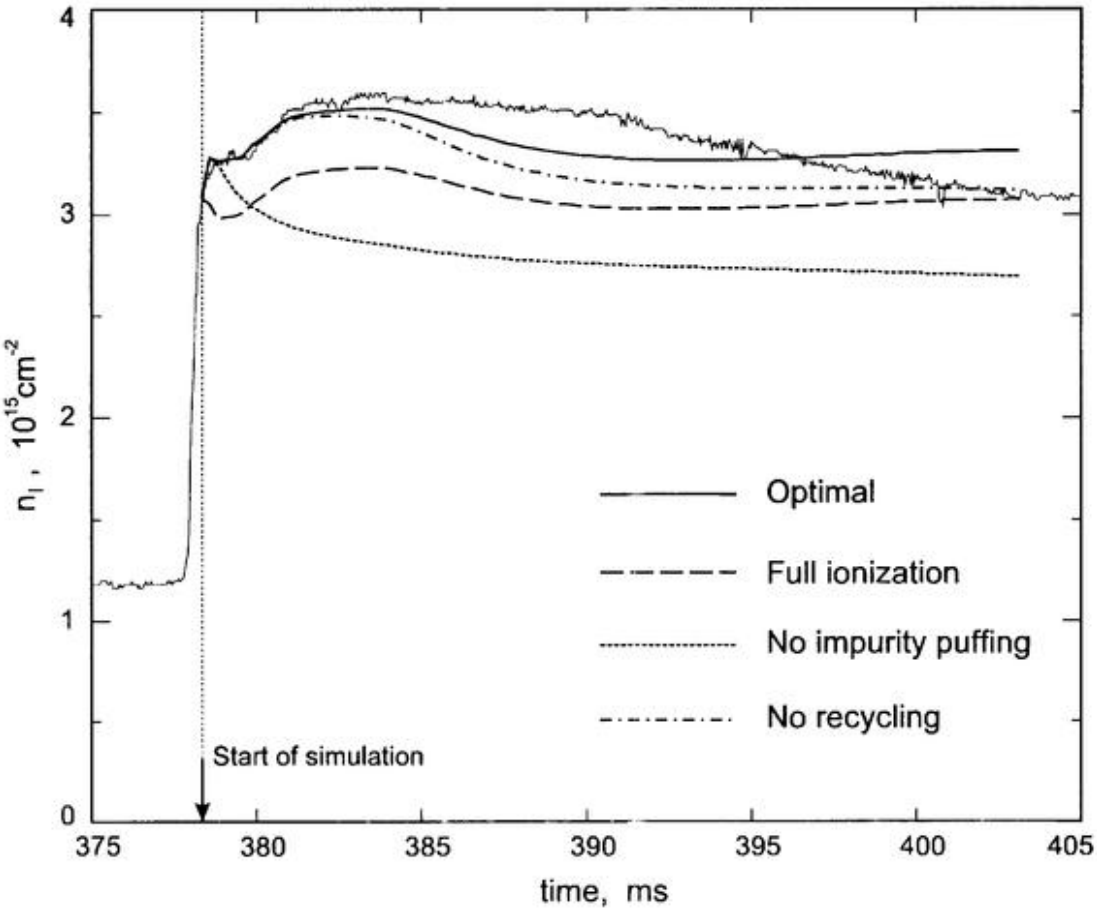

Fig. 19. Comparison of FIR interferometer signal and results of simulation: all factors included (solid curve), no partial Li ionization (dashed curve), no impurity puffing from the pellet residual (dotted curve), no impurity recycling (dash-and-dot curve).

2.8. Summary

This chapter was devoted to the experiments with lithium pellet injection and the analysis of transport properties of lithium ions.

The construction of the pellet injector and a special technique of preparation of the Li pellets has resulted in a high purity of the injected Li pellets. The lithium pellet injector has been installed on Heliotron E and demonstrated a reliable operation. The light emission from the ablating pellet in plasma was measured in LiI and Li II lines

simultaneously with high time resolution. The obtained images of the pellet cloud have allowed to estimate main characteristics of the lithium ions in various charge states. The time evolution of Li I and Li II intensities provided important information about the atomic processes taking place during the pellet injection.

The subsequent motion of the lithium ions has been analyzed by means of the impurity transport model with the initial radial distribution of Li ions calculated from the observed pellet ablation rate. Simulation of the Li ions transport has allowed to calculate the diffusion coefficient and the pinch velocity. It was demonstrated that the experimental data can be reproduced properly if the impurity puffing from the wall and the impurity recycling are taken into account.

The long time scale diffusion of Li ions is difficult to simulate correctly, as the transport task becomes not dynamic, but static and requires an account of a variety of factors. Because of the non-local initial distribution of the lithium ions, there is no clear transient process except for the relaxation of the Li ions profile as a whole. The analysis of the impurity transport is complicated also by a rather large impurity contents in the plasma after injection. The impurity transport becomes coupled with the transport of electrons and these two processes can not be considered independently.

All this suggests the use of a small perturbation of impurity contents confined initially to a small volume in a plasma, supporting the idea of the tracer-encapsulated pellet introduced in Section 1.3.

3. TRACER-ENCAPSULATED CRYOGENIC PELLET

3.1. Introduction

Concept of the tracer-encapsulated cryogenic pellet (TECPEL) injection was described in Section 1.3 as an accurate diagnostic system to measure particle transport both in parallel and perpendicular to the magnetic field lines in magnetic confinement devices. The particle transport can be measured by observing the motion of the tracer particles deposited in a limited plasma volume by the core of TECPEL.

The TECPEL consists of a small core made of light atom such as lithium, carbon, etc., which is encapsulated in the center of a pellet made of frozen hydrogen isotope. In order to deposit the tracer material in the localized area, the typical diameter of the core is from 50 to 250μm for a plasma temperature in the keV range [22]. In this case, the typical length of the pellet flight during ablation of the core is around 1 cm. This localization can be adjusted with pellet size and pellet velocity depending on plasma parameters such as electron temperature. The relation between the location of the tracer particle deposition in the plasma and the pellet size is studied with pellet velocity as a parameter in Reference 22. As an example of an application of the TECPEL, it was demonstrated that for a plasma of the Large Helical Device (LHD) [35], the outer pellet diameter should range from 1 mm to 3 mm and the appropriate diameter of the core should be in the range of 50–250 μm.

As for cryogenic pellet production technology, there are three basic techniques for pellet formation in existing injectors: direct freezing in a gun barrel, known as *in situ* condensation, or pipe gun [36, 37], extrusion [38, 39] and pellet formation inside a rotating or sliding disk [40, 41]. For the present purpose, a sliding disk system was adopted because of its advantage, comparing to a pipe gun type, of being able to accurately define the pellet length.

For a technical demonstration of the device producing tracer-encapsulated cryogenic pellets, a cylindrical form of the pellet was chosen: the outer diameter of 3 mm with the length of 3 mm. The inner core is made of carbon with diameter of 240 μm in a sphere form.

3.2. Configuration of TECPEL injector

The essential idea is to use the softness of a cryogenic hydrogen isotope, which also sets the practical limit for acceleration of the order of 4 km/s. The main sequence of the production process of a tracer-encapsulated cryogenic pellet is:

1) producing a cryogenic hydrogen isotope pellet as usual,
2) inserting the tracer into the pellet,
3) covering the hole of the pellet with solid hydrogen isotope,
4) ejecting the whole pellet with a propellant gas.

A schematic of the operation of a cryogenic unit of the injector for producing a tracer-encapsulated cryogenic pellet is shown in Fig. 20. The major part of the cryostat, a cryohead *1*, is made of oxygen free copper (OFC). The width and depth of the OFC cooling block are both 30mm. The cooling channel is formed by a zigzag groove on both sides. The cryohead consists of two blocks brazed together to form a slot. This slot holds the main disk *2* and the sub disk *3*, which are made of stainless steel (SUS) and have a form of thin rectangular plates. The thickness of the main and sub disks are 1.6 and 1.4 mm, respectively, and the width is 10mm for both. The tolerance between the disks and the slot is 15 μm.

The disks are driven in vertical direction by a vertical driving system. A horizontal driving system is used for driving the supplier mechanism to insert a tracer material into the pellet with a high accuracy of 5 μm. The maximal moveable distance is 50 mm for horizontal direction and 120mm for vertical direction. The driving is provided by means of two stepping motor systems with linear scale position sensors (Mitutoyo AT112).

The movement of the main and sub disks is operated by a single driving system in the following way. The main disk *2* is connected with bolts to the shaft *6* with a diameter of 10 mm. This shaft has a round disk *6* with diameter of 30 mm at the lower position, whose purpose is explained below. The sub disk *3* is connected to the shaped shaft *7* mechanically. The top disk *8* of the shaft *7* has diameter of 30 mm. At the top plate *8*, the spring *9* is set to push the sub disk *3*. Four characteristic positions of the main and sub disks are indicated with encircled letters. While the main disk is moving up from the bottom position **A**, the sub disk remains in its lowest position **C** because of the pushing spring *9*. When the main disk *2* is lifted up 68 mm from the bottom position, then the round disk *6* reaches the top disk *8*, which starts to pull up the shaft *7*. Thus, the main and sub disks are moved up together until the position **D**. When the main disk *2* is driven down, the sub disk *3* will move down automatically due to the force of the spring *9*.

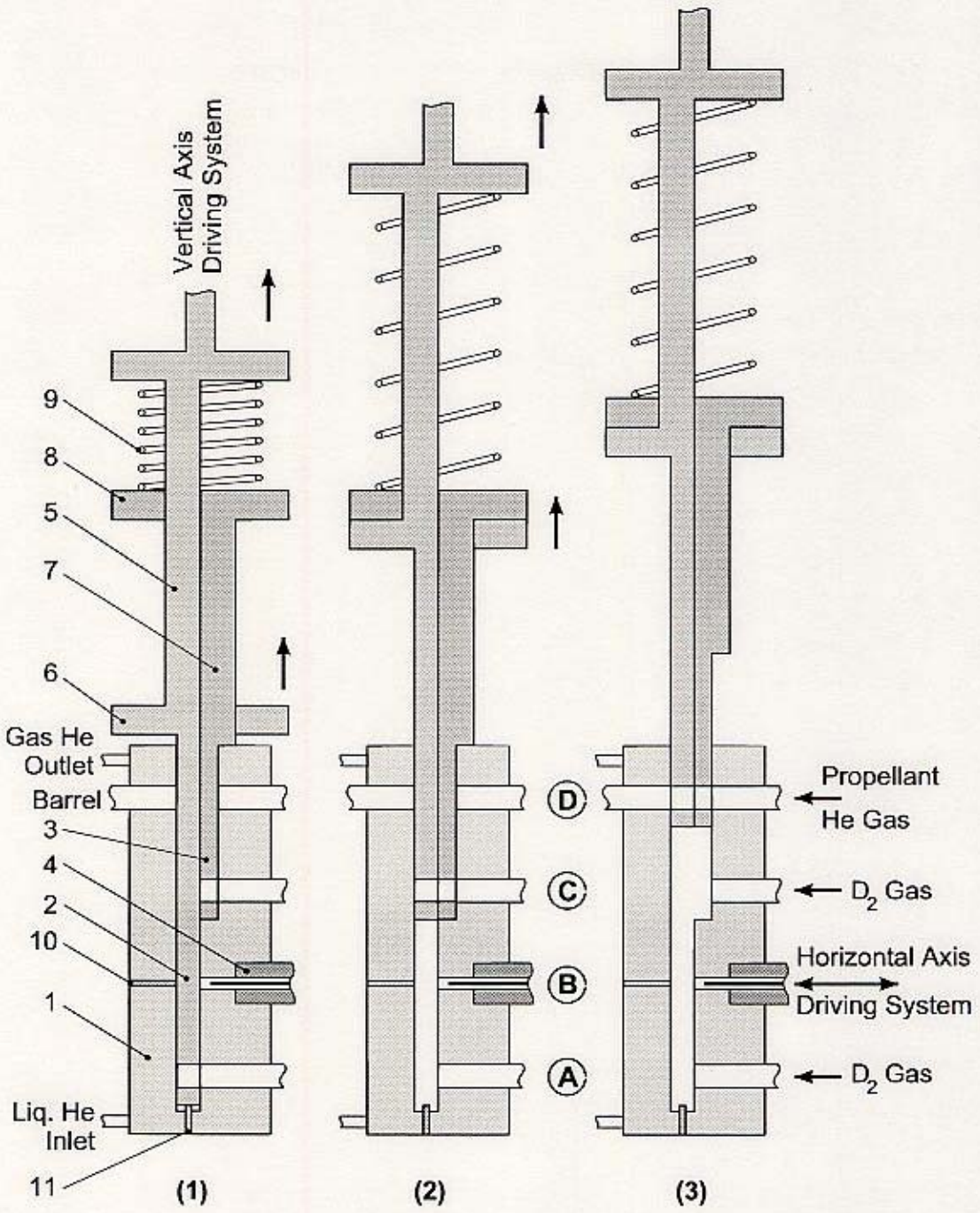

Fig. 20. Schematic of the cryohead part of the device for producing a tracer-encapsulated cryogenic pellet. Three typical states are indicated as (1), (2), and (3).

The main and sub disks are connected to the motor drive shaft with mechanical coupling outside of the vacuum chamber. The feedthrough of the shafts of the disks is sealed with a double O-ring. The bottom part of the housing of the cryostat is supported with three Invar rods, and the top part is connected to the top flange of the vacuum chamber through bellows. The bellows compensates the thermal contraction of the housing in the vertical direction during the cooling of the cryostat. As for the horizontal direction, the vacuum flange for the shaft of the horizontal driving system has also bellows for compensating the contraction in horizontal direction. The thermal contraction of the OFC block with a length of 153 mm is 450–600 μm, depending on the temperature profile of the module. The locations of the pellet production and the core supplier, which are shifted after cooling, are also adjusted by monitoring the new position with electric sensors (contact switches) *10* and *11*, which are set up in both directions. The sensors consist of stainless steel and epoxy resin (Stycast 2850FT) as insulating material.

For the precise manufacturing of the cryohead, a special brazing method in vacuum has been used, and the whole device has been successfully completed.

3.3. Method of TECPEL production

The procedure of the production method of a tracer-encapsulated cryogenic pellet is clarified in Fig. 21, where six typical phases of the operation are marked from (1) to (6). For each phase, a position in vertical direction is indicated with encircled letters according to Fig. 20.

At first, hydrogen isotope gas is introduced to form a partial pellet with thickness of 1.6 mm in the main disk as shown in (1) of Fig. 21. Then, the partial pellet is moved up to position B for inserting a core. The accuracy of the position B should be maintained within 5-10 μm. A tungsten wire is pulled out horizontally at first (2) to pick up a light atom core from the "tracer storage", which is organized as a stack. The typical number of stored cores is 20. One tracer core is supplied automatically from the stack when the tungsten wire reaches the position as shown in (3). This is done with a pushing spring placed at the top of the vertical tungsten wire. Once a tracer core is supplied, the horizontal tungsten wire pushes it until the core is inserted into the partial pellet (4). Then, the partial pellet containing the tracer core is transferred to the position C, where the hydrogen isotope gas is introduced again as shown in (5). Thus, the additional pellet with thickness of 1.4 mm is formed in order to cover the

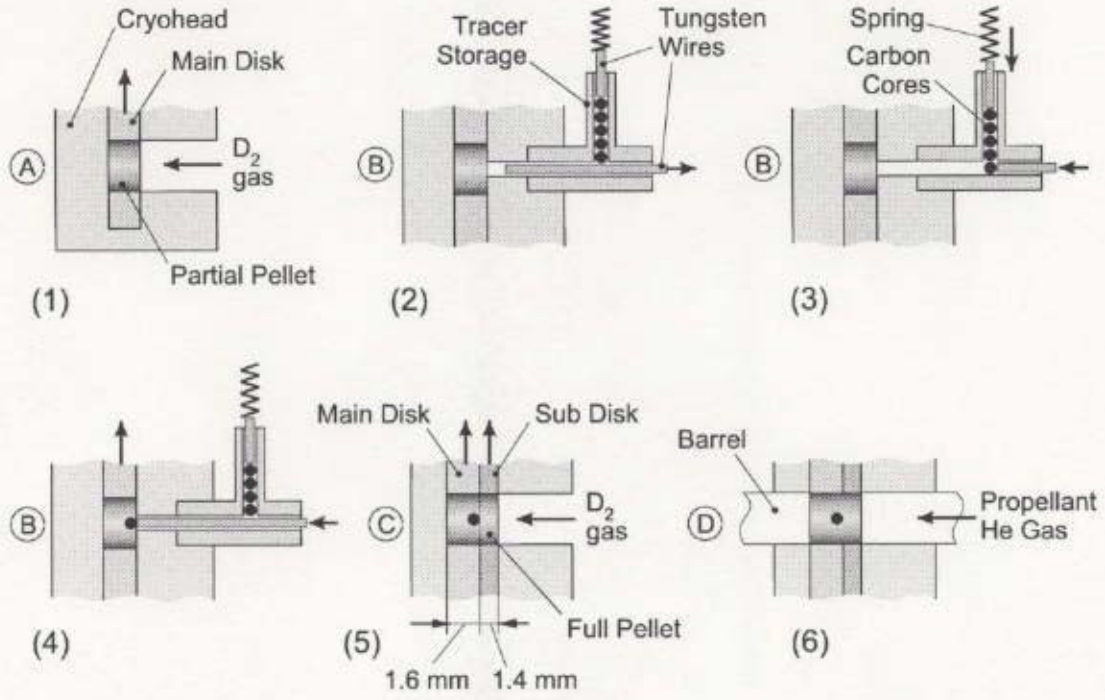

Fig. 21. Principle of the production method of a tracer-encapsulated cryogenic pellet.

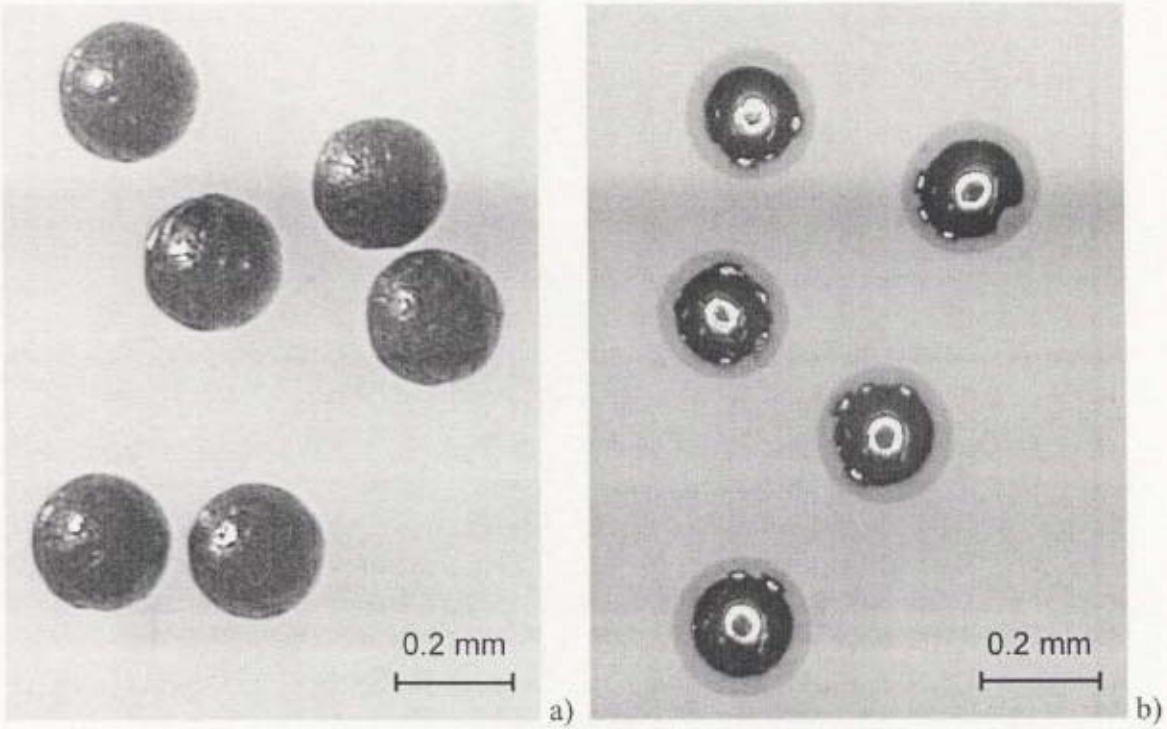

Fig. 22. Sample photo of carbon spheres with a diameter of 230–240 μm used as tracer cores.

exposed part of the core with hydrogen isotope. In this way, the full pellet is completed and transferred further to the position D as shown in (6), where it is accelerated through the barrel by a high pressure gas.

In these experiments, carbon or titanium spheres with diameter of 230–240 μm were used as the tracer cores. A photo of carbon cores is shown in Fig. 22. The tungsten wire with a diameter of 230 μm is moved in a 250 μm guide channel. Tungsten is more appropriate from the viewpoint of its stiffness. Stainless steel, for example, is too soft to produce such a thin wire for the present purpose. The thin tungsten wire, however, can be easily broken due to the friction inside the guide, so special consideration of issues, such as driving speed and wire connection, is necessary.

The TECPEL production procedures are controlled by an automatic remote control system with two personal computers and I/O capacity of a 128 channel digital input, a 48 channel digital output, a 16 channel analog input, and a 16 channel analog output. The basic sequence for automatic and remote control is established b adjusting experimentally. The values of temperature and gas flow quantities should be finely controlled as follows: the temperature at the position C in Fig. 21 should be 12.8±0.3 K and hydrogen gas at 23±1 Torr is fed for 10–15 s at both positions A and C, thereby consuming the amount of 18 mg at each position.

The valve operation for gas feeding, pressure control, temperature feedback control with five temperature sensors (silicon diodes), and heaters at three different locations can be also done by the automatic system. With a mass flow meter, the real time flow rate and the integrated amount of the supplied gas can be monitored. The experiment shows that the stepping motor systems can drive the pellet carriers smoothly in spite of small clearances of about 15 μm.

3.4. Diagnostics of TECPEL structure

For the purpose of confirming the TECPEL structure as well as the correct operation of the device in all phases, the ejected pellets are photographed from two perpendicular directions simultaneously.

The schematic of the pellet observing system is shown in Fig. 23. The photography is performed by means of two digital CCD cameras installed above and on the left of the pellet flight path. A flying pellet is illuminated simultaneously from

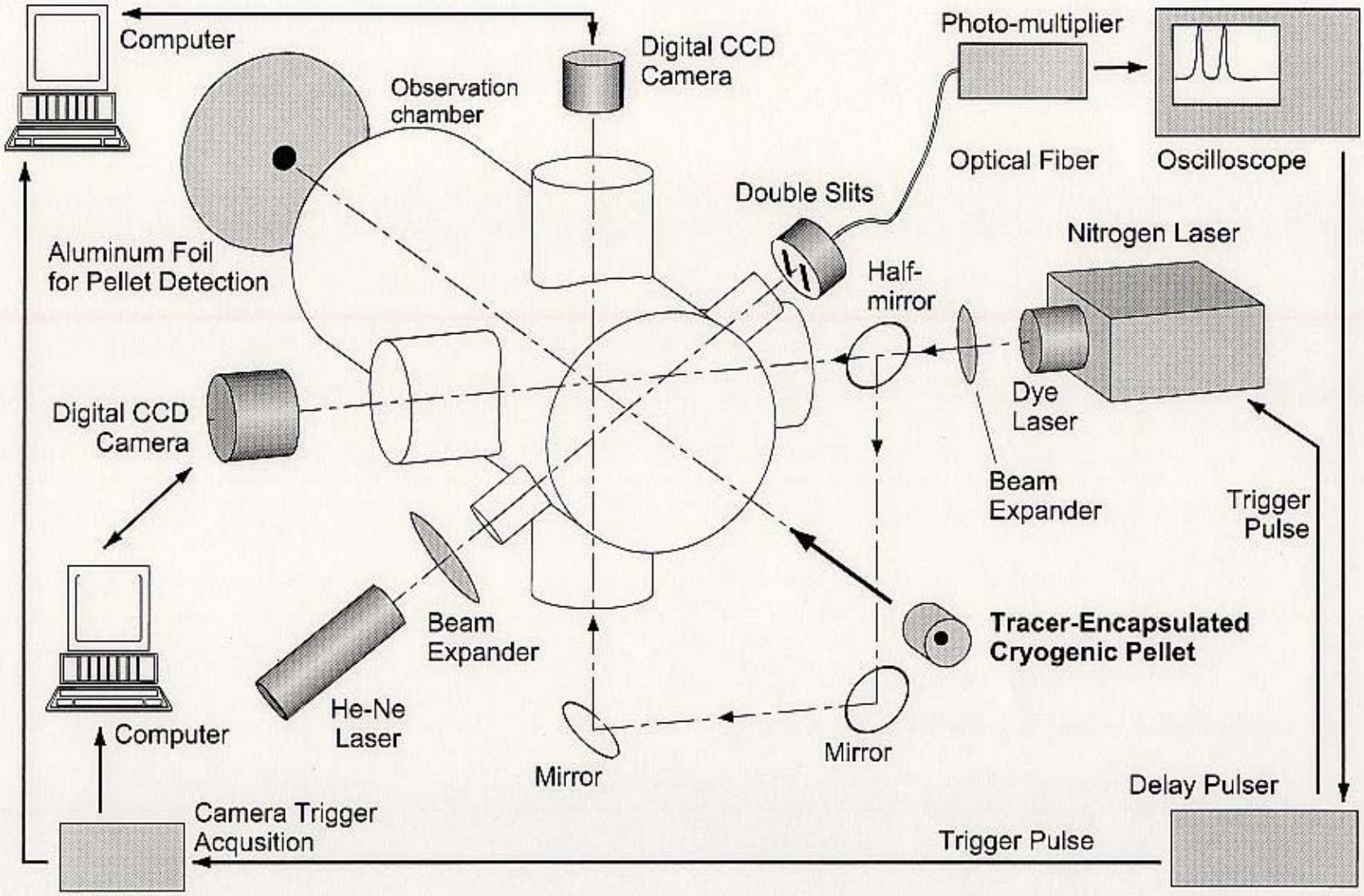

Fig. 23. Experimental set-up for observing a tracer-encapsulated cryogenic pellet.

two directions by two light beams originated from one light source of a short pulse laser split by a half-mirror. For both measuring the pellet velocity and triggering the fast light source, a 1 mW He-Ne laser beam is expanded to the diameter of 20 mm so that the beam can easily catch a pellet in flight. The expanded beam reaches the mask having two slits which are connected to a photo-multiplier through an optical fiber bundle. When the pellet passes across the He-Ne laser beam, then the detected light intensity decreases due to shadow of the pellet. The double slits allow to estimate the pellet velocity from two separate pulses, that is, with time-of-flight method. The typical pellet velocity is 400--800 m/s. The first pulse triggers the fast light source and the digital camera image acquisition after an appropriate delay with a preset delay circuit. For a direct detection of the pellet, an aluminum foil is located at the end of the pellet flight path. Its condition can be inspected through a glass window without opening the vacuum chamber.

For the fast light source, a dye laser is used, which is pumped with a nitrogen UV laser with a power of 75 kW and pulse width of 4 ns. The peak wavelength of the dye laser in case of Rhodamine 640 is 644 nm with spectral width of 80 nm. The pulse width is 3 ns and the output power is 20 kW. The use of this dye laser is necessary for obtaining a sharp and detailed image of a fast moving pellet. This is provided by the short pulse width of the illuminating laser, and also this resolves the problem related to the slow time response of a CCD camera. The spatial resolution of the image should be as high as possible in order to observe a tiny tracer core. For this reason, two high resolution digital CCD cameras are utilized: an Electrim EDC -1000U camera with 1134×972 CCD matrix elements and 8 bit analog-to-digital conversion, and a 12 bit Xillix M -1400 camera with 1317×1035 elements. Digital and analog cameras are set up at the same distance from the gun barrel outlet, with one looking in the vertical direction, and the other in the horizontal direction.

To avoid the cloud around the pellet which obscures the clear pellet image, the observation position is located about 250 mm remote from the gun barrel, although some gas on the pellet surface is often still seen.

Thus, the tracer-encapsulated cryogenic pellet has been successfully photographed from two perpendicular directions simultaneously. An example of the two images obtained is shown in Fig. 24 a), b). A photo of a scale fragment, which was located at the gun barrel outlet, is shown Fig. 24 c). Several other images of TECPEL with corresponding scales are shown in Fig. 24 d). The images clearly demonstrate the sound configuration of the tracer-encapsulated cryogenic pellet. After digitizing, such images are processed with a computer, as described in the following section.

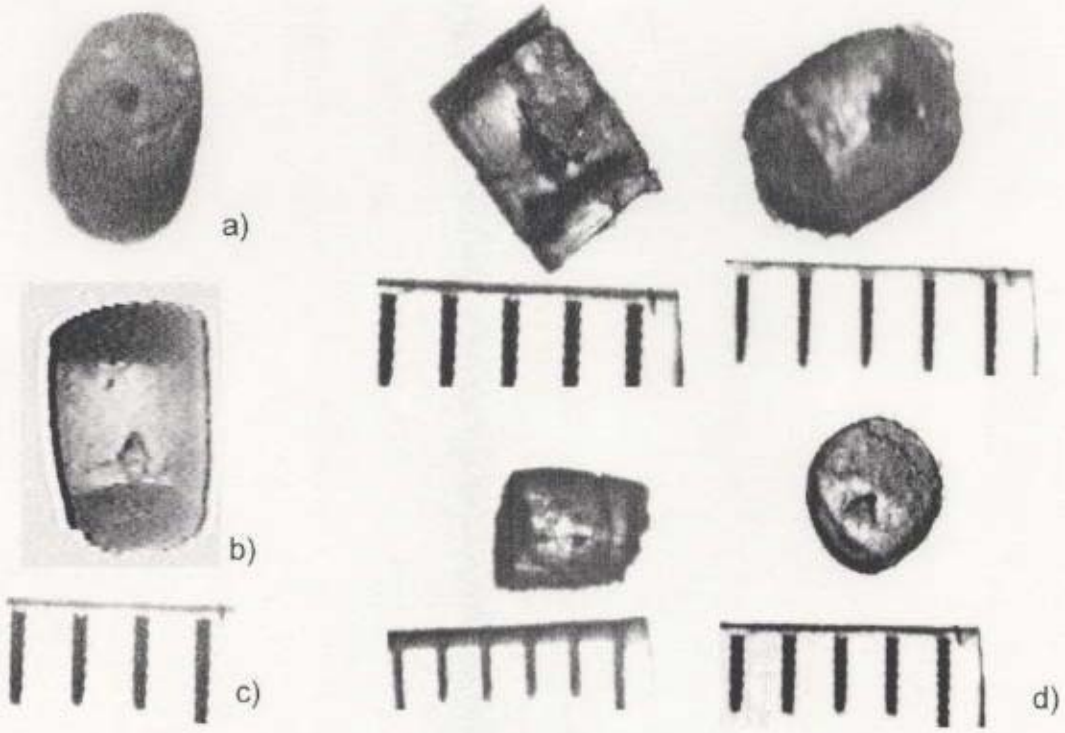

Fig. 24. CCD images of the tracer-encapsulated cryogenic pellet in flight. a) Pellet image made in horizontal direction (front view); b) Image of the same pellet made in vertical direction (top view); c) Photo of the corresponding scale (1 mm unit); d) Other images of TECPELs with corresponding scales.

3.5. 3D reconstruction of pellet geometry

The two obtained images of the tracer-encapsulated cryogenic pellet can be interpreted as projections of the pellet geometry on two perpendicular planes, and therefore, it is possible to reconstruct a 3D geometry of the pellet structure. This procedure has the following purposes:

1) Ensure the TECPEL integrity as a whole;
2) Confirm the existence of the real core inside the pellet;
3) Estimate the TECPEL dimensions and a possible displacement of the core;
4) From these, if necessary, adjust the operating parameters of the pellet injector during the TECPEL production.

The first step in the 3D reconstruction procedure is to determine a set of points in 3D space, which will represent vertices of the sought 3D pellet body. For that, the images shown in the Fig. 24 a), b) are used in the following way. Let us assume

that the top view contains (x,y) coordinates and the front view contains (x,z) coordinates (see Fig. 25). First, it is necessary to define several pairs of points, taking one point in each pair from the top view and another from the front view. These two points in each pair should correspond to the one 3D point and therefore their x coordinates must be equal. It is more convenient to select such points along some contours, such as pellet edges and other peculiarities. Fig. 26 represents one example of the results obtained by the above procedure. The numbers 1–4 indicate the correspondence between the points of the front and the top views.

Around the middle of the pellet an auxiliary contour is artificially built in order to simplify further 3D reconstruction. The two

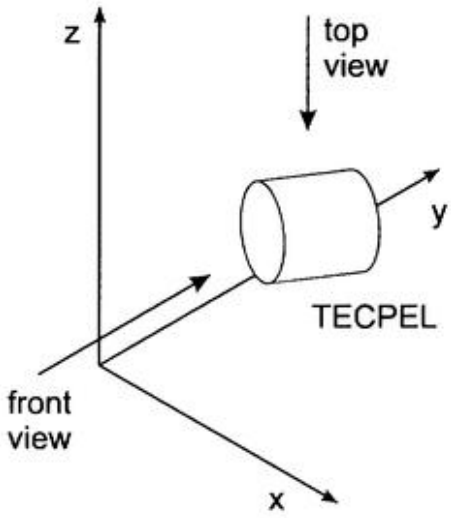

Fig. 25. Coordinate explanation of the top view containing (x,y) coordinates and the front view containing (x,z).

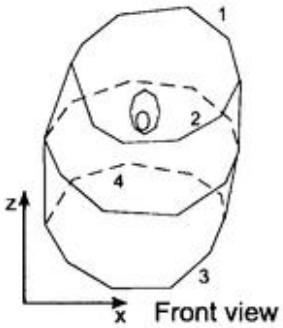

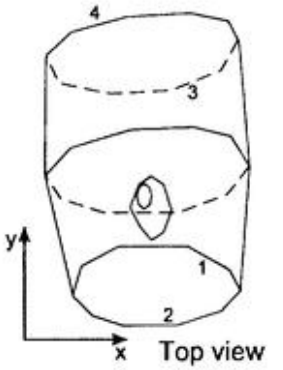

Fig. 26. The contours for determination of the pairs of points. The numbers 1–4 indicate the correspondence between the points of the front and the top views.

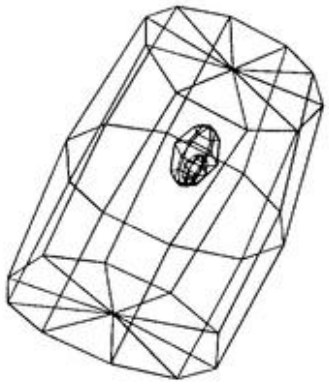

Fig. 27. 3D wire frame representing the reconstructed 3D geometry of the TECPEL.

inner contours represent the carbon core (the smaller contour) and a cavity around it (the bigger one). The cavity might appear due to melting of the pellet ice when inserting the carbon core with tungsten wire.

The next step is to build a 3D body based on the defined set of 3D vertices. This routine can be made in a 3D graphical editor, such as AutoCAD® software from Autodesk Inc. The result is shown in Fig. 27 in the form of a 3D wire frame. From the obtained 3D geometry, it is possible to determine the actual TECPEL dimensions. The calculated pellet length is 3.1 mm and diameter is 2.6 mm. This value of the diameter is less than the designed dimension, because of the possible evaporation of the pellet during acceleration in the gun barrel. It was found also, that the position of TECPEL's core is displaced along the pellet axis by 0.2 mm from the pellet center. This small shift is explained by a deeper insertion of the core by the tungsten wire during the phase 4 in Fig. 21.

The obtained 3D pellet body can be used for creating a virtual picture of the tracer-encapsulated cryogenic pellet. For that, the 3D structure is further processed in another 3D graphical editor. The process includes: smoothing the sharp edges of the 3D faces, locating some light sources around the object in 3D space, assigning special optical properties to its components (shininess, transparency, reflectivity) in order to imitate materials like ice or carbon. Finally, the 3D model of the pellet can be rendered and then displayed as if seen from any viewpoint in 3D space. Fig. 28 shows a sample picture of the rendered pellet model.

Fig. 28. One example of the 3D reconstructed virtual picture of the tracer-encapsulated cryogenic pellet.

3.6. Summary

Injection of a tracer-encapsulated cryogenic pellet is promising diagnostic system for an accurate measurement of the particle transport both in parallel and in perpendicular to the magnetic field lines in magnetic confinement devices.

A device for production and acceleration of tracer-encapsulated cryogenic pellets has been successfully constructed and tested experimentally. A typical configuration of the tracer-encapsulated pellet (TECPEL) includes a 50–250 μm diameter tracer made of light atom, such as lithium, carbon, etc. is encapsulated in the center of a 1–3 mm diameter cylindrical pellet of a frozen hydrogen isotope. For a technical demonstration of the device operation, a 240 μm diameter carbon sphere is encapsulated in the center of a ∅3×3 mm cylindrical hydrogen pellet. The full process of the TECPEL manufacturing is completely automated and controlled remotely by a computer-based sequencer. The produced TECPEL is accelerated by a light gas gun to velocities of 600–800 m/s at the test stand. The pellet is pho tographed from two perpendicular directions simultaneously in order to confirm the pellet integrity and the correct operation of the device. The two obtained high-resolution images of the pellet are then processed with a computer in order to reconstruct a 3D geometry of the TECPEL. The actual pellet size and the location of the TECPEL's core are determined from the reconstructed 3D geometry and found to be consistent with the projected dimensions. Thus, the proof-of-principle of the device operation has been successfully demonstrated.

4. TRACER-ENCAPSULATED SOLID PELLET

4.1. Introduction

Injection of the tracer-encapsulated cryogenic pellet (TECPEL) is a prospective diagnostics of local transport analysis. The concept of the TECPEL is described in Section 1.3 and the method of TECPEL production and acceleration is discussed in Chapter 3. The first TECPEL injector has been constructed and tested in the National Institute for Fusion Science (NIFS) [42]. This device is capable of injecting hydrogen pellets with a diameter of 3 mm and a length of 3 mm with encapsulated carbon core of 240 μm diameter. The successful operation of the injector has demonstrated a conceptual possibility of encapsulating a core inside of a frozen hydrogen isotope. However, the realized configuration of the TECPEL is appropriate for injection into a rather hot and dense plasma of a large machine, such as ITER, in order to achieve the necessary localization of the tracer. For existing fusion devices with a medium size plasma, the pellet size should be about 1 mm with a typical diameter of the core of 50–100 μm [22].

The outer diameter of the pellet affects the pellet penetration into a plasma, which can also be adjusted by the pellet velocity. The requirement of the smaller core size is more significant, since this directly determines the duration of the core ablation and hence the resulting tracer localization. On the other hand, this implies a special technology for the core preparation and handling during the pellet production. The necessity of smaller size for hydrogen pellets (i. e. diameter of 1 mm or less) also demands a high accuracy of positioning a core and an outer pellet in turn.

As an alternative to this direction, a tracer-encapsulated solid pellet (TESPEL) made of other non-cryogenic materials can also be a useful tool of the particle transport diagnostics. The idea of the TESPEL injection will be still advantageous if the emission of the core ions can be observed on the background emission of the major pellet ions.

Because of these reasons, several alternative configurations of a tracer-encapsulated pellet have been developed and tested, which is reviewed in the following section.

4.2. Selection of the TESPEL configuration

4.2.1. Hydrogen pellet with smaller core

One obvious way to advance the TECPEL configuration described in Chapter 3 is to reduce the size of the core, while retaining the pellet dimensions of ∅3×3 mm. The unchanged TECPEL sizes leave a possibility to employ the developed already method of TECPEL production along with the existing pellet injector.

The test experiments have been carried out with titanium spheres with a diameter of about 100 μm in order to develop a method of inserting such a tiny core into a frozen hydrogen pellet. For that, the tracer storage unit shown in Fig. 21 (2) has been modified in the following way. Instead of one vertical channel containing a stack of cores, a new device has 12 channels each loaded with a single core. The diameters of all vertical channels and the horizontal channel are 250 μm and all the tungsten wires have a diameter of 230 μm. The operation principle of the device is clarified in Fig. 29 and the top view of the device is shown in Fig. 30. For the first pellet, the horizontal wire is pulled back to the position of the leftmost channel where the first core is supplied. For each of the following pellets the horizontal wire is pulled back

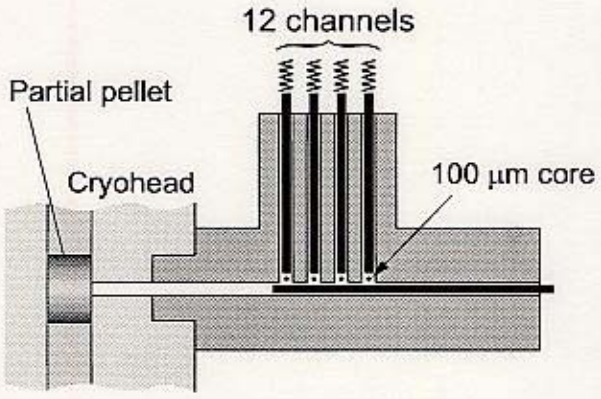

Fig. 29. Schematic of the device for supplying 100 μm cores.

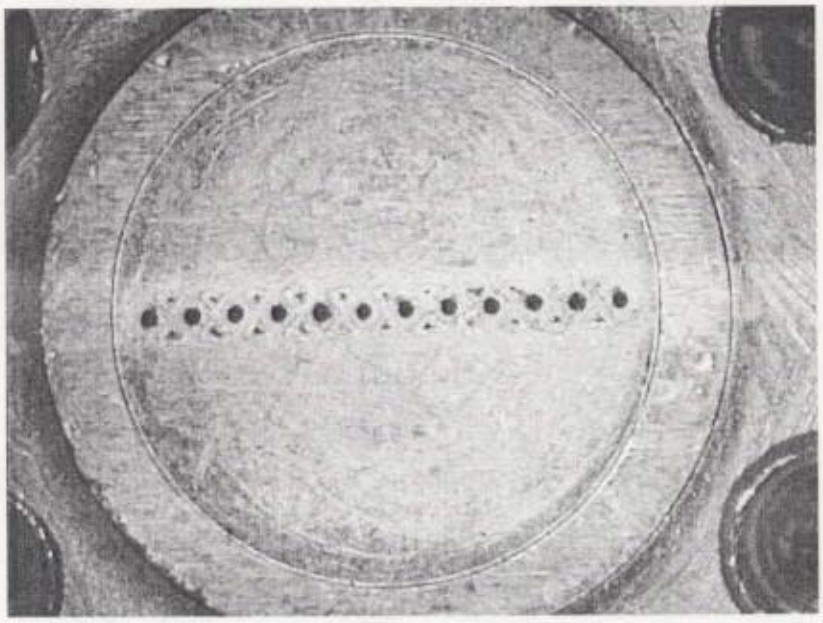

a)

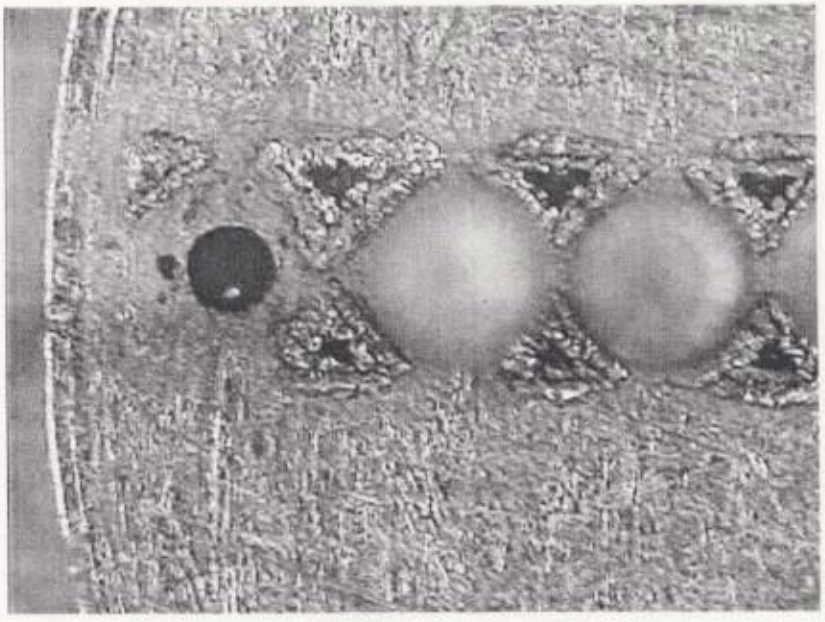

b)

Fig. 30. Photos of the device for loading 100 μm cores. a) Top view of the device. All 12 channels are open. b) Enlarged view of the left side of the device. In the leftmost channel a loaded titanium core is seen. Diameters of channels are 250 μm.

further, and thus, the other cores are supplied one by one from left to right. This eliminates a possibility of penetrating of more than one core at a time into the space before the horizontal wire.

The described construction of the tracer storage has one important advantage of being compatible with the described earlier TECPEL injector. Thus, the TECPEL production can be accomplished with the existing technology of the 230 μm tungsten wires and 250 μm channels.

However, several series of tests have revealed significant difficulties in achieving a stable operation of the device. The sequence of supplying of the 100 μm cores has often been interrupted. The next core in turn was sometimes not coming out as expected. This can be caused by existence of a "dead space" at the junction point of the horizontal and a vertical channel. An empty volume of about 100 μm size is always present between the flat end of the vertical wire and the cylindrical sidewall of the horizontal one, even when the one touches the other. If a core comes into this space it becomes inaccessible by none of the wires.

The achieved value of the average statistical reliability of the device operation is below 50%, and therefore, this method has been discarded.

4.2.2. Polystyrene shells inserted into hydrogen pellet.

It is still possible to remain within the present injector configuration with a reduced mass of the tracer core. If the core size is set to be unchanged, this means that the mass density of the core should be lower. This can be achieved by the use of a an empty core, or a shell with the wall thickness much smaller than the outer diameter. If the diameter of a shell remains in the range of 230–240 μm, then it can be handled with the process developed for the solid carbon cores, described in Chapter 3.

For the material of the shells, an organic polymer, polystyrene $(CH(C_6H_5)CH_2)_n$, has been chosen. Such polystyrene shells are originally produced for laser fusion experiments, in which they are used as fuel containers and pushers to be irradiated by powerful laser beams. The technology of the polystyrene shell production is now well established and allows obtaining shells with high sphericity and uniformity of the wall thickness [45, 46]. The shells can be produced with a diameter in the range of 0.2–7 mm and a wall thickness of 5–150 μm.

In the test experiments with the tracer storage unit shown in Fig. 21 (2), polystyrene shells with a diameter of 232–237 μm and a wall thickness of 10–15 μm. These experiments were aimed at achieving a high stability of the shell supplying sequence (one piece at a time), as well as finding optimal parameters for preserving the shell integrity.

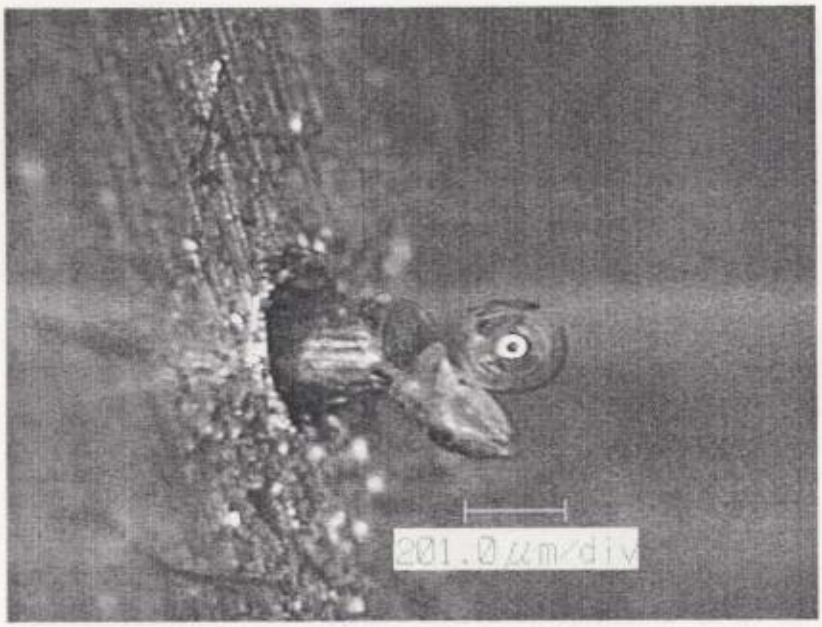

Fig. 31. Sample photo of the tungsten wire pushing out two polystyrene shells, one of which is broken.

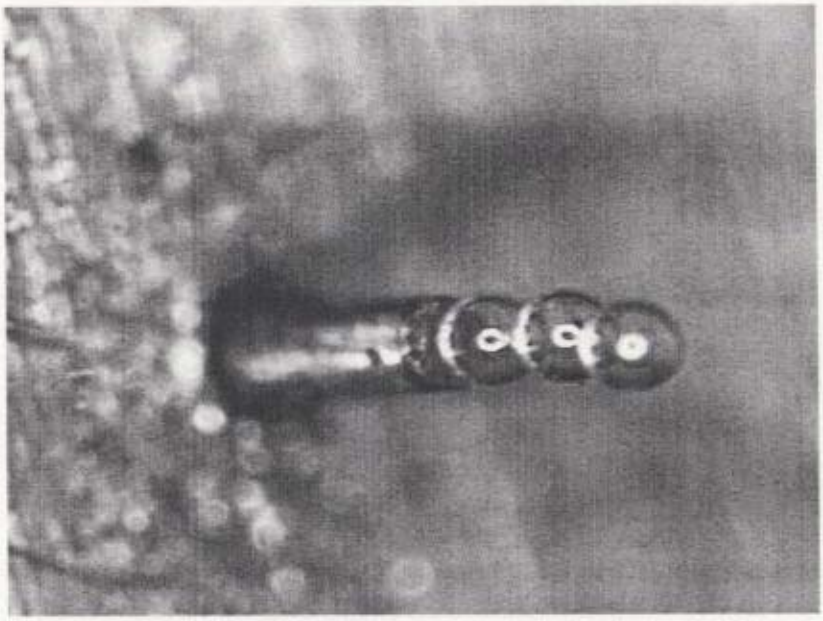

Fig. 32. Sample photo of three shells supplied simultaneously.

It was found that the shells can be operated safely if the wall thickness is not less than 15 μm. Otherwise, the percentage of the broken shells becomes too high. An example of the situation with a broken polystyrene shell is shown in Fig. 31. However, even if the shell stiffness is high enough, the order of shell supplying one at a time has turned out to be difficult to maintain. If a force of the spring pushing the vertical tungsten wire (See Fig. 21 (3)) is too low, then no shells can be supplied. If the force is too high, then two or more shells are pushed out of the vertical channel at once. An example of the latter situation is illustrated in Fig. 32. If the spring strength is intermediate, then these two situations may happen randomly, thus worsening the reliability of the operation to lower than 50%.

This can be explained by the influence of the two main factors. First, there is a static friction force, preventing the shells from coming out of the vertical channel. Second, because of the very low mass of a shell and a very smooth surface, several shells can easily slip into the horizontal channel at once. Typically, the maximal force of a static friction exceeds the dynamical friction force, which is quite enough to move several shells at once.

To overcome this problem, the tracer storage unit has been connected to a compact generator of the mechanical vibration. The vibration is generated by a piezo-electric crystal at a typical frequency of 170 Hz with duration of 0.5–1.0 sec during the phase (3) of Fig. 21. With this construction, the probability of the stable operation of the device has become over 90%. At present, the research in this direction is continuing and the improved construction is being prepared for the experiments with solid hydrogen.

4.2.3. Tests of other materials as a core.

It was said earlier that the tracer core should be made of a low Z material. The first candidate with the lowest Z value is lithium. Some properties of the lithium metal have already been discussed in section 2.3.1. Now the problem is to produce a very small amount of the substance with a typical size of 100 μm or less.

Because of the high physical adhesion of the lithium metal and its high chemical activity, it is rather problematic to produce such a small piece of lithium by a mechanical cutting. Therefore, an attempt has been made to produce small lithium spheres by a fast stirring of a melted lithium in another liquid. Such a liquid should be chemically inert to lithium and its viscosity should be comparable to that of the melted lithium, in order to produce a fine suspension from the two liquids. Thus, a small amount of melted lithium has been stirred in a high viscosity silicon oil at a typical temperature of 200–220°C. After cooling, numerous lithium spheres have been produced. However, the minimal size of these spheres is about 500 μm. This

procedure has been tested with silicon oils having various values of the viscosity, however the minimal size of a lithium sphere has not been reduced considerably. This can be explained by the fact, that the typical size of a liquid droplet is very much determined by a surface tension force. For liquid metals the surface tension is by one order of magnitude higher than that of organic liquids. The high surface tension becomes significant with smaller radius of a sphere and prevents it from being split further.

Because of these reasons, the procedure of obtaining small (<500 μm) quantities of lithium metal is very difficult to realize.

The other materials have also been considered as candidates for producing the tracer cores. Among those we can mention beryllium, boron carbide (B_4C), lithium hydride (LiH), lithium silicate (Li_4SiO_4), fullerene (C_{60}). (The latter, fullerene, is an interesting material as a form of carbon with relatively low mass density.) The common disadvantage of the tested materials is a rather irregular shape of the crystals or a too small typical size of the particles in a powder. This results in a significant inaccuracy when estimating the mass of the core to be injected into a plasma.

Among the considered substances, lithium hydride has been chosen as a core material for the tracer-encapsulated solid pellet, because of the following reasons:

1) Although it contains only half as much tracer atoms (Li) as pure lithium, the chemical activity of lithium hydride is much lower than that of lithium itself, which significantly simplifies the process of TESPEL production.
2) Lithium hydride contains no atoms with Z higher than that of lithium, which allows to keep the effective charge of the plasma at low level.
3) The typical size of the crystals in a powder of lithium hydride ranges from several μm to about 150 μm (See Fig. 33), which acceptable for the current purpose.

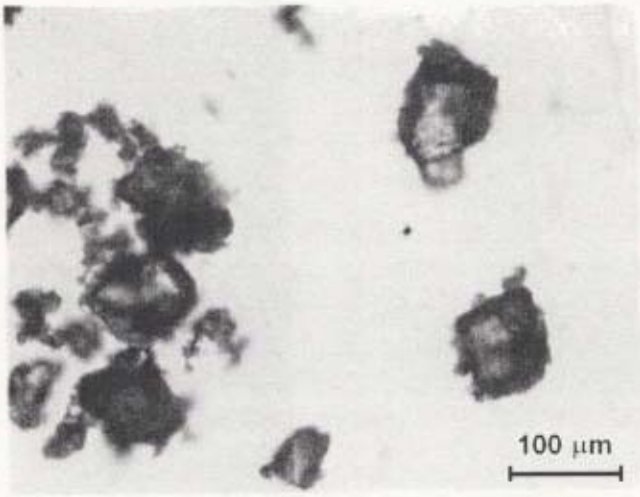

Fig. 33. Photo of the lithium hydride powder.

4.2.4. Covering lithium hydride with polystyrene.

It was shown earlier, that encapsulating of a very small (<100 μm) core into a frozen hydrogen is very problematic within the current technology. For this reason, other materials have been considered as alternatives to hydrogen pellet.

It is possible to cover the tracer core by coating in the atmosphere of a vaporized organic plastic material, such as polystyrene. For that, a piece of the tracer material, for example, lithium hydride, is located in a chamber filled with vapor of polystyrene. By adjusting the temperature in the chamber and duration of the coating process, it is possible to cover the tracer core with a polystyrene layer with required thickness. However, the typical time of this process is a few tens of hours, that increases considerably the TESPEL production costs.

Another way to form a tracer-encapsulated solid pellet is to use the ready made polystyrene shells described in Section 4.2.2 as containers for the tracer cores. For that, it is necessary to develop a method of inserting of small crystals of lithium hydride into the polystyrene shell. This problem has been successfully solved and the method is described in detail in Section 4.4.1. Thus, the proposed configuration of the tracer-encapsulated solid pellet includes a tracer core made of lithium hydride encapsulated into a spherical shell made of polystyrene.

The shell size should be chosen according to the following requirements:

1) Amount of electrons in the shell should be low enough, so that the increase of the electron density after the pellet injection does not terminate the target plasma;
2) The shell thickness should provide desired location of the deposited core atoms in a plasma, for given pellet velocity and background plasma conditions;
3) The pellet size should be large enough for handling (with a standard technology) and acceleration of the pellets.

For the purpose of injection to a medium size machine, such as CHS (Compact Helical System) [47], the shells used for TESPEL production have diameters in the range of 300–400 μm with wall thickness of 40–50 μm. In this case the total amount of electrons to be deposited in the plasma is $2.6–5.1\times10^{18}$ which is allowable for the total amount of electrons in CHS plasma of about 10^{19} particles. The location of the deposited tracer atoms and the deposition width in a plasma are determined by the pellet ablation rate. The calculation of TESPEL ablation is described in the following section.

4.3. Calculation of TESPEL ablation

In order to estimate appropriate pellet dimensions and velocities for the injection, a simple calculation of the TESPEL ablation rate has been made. The method is similar to that of described in [22]. The ablation rate is determined as

$$\dot{N} = Q\frac{\eta}{\varepsilon}, \tag{4.1}$$

where ε is the sublimation energy for a given material, η is the attenuation factor of the electron heat flu Q, which is calculated as [32]:

$$Q = 2\sqrt{2\pi}\, n_e T_e^{3/2} r_p^2 m_e^{-1/2} \tag{4.2}$$

Here n_e and T_e are electron density and temperature, r_p is radius of the ablating surface and m_e is electron mass.

On the other hand, the ablation rate equals to the rate of decreasing of the amount of particles in the pellet:

$$\dot{N} = 4 n_s \pi r_p^2 \dot{r}_p, \tag{4.3}$$

where n_s is the molecular number density of the pellet material, $\dot{r}_p$ is the rate of decreasing of the pellet radius.

Combining this equation with (4.1) and (4.2) one can easily obtain an expression for $\dot{r}_p$:

$$\dot{r}_p = \frac{1}{\sqrt{2\pi}} n_e T_e^{3/2} m_e^{-1/2} \frac{\eta}{\varepsilon n_s} \tag{4.4}$$

The pellet penetration into a plasma, i.e. the length of the pellet flight until $\dot{r}_p = 0$, is calculated by integrating the expression (4.4).

It is worth to mention, that for the described simple method of calculating of the pellet penetration, the rate of decreasing of the pellet radius $\dot{r}_p$ does not depend on the pellet radius r_p. This means, that the time of ablation of a shell (and its penetration into plasma) depends on the shell thickness, but not on its radius. Thus, the penetration of TESPEL into plasma can be adjusted by the shell thickness, whereas the total amount of the deposited electrons (i.e. the perturbation of the background plasma) can be reduced by using the shells of smaller diameter.

An example of the calculation of Eq. (4.4) is shown in Fig. 34. The minor radius in the direction of the pellet flight is 28 cm. The density and temperature profiles of the target plasma are both assumed as parabolic. Central and edge electron temperatures are 500 eV and 20 eV, respectively, while central and edge density are 2×10^{13} cm^{-3} and 10^{12} cm^{-3}. The attenuation factor is assumed as $\eta_{LiH} = 0.8$ for lithium hydride and $\eta_{PS} = 0.4$ for polystyrene. The sublimation energy for lithium hydride is

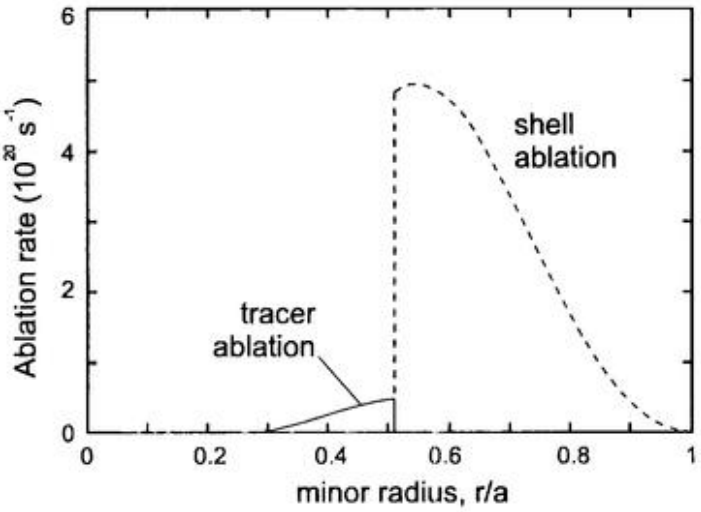

Fig. 34. Ablation rate of TESPEL in CHS plasma. Pellet velocity: 400 m/s, shell diameter: 350 μm, wall thickness: 50 μm, tracer diameter: 50 μm.

$\varepsilon_{LiH} = 2.4$ eV [49] and for polystyrene it is taken as $\varepsilon_{PS} = 3$ eV (see explanations below). In this case the ablation of the tracer starts at $r/a = 0.51$ (further – deposition location) and continues until $r/a = 0.26$ resulting in deposition width of 6.9 cm. However, because of the decaying ablation rate in the end, the main part of the tracer particles is deposited within a smaller distance of the flight path. Namely, 80% of the tracer material is ablated in 3.3 cm and 90% in 4.1 cm. For this reason, further we will refer to the deposition width as a length of the pellet flight path within which 90% of the tracer particles are deposited.

In the example above we used approximate values for the attenuation factor η and the sublimation energy ε_{PS} for polystyrene. Correct value for the latter is obscured by the complexity of the sublimation process of polystyrene as an organic polymer and the resulting sophisticated mechanism of the screening of incoming heat flux. Uncertainty in the η values arises from the variety of theoretical methods describing the ablation process. Here we do not strive to obtain exact theoretical values for η and ε_{PS}, but confine them within the following possible ranges: $\varepsilon_{PS} = 2\pm1$ eV, $\varepsilon_{LiH} = 2.4\pm0.2$ eV and $\eta = 0.5\pm0.3$ for both polystyrene and lithium hydride. Variation of these values for polystyrene affects mainly the deposition location and those for lithium hydride will alter the deposition width. From the viewpoint of the particle transport measurement, a small value of the deposition width is more important than the location of the deposited tracer particles. Thus, we can expect that uncertainty in the values of the ε_{PS} and η_{PS} for polystyrene will be resolved by experimental data on the injection into plasma. Fig. 35 presents a dependence of the deposition location

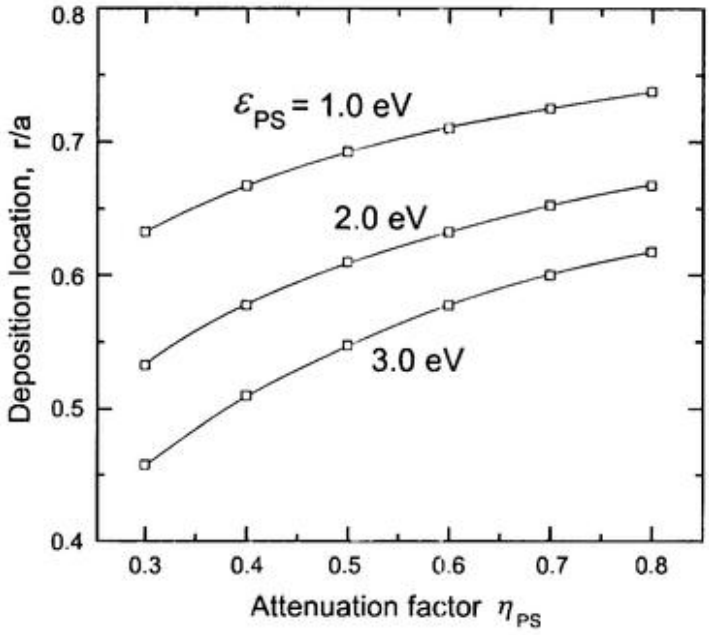

Fig. 35.Tracer deposition location calculated for various values of η_{PS} and ε_{PS}. Plasma and pellet parameters are the same as in Fig. 34.

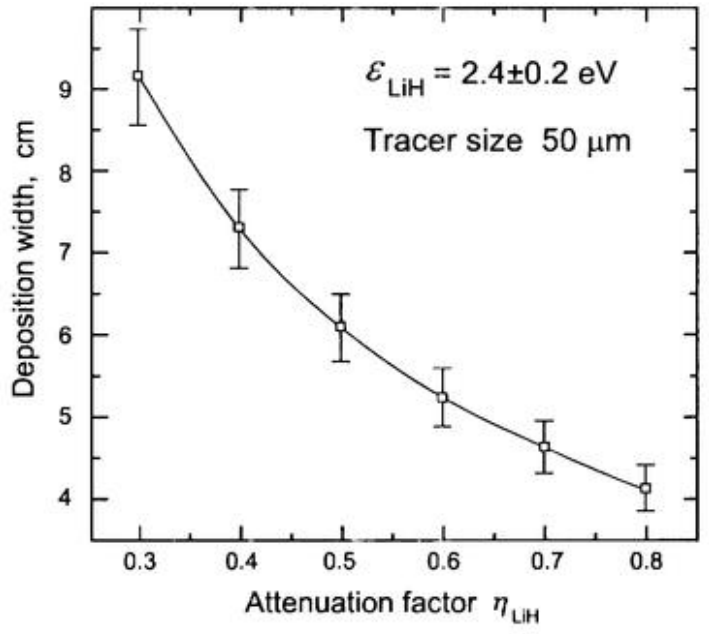

Fig. 36. Tracer deposition width calculated for various values of η_{LiH}. The error bars correspond to the error in the value of ε_{LiH} = 2.4±0.2 eV. Plasma and pellet parameters are the same as in Fig. 34.

on the attenuation factor for polystyrene η_{PS} for various values of the ε_{PS}. Result of the similar variation of η_{LiH} and ε_{LiH} is shown in Fig. 36 as a dependence of the deposition width on the attenuation factor for lithium hydride.

It is seen from Fig. 36 that the minimal value of the deposition width is estimated as 4.1 cm. However it can be further lowered by reducing the size of the tracer inserted into the shell. At the same time too small amount of the tracer ions will require a high sensitivity of a detecting diagnostics. Therefore, here we propose to fill the polystyrene shell with numerous macro particles of the tracer material each having the size smaller than 10 μm. In ideal situation the polystyrene shell should be filled with a fine powder of lithium hydride with typical particle size as small as possible. In this case the whole tracer contents will be ablated approximately during the ablation time of the largest piece, thus providing better localization of the deposited tracer ions. The total mass of the tracer can be even larger than that of a single crystal of 50 μm size for the purpose of producing higher signal for a detecting system. Fig. 37 presents calculated deposition width for a 10 μm lithium hydride sphere at the same plasma conditions and pellet velocity as in Fig. 34. It is seen that the expected tracer deposition width can be as small as 1 cm. This confirms that the injection of a TESPEL with fractionated tracer contents can deposit the tracer with good localization.

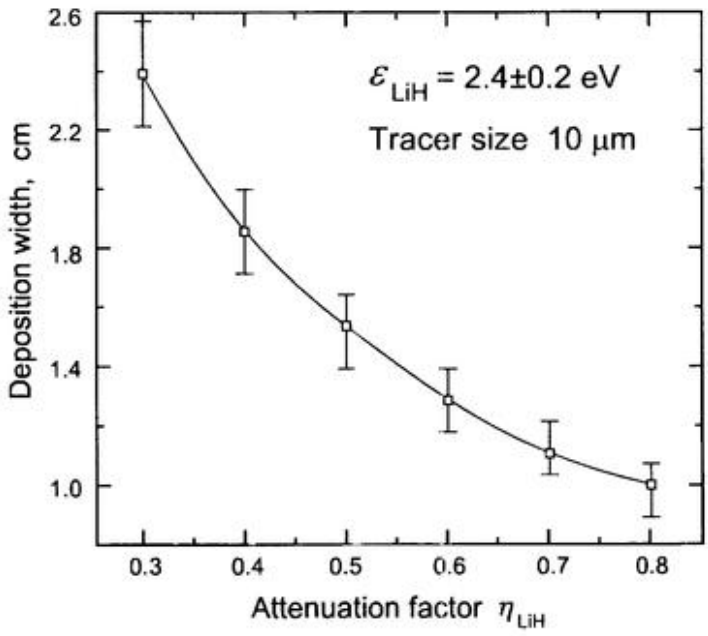

Fig. 37. Deposition width of the 10 μm tracer calculated for various values of η_{LiH}. The error bars correspond to the error in the value of ε_{LiH} = 2.4±0.2 eV. Plasma parameters are the same as in Fig. 34.

In the calculations above a standard model based on the one-dimensional spherical ablation was employed. However, it may be necessary to mention a possible nonuniformity of the ablation, which can appear due to the difference of the heat flu in the directions of parallel and perpendicular to the magnetic field lines. One example is the model of ablation in "lentil" form developed by Miroshnikov [43]. The penetration depth based on the lentil model differs only by about 20% from that of the standard model. The instability of the ablation causing striations [44] can also affect the feature of the pellet ablation. But this does not change significantly the penetration depth of the pellet and does not alter the major effect of the present process. So, the nonuniformity of the ablation is considered to give only a small effect on the resulting location of the tracer deposition. On the other hand, the experimentally observed behavior of the tracer may even clarify the ablation mechanism due to the property of the local deposition.

4.4. TESPEL production and acceleration

4.4.1. TESPEL production routine

The procedure of manufacturing of a TESPEL consisting of lithium hydride encapsulated into a polystyrene shell consists of the following basic steps:

1) Selecting the shells of the appropriate size;
2) Making holes in the selected shells;
3) Inserting the tracer material into the shells;
4) Closing the holes.

The density-matched emulsion method [45] of polystyrene shell production allows obtaining the shells with diameter smaller than that of described in [46]. However the latter provides better uniformity of the shell sizes: for the average diameter of 350 μm about 80% of the shells have diameter within the range of 300–400 μm. For the selection of shells with appropriate diameter, a standard optical microscope with ~10 μm resolution is used. For the precise measurements we use an interferometric microscope which provides 1 μm accuracy for the shell diameter and 0.1 μm for the wall thickness.

Every selected shell is glued on a sample glass by means of acrylic resin glue which dries up under UV light. After the TESPEL is completed it can be easily separated from the solid glue while the latter remains on the glass. The glue is required to fasten the shell for the following operations.

On the next stage it is necessary to make holes for inserting the tracer. This can be done by means of a boring machine equipped with a microdrill. For our purpose we used the microdrill of 50 μm diameter, which produces holes of 70–90 μm. The result of this operation is shown in Fig. 38.

The next step is inserting the tracer material into the shells. The lithium hydride used for this purpose is in the form of a fine powder with maximal size of the crystals of about 150 μm (See Fig. 33). Lithium hydride slowly reacts with water vapor from the air and turns into lithium hydroxide. For the standard room conditions such a powder becomes oxidized during about 3 hours, and therefore it should be refreshed rather frequently.

From this powder one should pick up solid crystals of 40–60 μm size and insert them into the holes. This can be done by means of a thin glass pipe, which can be made from a standard ∅1 mm glass pipe by simultaneous heating and stretching. The end diameter of the stretched pipe should be small enough to fit into the hole of the shell. The other (thick) end of the pipe can be connected to an air evacuating system, which can easily be turned on and off. Such an instrument is very useful for picking up and releasing small particles of 0.05–1 mm.

On the final step the holes in the shells are covered with polystyrene dissolved in toluene. A small drop of the solution should be put on the top of each shell. The drop covers the hole completely due to the surface tension. The amount of liquid should not be too large, otherwise the whole shell can be melted and destroyed due to the high absorption of toluene by polystyrene. The main difficulty here is a high volatility of toluene resulting in a quick solidification of the solution. The surface of such a small drop becomes solid within a second, which makes difficult the moistening of the shell surface. For this reason the percentage of the polystyrene in the solution should be rather small (8–10%). A photo of the shell with closed hole is shown in Fig. 39.

After all shells are completed, it is necessary to place them in a vacuum or noble gas atmosphere, because the polystyrene slowly passes the air through the shell wall.

4.4.2. Stand testing of shell acceleration

As a first step, experiments with injection of the ready-made empty plastic shells have been made on the laboratory stand. These experiments were made in order to:

1) prove the principle possibility of the acceleration of such thin shell pellets without being destroyed;
2) determine optimal operating parameters of the injection (propellant gas pressure, camera aperture setting and others).

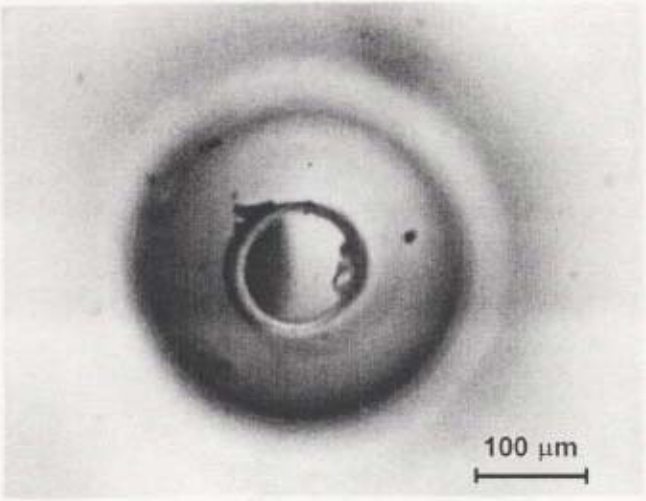

Fig. 38. Photo of a polystyrene shell with hole. The focal plane of the microscope is adjusted to the top of the shell.

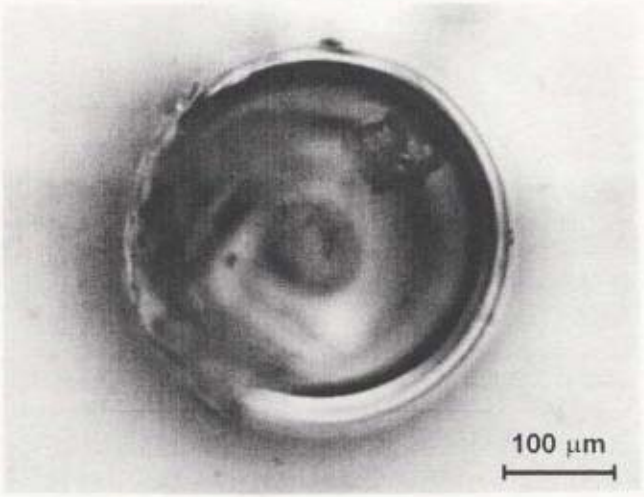

Fig. 39. Photo of a completed TESPEL. The focal plane of the microscope is adjusted to the half height of the shell. In the upper right part of the shell a lithium hydride crystal is seen.

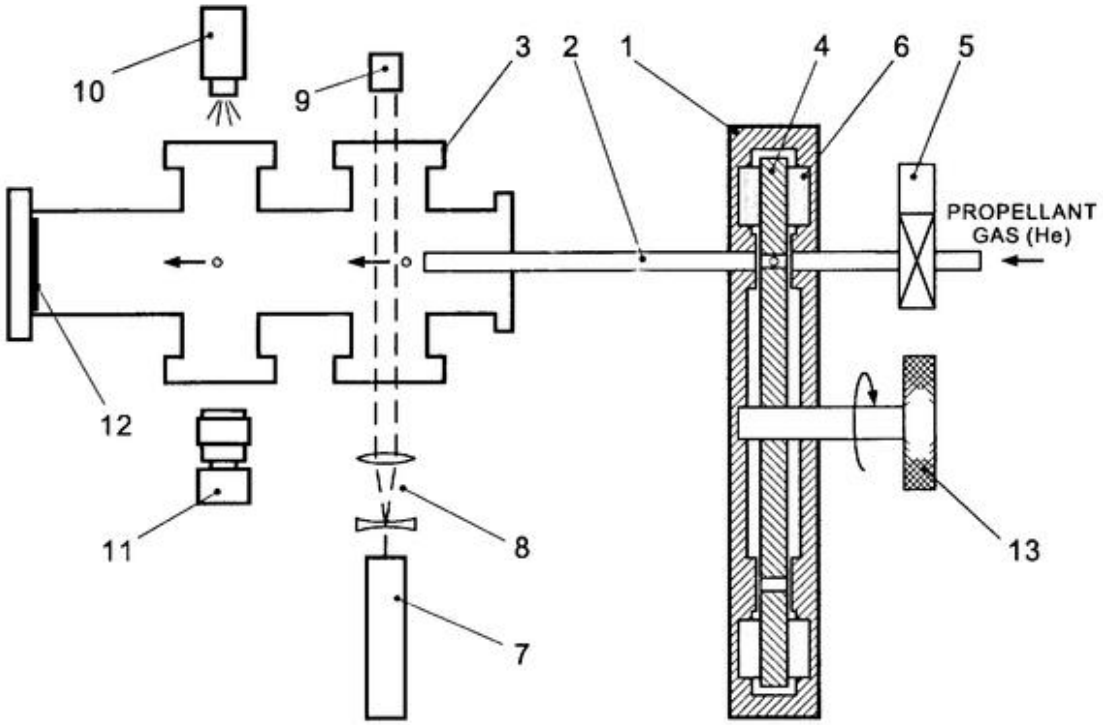

Fig. 40. Schematic view of the TESPEL injector.

The schematic view of the pellet injector is shown in Fig. 40. Its construction is similar to the one shown in Fig. 4, however, the design of the magazine with pellets has been substantially improved (as described below), in order to handle the small and fragile polystyrene shells. The main parts of the injector are the magazine *1* for pellets, gun barrel *2* and observation chamber *3*. Prior to the injection a set of 29 pellets is loaded into holes of the rotative disk *4* of the magazine. After the pulse of the propellant gas from the shooting valve *5* with duration of 2–4 ms, the pellet located at the shooting axis is accelerated and goes through the gun barrel *2*. The length of the barrel is 1.2 m. The inner diameter of the barrel and the holes in the disk are 1.0 mm. The clearance between the disk and the housing of the magazine is kept small enough by means of precise rollers *6* so that the pellet size can be as low as 0.25 mm. The accuracy of positioning of a hole with a pellet at the injection axis is not worse than 0.01 mm.

Then the pellet crosses the beam of He-Ne laser *7* expanded by the beam expander *8*. The light from the beam expander goes to the light detector *9* and then transferred by the optical fiber to the photo-multiplier. The photo-multiplier's signal is changed by the pellet shadow and this change is recorded by a digital oscilloscope, which is triggered at the moment when the pellet crosses the laser beam. The light detector *9* has two input slits at the distance of 5.5 mm and this allows to obtain a

rough estimation of the pellet velocity. The trigger signal from the oscilloscope runs the fast flash lamp *10* (pulse duration is about 180 ns) and the instant image of the flying pellet is projected on the digital CCD camera *11*. The CCD matrix has 1134×972 pixels with 8 bit A/D conversion. Finally, the pellet comes to the aluminum foil *12* which is used for a direct detection of the pellet. After each shot the disk in the magazine is manually rotated by the handle *13* in order to position the next pellet.

4.4.3. Obtained results and discussion

The main purpose of the laboratory tests with the plastic pellet injection was to achieve a high probability of the injection. Among the reasons that made the injection unstable it is necessary to mention:

1) High fragility of the pellets which sometimes resulted in destroying the pellet during the acceleration.
2) Small size and transparency of the pellets resulting in a small signal from the pellet shadow and thereby reducing the signal to noise ratio of the photo-multiplier.
3) The transparency of the shells also complicated the photography by the CCD camera requiring fine adjustment of the aperture for obtaining an appropriate pellet image.

In spite of these factors the acceleration of the plastic pellets has been successfully performed. For the first series of experiments we used empty shells with diameter 400–500 μm and wall thickness 10–20 μm. An example of the photographed polystyrene shells is shown in Fig. 41 a). The typical pellet velocity was in the range of 350–450 m/s. The acceleration was made by the helium gas with 10 bar pressure. In order to study the destroying effect of propellant gas pulse, its pressure was increased to 14 bar. However, no pellets were registered by the light detector at this condition, and in the aluminum foil target numerous tiny bumps were observed. This fact confirms that a plastic pellet can be easily destroyed by the strong pulse of propellant gas. Even at the level of 10 bar about 25% pellets were destroyed. Sample photo of a destroyed shell is presented in Fig. 41 b).

The next series of experiments was made with TESPELs manufactured by the method described in section 4.4.1. The diameter of the pellets was 300–400 μm and wall thickness of 40–50 μm. In this case the pellet hardness was significantly higher resulting in more stable injection. No broken pellets were registered for the propellant gas pressure up to 25 bar. However the signal of the light detector was even smaller (typical S/N ratio was 2–3) that made the pellet registration more difficult. The smaller size of the pellets also resulted in worse acceleration: the pellet velocity ranged in 250–350 m/s for the propellant gas pressure of 15 bar. The variation in the pellet velocity can be explained by the variation in pellet diameters. Increase of the

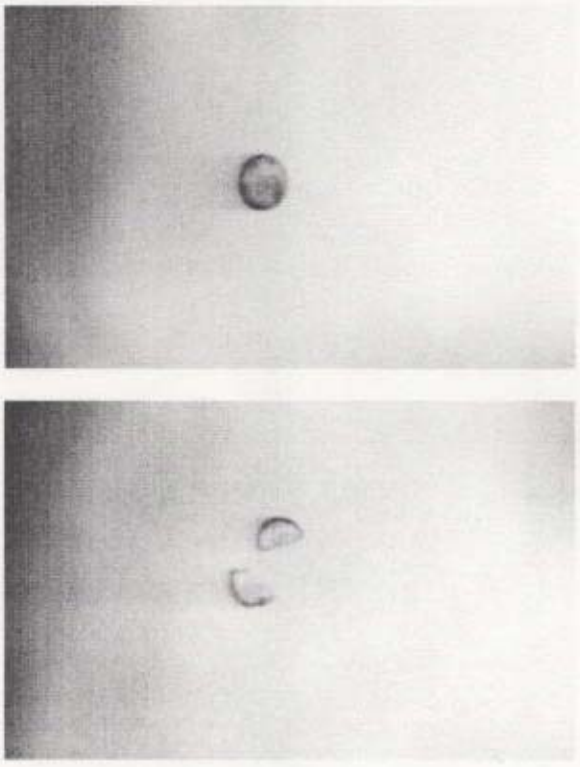

Fig. 41. CCD images of polystyrene shells in flight (the shells are moving from right to left). Wall thickness is 10–20 μm.
a) Safely accelerated shell;
b) Sample photo of a destroyed shell.

propellant gas pressure had a weak effect on the pellet velocity, which was not higher than 400 m/s even at 25 bar level. The further increase of the propellant gas pressure was not desirable because of a good vacuum requirement in the diagnostics chamber. At the same time, according to the calculation described in section 4.3, the achieved level of pellet velocities is enough for the plasma of a medium size machine.

4.5. Summary

As an alternative to the tracer-encapsulated cryogenic pellet, a method of injecting of the tracer-encapsulated solid pellet (TESPEL) has been developed. Because of the smaller size of the tracer core of the TESPEL, the new method can be

applied for the transport measurements in a plasma of a medium size machine, such as CHS. Various materials and configurations of the TESPEL have been tested:

1) Hydrogen pellet with smaller core (about 100 μm diameter);
2) Hydrogen pellet with a core in the form of empty polystyrene shell;
3) The core in the form of a small lithium sphere (<100 μm diameter);
4) Coating of a small core by a polystyrene layer;
5) Inserting a core into a polystyrene shell.

From these, the most appropriate configuration of TESPEL has been selected, which consists of a tracer core made of lithium hydride crystal of 50 μm size encapsulated into a spherical shell made of polystyrene. Such a configuration of the TESPEL has been successfully realized by means of a specially developed manufacturing procedure. The improved construction of the pellet injector has allowed to accelerate the produced TESPELs safely, and the photography of TESPEL in flight has confirmed the pellet integrity. For the pellets with diameter 300–400 μm and wall thickness 40-50 μm the fragility of polystyrene shells becomes insignificant. Calculation of the TESPEL ablation rate has demonstrated that the obtained TESPEL dimensions and achieved pellet velocities are appropriate for the injection into a medium size plasma. It was proposed to fractionate the tracer contents in order to provide better localization of the deposited tracer ions in the plasma. The data obtained in these experiments have proved that injection of the TESPEL made from the plastic shells can be an effective tool for the particle transport diagnostics.

5. TESPEL INJECTION EXPERIMENTS

5.1. Introduction

A local particle transport in plasmas can be analyzed directly by observing evolution of a small perturbation artificially made at a certain point in the plasma core. Such a perturbation can be a tracer particle source which is poloidally and toroidally localized within a limited plasma volume of the order of 1 cm^3. Injection of a tracer-encapsulated pellet having a small core of tracer particles is a prospective method for providing this localization.

After the success of the proof-of-principle experiments with tracer-encapsulated cryogenic pellet (TECPEL) described in Chapter 3, it was proposed to use a tracer-encapsulated solid pellet (TESPEL), which consists of a core as a tracer made of lithium hydride encapsulated into a polystyrene shell. The method of TESPEL production and the experimental results of TESPEL acceleration are discussed in Chapter 4. In this chapter, the first experimental implementation of the complete diagnostics system based on TESPEL injection is described.

As TESPEL can be handled at room temperature, the pellet injector does not need a complicated cryogenic system and therefore, can be much simpler and more compact. The dimensions of TESPEL itself are also smaller than those of TECPEL, that makes the injection more appropriate for the plasma of a medium size experimental device, such as the Compact Helical System (CHS) [47].

The motion of the lithium ions deposited by TESPEL can be observed by a method of charge exchange recombination spectroscopy (CXRS). The charge exchange reaction takes place between the fully ionized Li ions and the neutral hydrogen atoms from the neutral beam injection (NBI). Thus, for proving the essential concept of the new diagnostic method, TESPEL is injected into the NB plasma of CHS.

5.2. CHS plasma configuration

Magnetic configuration of the CHS device is similar to that of the Heliotron E. CHS is a heliotron/torsatron device with multipolarity $l = 2$, toroidal period number $m = 8$ and a rather low aspect ratio. The major radius of the vacuum chamber is 100 cm and the poloidal cross-section of the plasma is elliptical with the averaged minor radius of 20 cm. The toroidal magnetic field can be varied from 0.7 to 2 T. The vacuum vessel wall is conditioned by titanium gettering. The schematic of the CHS diagnostics arrangement is shown in Fig. 42.

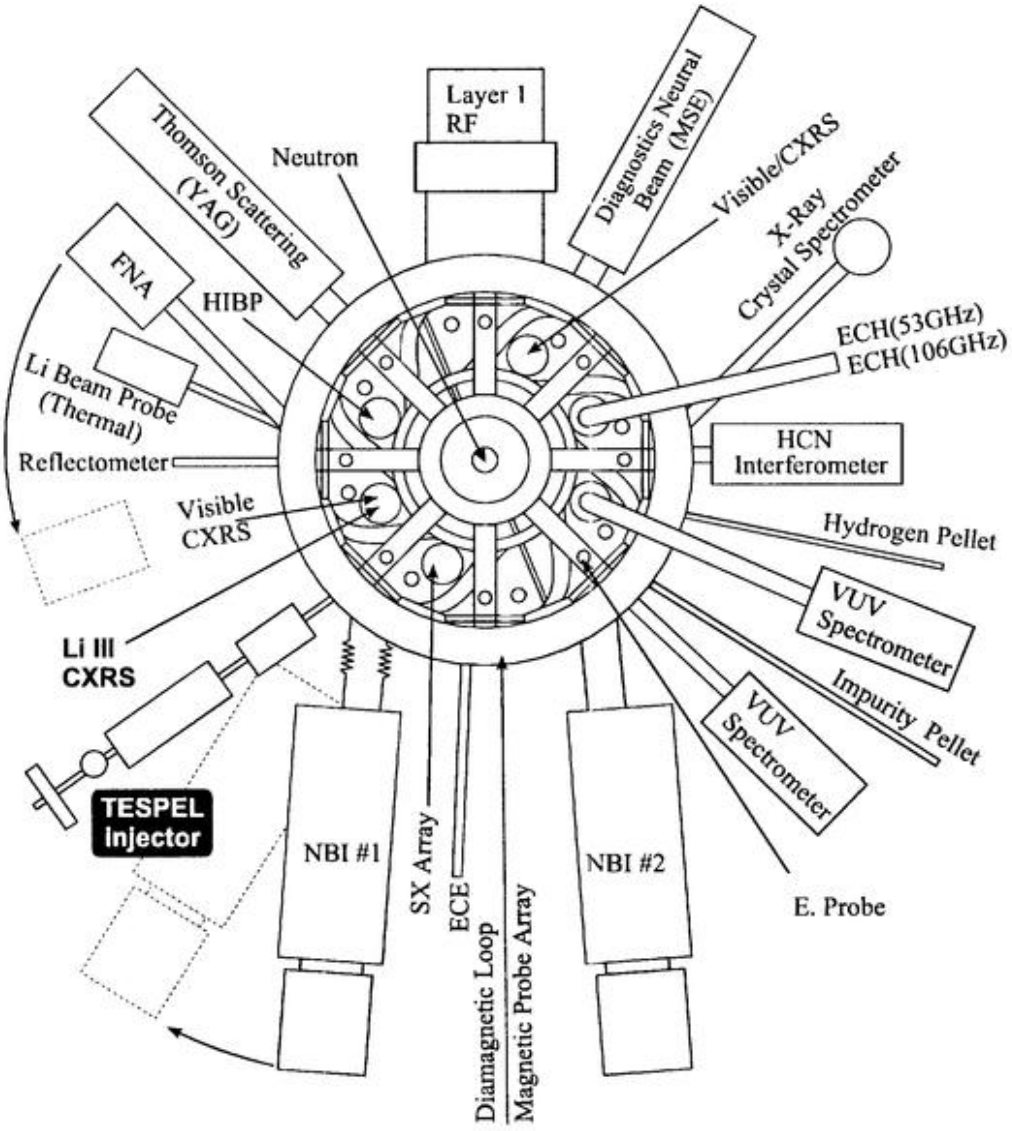

Fig. 42. CHS diagnostics arrangement.

The target plasma of the CHS is produced by the electron cyclotron heating (ECH) at the frequency of 53 GHz (corresponding to the second harmonic resonance) with the maximal output power of 400 kW. The ion cyclotron resonance heating (ICRH) at the frequency of 7.5 MHz can also be used for the plasma production. As the main source of the plasma heating, two neutral beam injectors (NBI #1 and #2) are employed with the maximal energy of 40 keV and 36 keV, respectively [50]. The typical output power of the two NBI lines is 1.1 MW and 0.7 MW, respectively.

The injection of TESPEL was performed at the standard operation mode of CHS with the radius of magnetic axis R_{ax} = 99.5 cm or 97.4 cm. The magnetic field strength for these configurations is set to be 0.9 and 1.3 T, respectively. In order to study the effect of the magnetic field strength, the TESPEL was also injected during the CHS operation with the magnetic field of 1.9 T and R_{ax} = 94.9 or 92.1 cm. The typical central electron temperature and density are 0.3–0.8 keV and 1.5–4.0×10^{19} m^{-3}, respectively. The ion temperature during the high-T_i mode of the CHS operation can be as high as 1.0 keV in the center, due to the NBI heating of ECH.

5.3. Experimental setup of TESPEL injector

The TESPEL injector with the differential pumping system has been installed on CHS at the port, to which the NBI #1 line is connected (See Fig. 42). Construction of the TESPEL injector is described in Section 4.4.2. The injector is connected to the differential pumping system (DPS), which is similar to the one used on Heliotron E (See Section 2.2), but because of the space limitations, the DPS was reduced to three main chambers isolated by gate-valves. The chamber nearest to the injector is evacuated by a rotary pump only, while the two others are evacuated by turbo-molecular pumps (TMP) coupled with rotary pumps. At the end of the gun barrel, the first chamber is connected to a buffer tank for absorbing the pressure jump of the propellant gas following the pellet. Because of the high vacuum requirements, the chamber nearest to the CHS is evacuated by two TMPs concurrently. They are connected to the different parts of the one chamber separated by a diaphragm. The one TMP has a magnetic suspension of the axis, and because of the strong magnetic field of the CHS, it is located about 4 m away from the evacuated chamber. The shooting valve of the injector is triggered remotely by a TTL pulse, which is delayed by 50-70 ms from the main CHS timer. The gate-valves of the differential pumping system are triggered by the same pulse, so as to isolate the chambers soon after the shot. (The time response of the first gate-valve is 0.05 ms, while the pellet reaches it at 4–6 ms

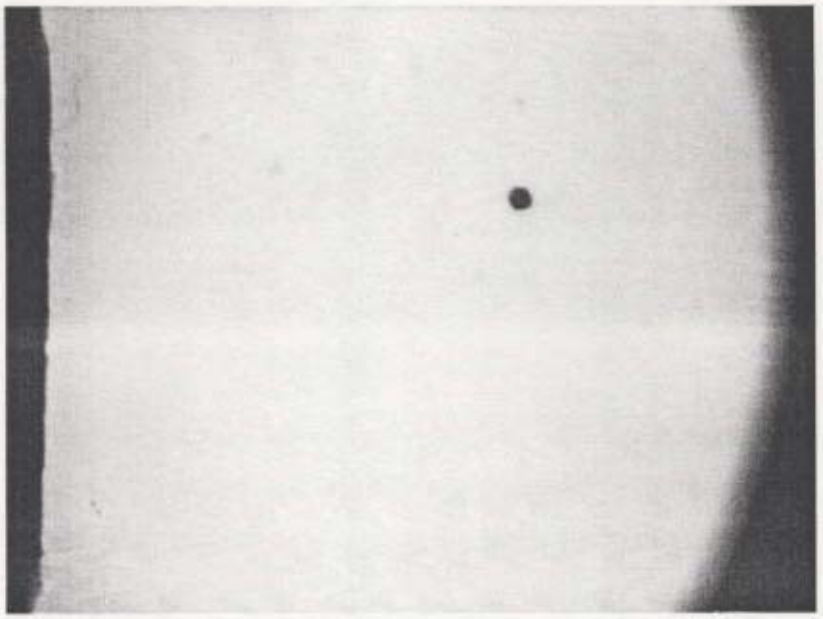

Fig. 43. Photo of a TESPEL in flight before it enters the plasma. The edge of the last guide-tube with the outer diameter of 8.4 mm is seen on the left. The TESPEL diameter is 350 μm.

after the shot.) During the shot of the propellant helium gas with pressure of up to 25 bar and duration 2–4 ms, the vacuum level in the first chamber reaches 10 torr for about 10 s, while in the last chamber it does not exceed 10^{-6} torr. In the idle state, the vacuum level in the last chamber is $1.3–1.6\times10^{-7}$ torr. Thus, the construction of the differential pumping system has allowed to maintain the necessary vacuum level.

The He-Ne laser light barrier has been located at the end of the last guide-tube in order to estimate the pellet velocity. The accurate measurements are made by the time difference of the light detector signal and the plasma response to the injected pellet. The typical pellet velocity is in the range of 250–350 m/s. The signal of the light detector triggers the fast flash lamp and the pellet is photographed by a CCD camera. Such a system was installed so as to confirm the TESPEL integrity after the pellet passed all the guide-tubes. An example of the TESPEL photo is shown in Fig. 43.

The capacity of the injector magazine is 29 pellets. Thus, in one series of experiments, 29 pellets can be injected one by one. Due to the simple configuration, if necessary, the injector magazine can be dismounted from the injector without turning off the pumping system and reloaded with new pellets in less than one hour.

5.4. Setup of observing diagnostics

Layout of the TESPEL injection experiment and the observing diagnostics are shown in Fig. 44. The figure includes the arrangement of the pellet injection line, the neutral beam injector (NBI) line, location of CXRS array for observation of LiIII in the radial direction, and other diagnostics for observing the pellet cloud.

The light emission from the pellet is collected with an optical system that includes a rotative mirror and two half mirrors. The optical system allows to observe the pellet from the back when it enters the plasma. The rotative mirror is installed in a supplementary vacuum chamber which is mounted on the CHS port. The mirror is made of polished stainless steel and can be rotated and faced off the plasma, so as to prevent it from contaminating during the titanium gettering of the CHS chamber. The half mirrors divide the light between two compact CCD cameras and an input of the optical fiber. Each CCD camera is equipped with an optical filter for H_α and Li I (or Li II) lines. The optical fiber goes to the control room to another optical system, where the light is further divided between two photo-multipliers with similar configuration of filters.

With this system it is possible to register the space integrated light from the ablating pellet in two wavelengths simultaneously with high time resolution (The maximal resolution of ADC is 1 μs). At the same time, it is also possible to obtain the time integrated images of the pellet cloud emission in different spectral lines. The photography of the pellet cloud has been carried out with the purpose of obtaining the pellet location during the ablation of the core, which is necessary to confirm the correct deposition of the tracer material and its localization.

In order to achieve higher spatial resolution along the pellet flight path, the pellet is also photographed by a CCD camera installed at the neighboring port. This location is indicated as CCD3 in Fig. 44. In fact, up to three CCD cameras can be mounted at that location, one under another, and equipped with H_α, Li I, and Li II filters.

The long time scale diffusion in radial direction of the fully ionized lithium ions is measured by observing the Li III emission of Li^{2+} ions, which appear from the charge exchange recombination of Li^{3+} ions:

$$Li^{3+} + H^0 \rightarrow Li^{2+} + H^+ + h\nu\,(\text{Li III}) \qquad (5.1)$$

The source of hydrogen atoms for this reaction is the neutral beam for plasma heating. Li^{2+} ions can also exist in the peripheral plasma with low electron temperature due to recombination of Li^{3+} ions. For this reason, the Li III light is

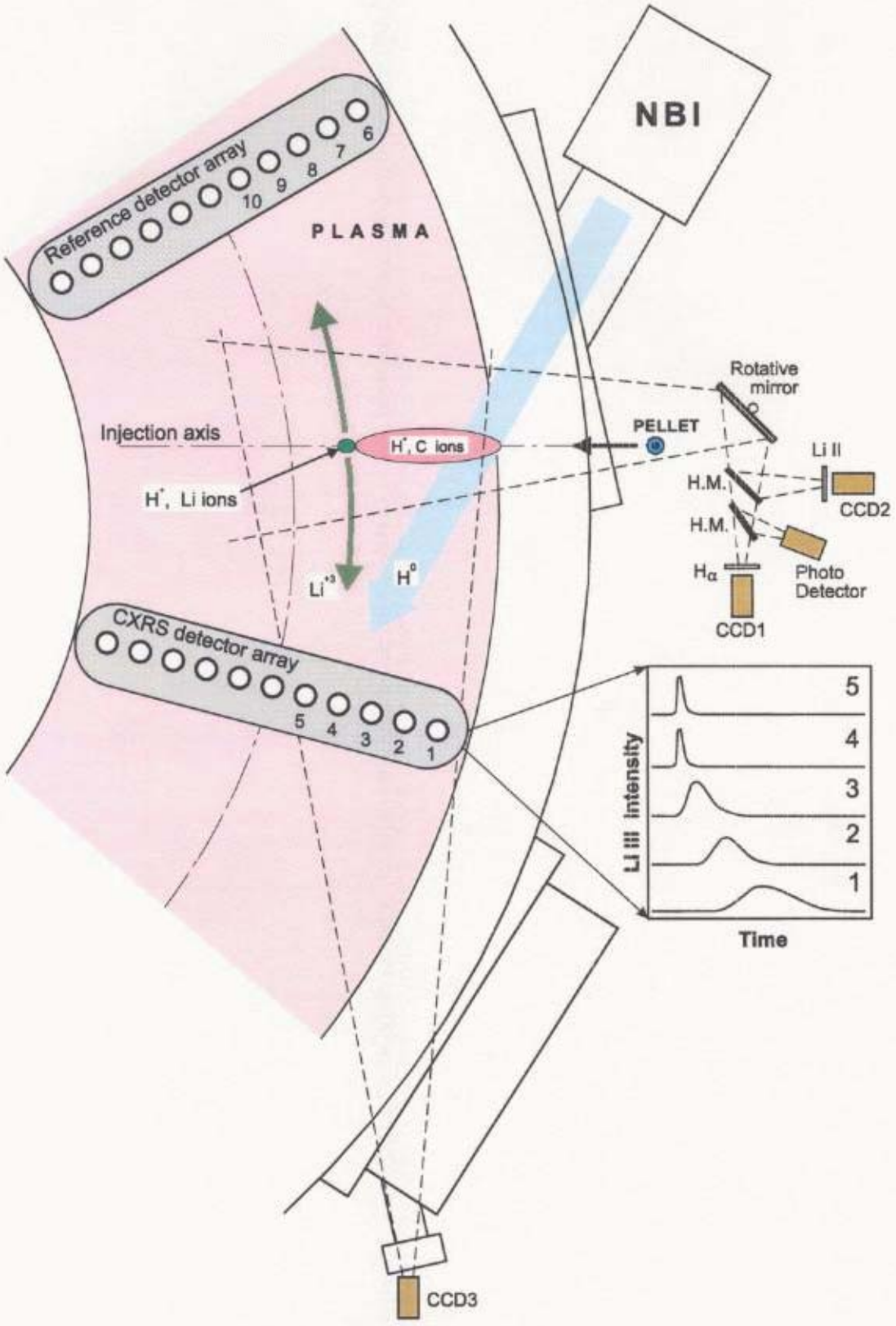

Fig. 44. General layout of the TESPEL injection experiment on CHS.

observed simultaneously at the location on the NBI path and, for reference, at the neighboring port without the NBI (as shown in Fig. 44). Thus, the difference of these signals can be interpreted as a pure emission from Li $^{2+}$ ions originated from the charge exchange with NBI. Because of the rather small thickness of the neutral beam in the vertical direction (less than 10 cm in case of CHS), the reaction takes place in the vicinity of the equatorial plane. Therefore, the L III light collected along a vertical observation chord is directly proportional to the local density of Li^{3+} ions at the corresponding radius. Thus, the CXRS system consists of the two arrays of the photo detectors having different radial positions. The minimal distance between two neighboring detectors is 16 mm. Each detector consists of a lens coupled with an optical fiber that goes to a photo-multiplier. The lens collects almost parallel light (divergence about 1.6° in full angle) with viewable area of about 14 mm in diameter at the equatorial plane. In contrast to conventional CXRS systems that use CCD [51, 52], here photo-multipliers are employed to achieve higher time resolution of 10 μs (limited only by the performance of the data acquisition system). In total, 5 observation lines are installed at the location of NBI and 5 corresponding lines at the reference location. The radial position of each line can be adjusted, if necessary, according to the location of the plasma axis. The photo-multipliers are equipped with optical filters for observation of the line $\lambda = 449.9$ nm corresponding to the transition from ^{2}G to ^{2}F in Li^{2+} ions.

5.5. Experimental results and discussion

By injection of a TESPEL into the plasma with the density level of 1.5×10^{13} cm^{-3}, the electron density increase of $\sim 5\times10^{18}$ cm^{-3} is observed, which is consistent with the particle number contained in the polystyrene shell (the contribution from the core is negligible). After the injection, the electron temperature decreases due to the sudden increase of the density, while the electron pressure $P_e = n_e T_e$ remains unchanged in the initial phase (See Fig. 45), which confirms that the process is adiabatic. The electron temperature is kept higher than the radiation barrier, and the temperature is recovered to the original level in the late phase. At that time ($t = 110$ ms in the Figure), the plasma density remains growing because of the continuing NBI injection, and the electron pressure becomes larger than the before-injection level. Thus, no harmful effect is caused to the plasma by TESPEL injection.

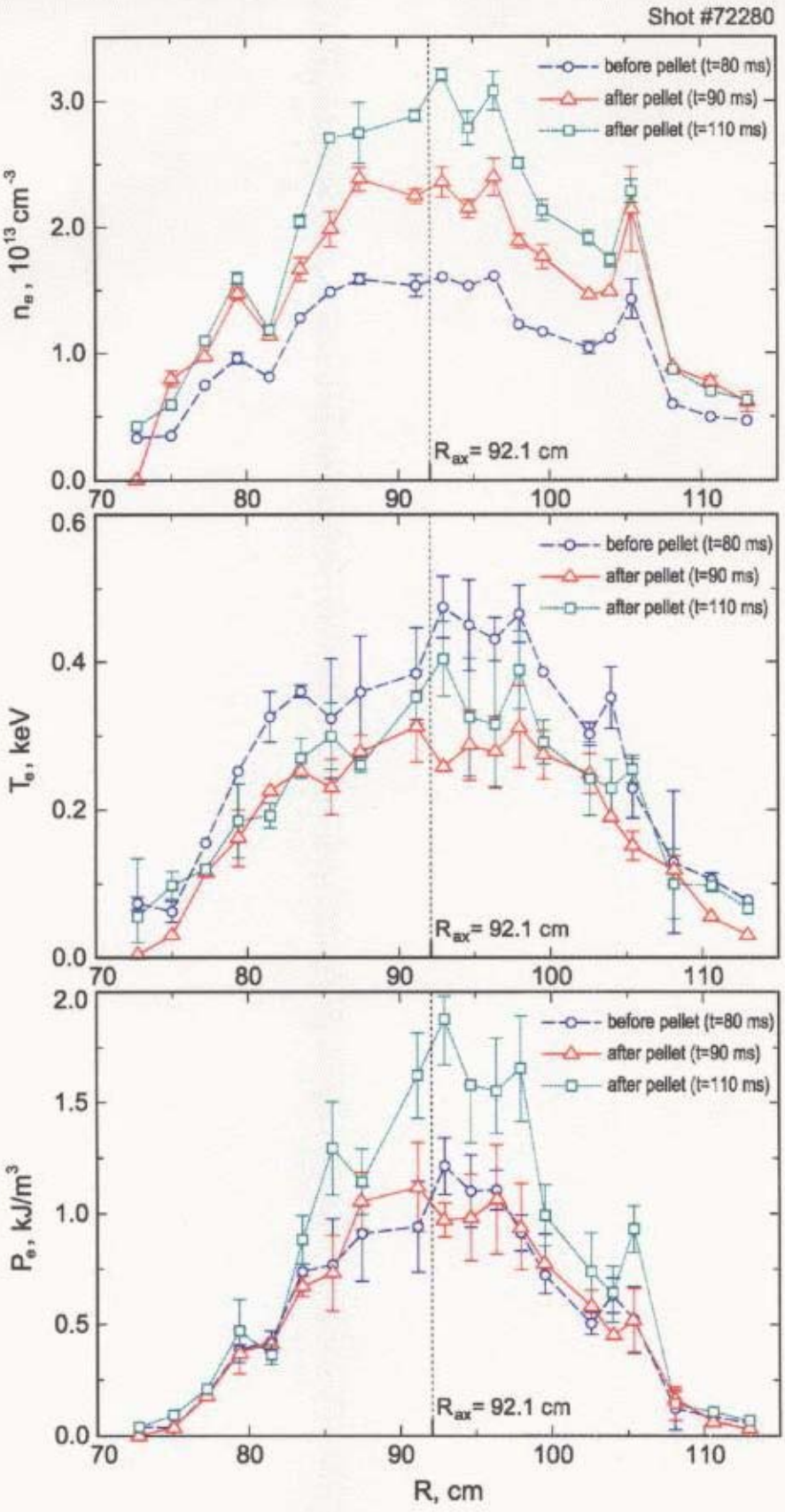

Fig. 45. Change of the electron temperature, density, and pressure profiles in a discharge with TESPEL injection (TESPEL was injected at t = 82.3 ms).

5.5.1. Observation of tracer deposition

The ablating pellet has been photographed from the two perpendicular directions simultaneously, which provided information about the exact location of the pellet in the plasma. An example of the obtained images is shown in Fig. 46. It includes the rear view of the pellet made with Li II filter and two side views of the same pellet for Li I and Li II light. The very beginning of the pellet ablation is obscured by construction elements. From these images, it is found that the pellet reaches the central region of the plasma. The Li I light starts at $R \approx 104$ cm and continues for about 3 cm, which proves the necessary location of the tracer deposition and its localization. The thickness of the pellet trace seen as Li I light is less than 5 mm, while the Li II light spreads for several centimeters out of the pellet path, which corresponds well to the typical life times of the Li^0 and Li^{1+}, respectively (See estimations in Section 2.6.2).

Besides the main region with intense Li II light located further in the plasma core, a thin pellet trace is also seen through the Li II filter along the whole pellet path. According to the TESPEL configuration, the Li II emission should start with the ablation of the TESPEL core, that is in the central plasma. This inconsistency is resolved by a similar image of a pellet without a core, shown in Fig. 47. Typically, one series of TESPELs contains 6–8 so-called reference pellets, which do not contain a core and are injected in order to distinguish the signal from the tracer by comparing to the background signal. So, the empty pellet has also produced the similar trace seen through the Li II filter. But the clear difference is seen between the two images: the real TESPEL produces a wide halo region in the end of ablation (between $R \approx 10$ and 100 cm), while there is no such thing with the empty pellet. The light seen through the Li II filter from the empty pellet is attributed to the emission on C VI line ($\lambda = 529.1$ nm) from carbon ions ablated by the shell. Because of the very strong ablation of the shell comparing to that of the core (See Fig. 34), the intense C VI light can be slightly passed by the Li II filter with $\lambda_0 = 548.7$ nm and a bandwidth (with 50% attenuation) of $\Delta\lambda = 1$ nm. Thus, for this shot, the region of real Li II emission is confined within about 5 cm along the minor radius.

More exact information about the deposition width of the tracer particles have been obtained from the signals of the photo-multipliers observing the ablating pellet through H_α and Li II filters with high time resolution. One example of the measured emission from the pellet cloud in H_α and Li II lines is shown in Fig. 48 a). It is seen that at first H_α appears for about 500 μs, and in the late phase Li II is emitted during a short period of about 100 μs. For comparison, signals from H_α and Li II detectors are shown in Fig. 48 b) in case of a reference pellet without a tracer. In this case, the peak in the late phase for Li II does not appear as expected (although some background

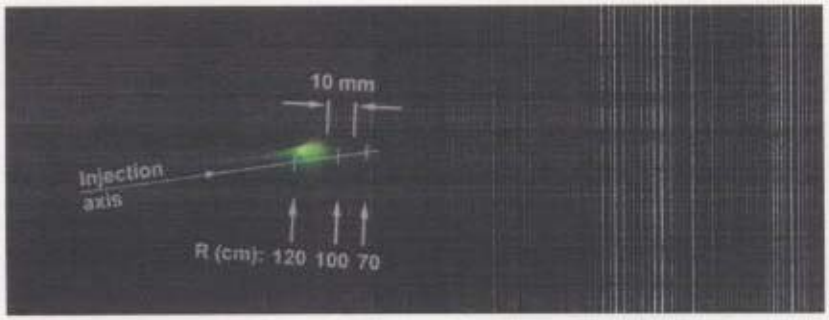

a)

b)

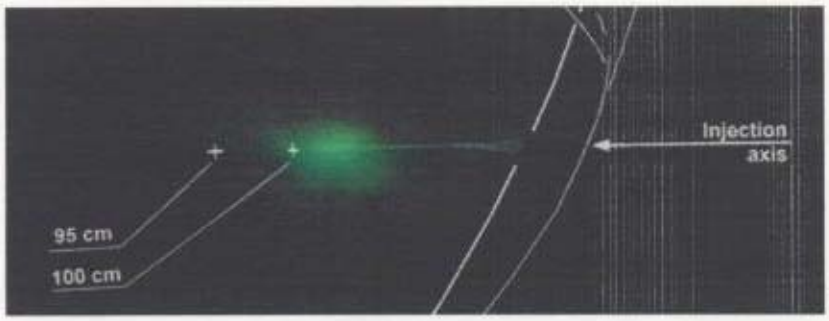

c)

Fig. 46. Three CCD images of the same ablating TESPEL (Shot #74989). Geometry is indicated as positions along major radius (R_{ax} = 94.9 cm): a) Li II filter, rear view of the pellet (from CCD2 of Fig. 44); b) Li I filter, side view from CCD3; c) Li II filter, side view.

Fig. 47. CCD image of a reference pellet without a core (Shot #74652, R_{ax} = 92.1 cm): Li II filter, side view from CCD3.

signal is still seen). These measurements indicate clearly the local deposition of the tracer particles in the core plasma region.

The top axes of the plots in Fig. 48 represent the pellet position along the minor radius as calculated from the known pellet velocity. These data provide direct information about the location of tracer deposition. There is a certain error in this

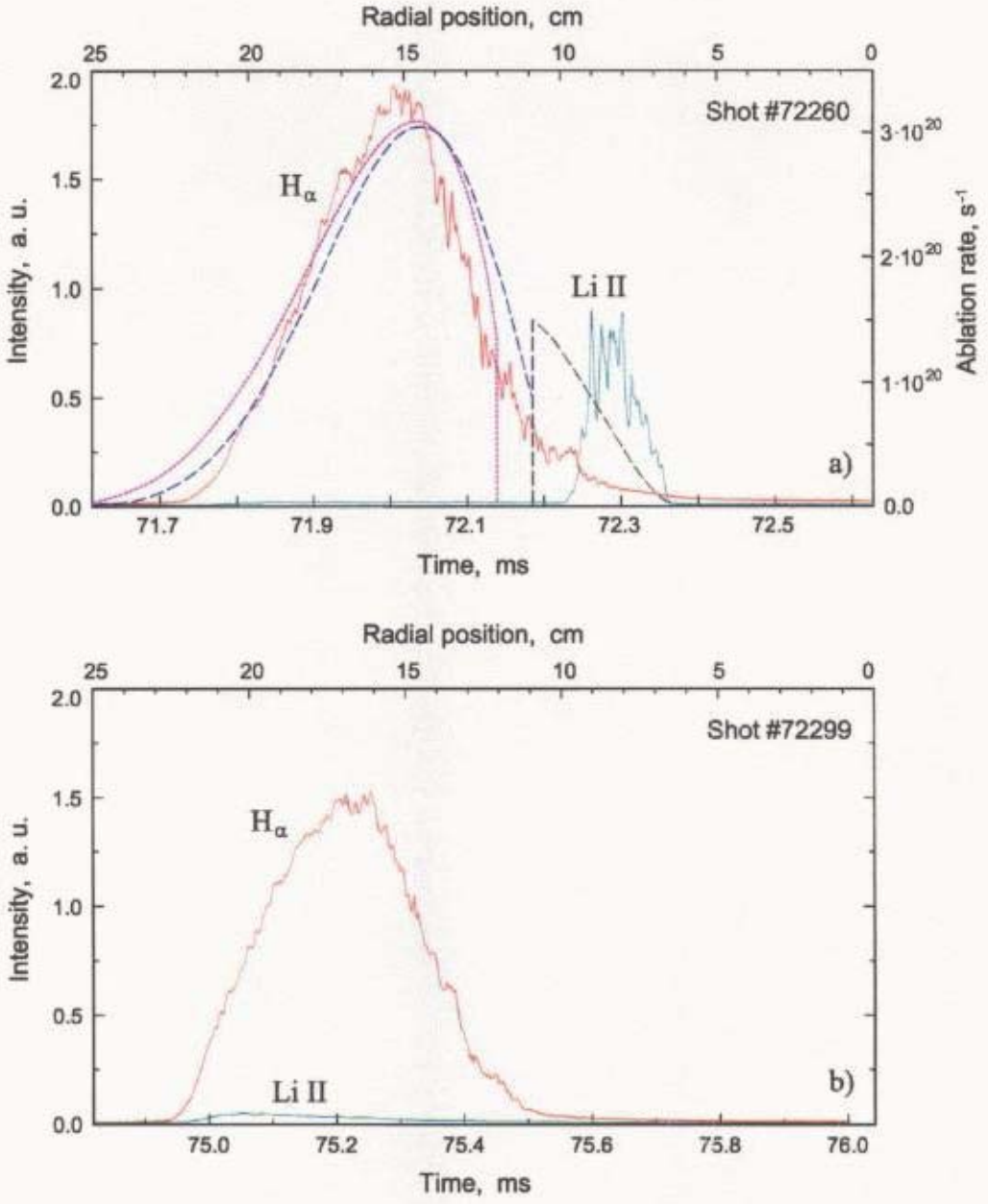

Fig. 48. Time dependencies of the pellet cloud emission in H_α and Li II lines (solid curves). Corresponding radial position of the ablating pellet is shown as the top axes. Ablation rates calculated by impurity model (dashed curves) and gas dynamics model (dotted curve) are also shown. a) Typical case with TESPEL injection; b) Emission from a reference pellet without a tracer core.

calculation due to an uncertainty in the location of the starting point of ablation, which is determined by ambiguous values of the peripheral temperature and density. (The deposition width of the tracer, however, can be obtained from these signals with high accuracy.) The obtained data of the deposition location were compared with the corresponding CCD images and a good agreement has been found.

The ablation rate of TESPEL has been simulated according to the impurity ablation model described in section 4.3. In this simulation, the sublimation energy of polystyrene was taken as $\varepsilon_{PS} = 1.0$ eV and the attenuation factor $\eta_{PS} = 0.4$. Experimental information was used for the TESPEL velocity and dimensions, as well as for the plasma temperature and density profiles measured by Thomson scattering [53]. The calculated ablation rate is compared with the experimental dependence in Fig. 48 a) (plotted as dashed curve). Due to the low sublimation energy of polystyrene, the ablation process can also be approximated with gas dynamics ablation model [48], which is applicable for a hydrogen pellet. The result of this calculation is shown as dotted curve in Fig. 48 a). It is seen, that both models give close values for the deposition location, although the time dependence of the ablation rate of the shell is reproduced better by the impurity ablation model.

Comparison of the simulated deposition location (defined as a radial position of the center of the region where 80% of tracer is ablated) and deposition width (defined as the width of that region) with the experimental data is summarized in Fig. 49. Parameters of the corresponding discharges and TESPEL dimensions are presented in Table 1.

Table 1. Parameters of a series of the discharges with TESPEL injection.

Shot №	R_{ax}, cm	B_z, T	a_l, cm	$T_e(0)$, eV	$n_e(0)$, 10^{13} cm^{-3}	Pellet velocity, m/s	TESPEL diameter, μm	tracer diameter, μm
72260	94.9	1.5	25.0	430	2.0	246	300	40
72262	94.9	1.5	25.0	440	1.9	245	280	40
72278	92.1	1.5	25.0	470	1.2	186	260	40
72280	92.1	1.5	25.0	440	1.6	148	245	40
72286	94.9	1.5	25.0	450	1.3	238	290	55
72296	94.9	0.9	27.5	290	0.9	298	270	45
72311	97.4	1.3	30.5	280	1.8	161	220	20
72315	97.4	1.3	30.0	300	1.4	113	280	25
72316	97.4	1.3	29.0	390	1.3	212	300	70
72318	99.5	0.9	29.0	300	1.1	232	290	50
72320	99.5	0.9	29.0	360	1.1	151	230	10

The vertical error bars in Fig. 49 correspond to the inaccuracy in the measurements of plasma temperature and density profiles. It is seen that the used ablation model for impurity pellet describes the experimental data rather well, within the mentioned above accuracy.

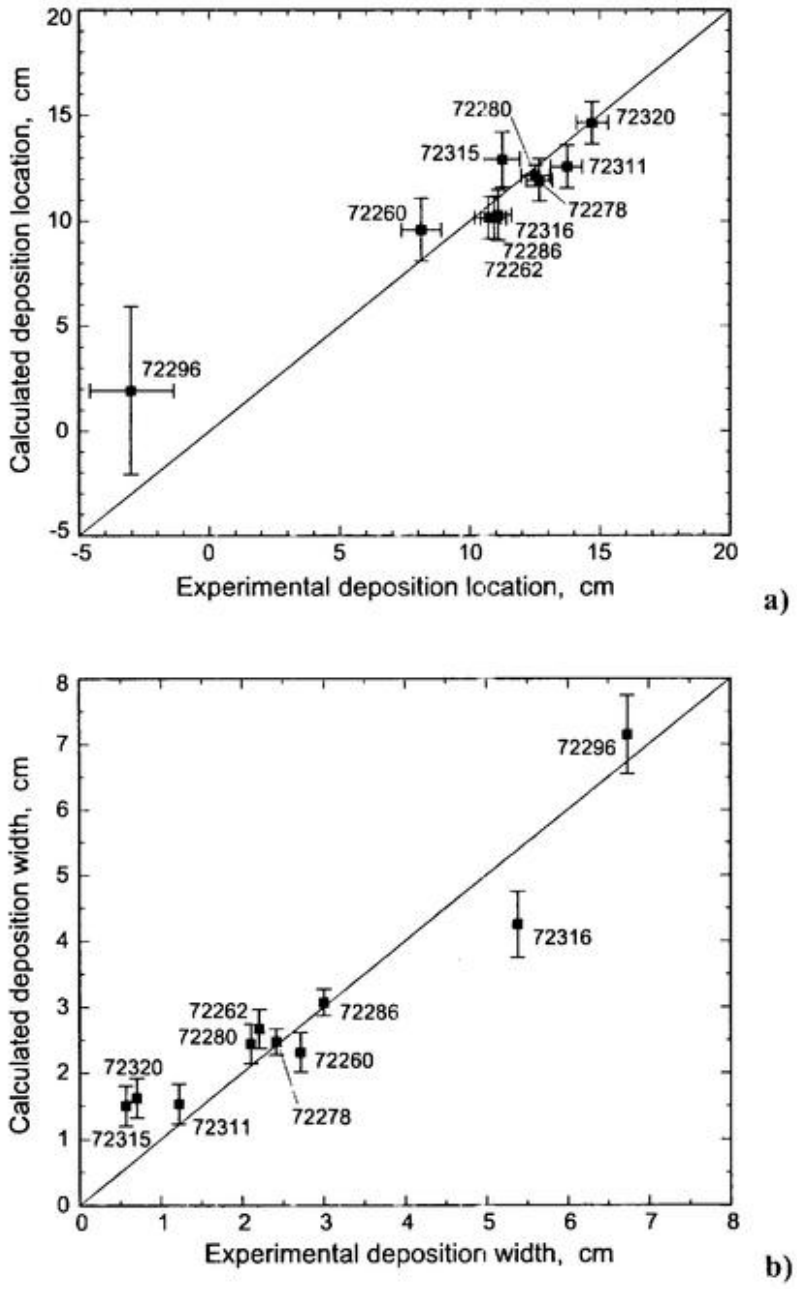

Fig. 49. Comparison of the simulated deposition location (a) and deposition width (b) with the experimental data obtained from photo-multipliers' signals for several shots.

5.5.2. Diffusion of tracer particles

A typical signal of Li III (449.9 nm) emission observed by CXRS at the location of NBI path and the corresponding reference signal are shown in Fig. 50 in the case of $R_{ax} = 94.9$ cm and $B = 1.5$ T. The signals coincide during the RF heating, and some small difference is seen during the NBI phase before the TESPEL injection. After the injection, an apparent difference of Li III intensities is observed. Furthermore, it should be noticed that a clear drop of CXRS signal appears when NBI is turned off, and the signal becomes again equal to the reference one. This fact confirms that the difference between the two signals is due to the Li III emission originated from the charge-exchange reaction.

One example of the CXRS signals of Li III emission subtracted by the reference signals is presented in Fig. 51 in the case of $R_{ax} = 99.5$ cm and $B = 1.5$ T. There are five signals corresponding to the different radial positions indicated by r/a values. The short spike (less than 1 ms duration) right after injection is attributed to the ablation phase of the pellet, when a dense group of the Li^{2+} ions is diffusing along the magnetic field lines before being ionized. In the later phase, each signal achieves a maximal value at the time indicated by horizontal error bars in Fig. 51. As shown with

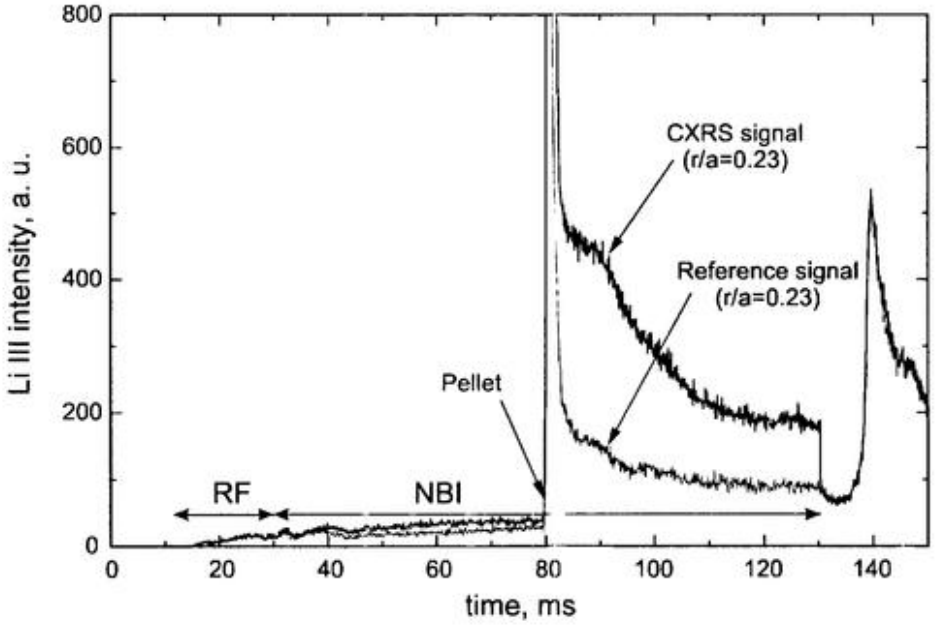

Fig. 50. One example of signals of Li III emission near the tracer-deposited radial position ($r/a = 0.23$) at the location of NBI (CXRS signal) and at the reference location.

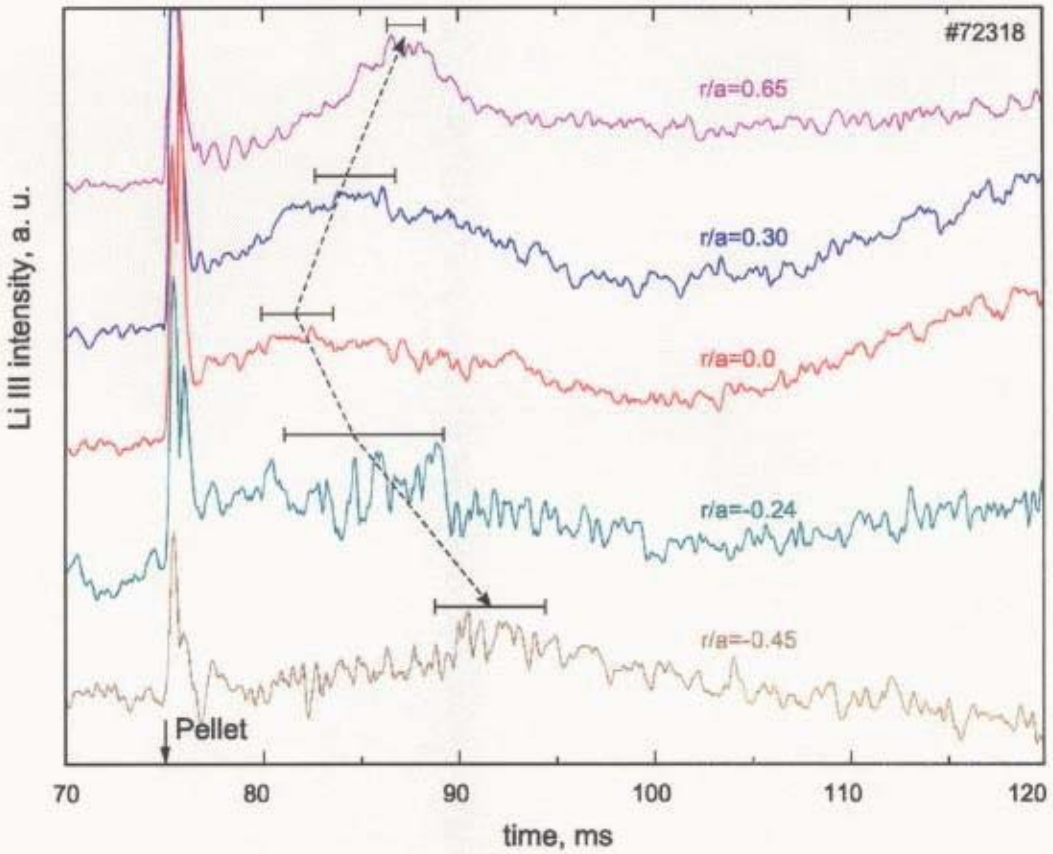

Fig. 51. Li III CXRS signal subtracted by reference signals at different radial positions. Horizontal error bars indicate the time of achieving maximal intensity.

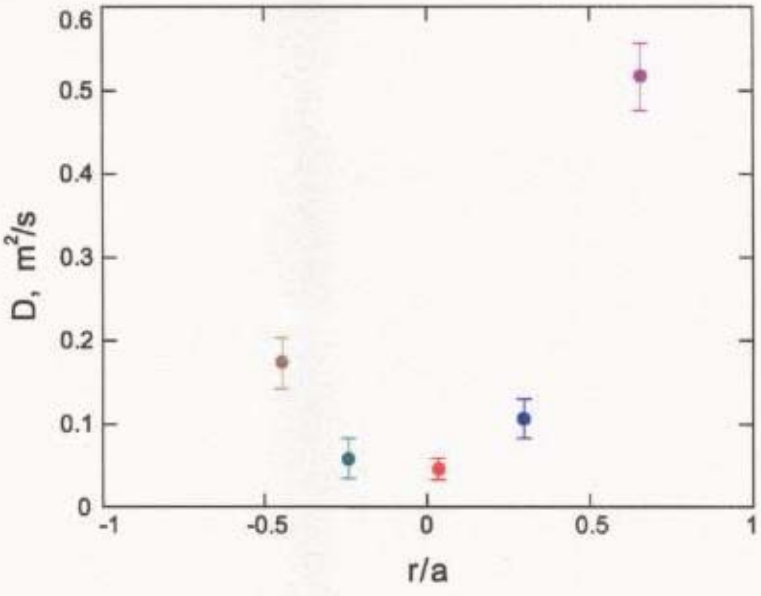

Fig. 52. Diffusion coefficient D at different radial positions calculated from the signals of Li III intensity. Error bars here correspond to the horizontal error bars in Fig. 51.

two arrows, this maximum appears later for the outer radii, which corresponds properly to the calculation made in Section 1.4. From the observed time delays of these maximums it is possible to estimate the diffusion coefficient D at different radii (See Eq. (1.42)), for the tracer deposition location $r_0 \approx$ 3 cm and deposition width $\Delta r \approx$ 2 cm. The result of this calculation is shown in Fig. 52. It is seen that the diffusion coefficient is smaller in the center and increases with r, which is a very typical behavior for the case of anomalous transport.

The procedure of calculation of D by this time-of-maximum method has been applied for the data obtained in various configurations of CHS plasmas. The summary of these calculations is presented in Fig. 53, which includes the data of the diffusion coefficient for different values of major radius R_{ax} and toroidal field B_z. It is seen, that the general behavior of the diffusion, i.e. smaller in the center and larger for the periphery, is maintained for all plasma conditions. A clear difference is observed for the large amount of shots between the case of $R_{ax} = 94.9$ cm, $B_z = 1.5$ T and the case of $R_{ax} = 97.4$ cm, $B_z = 1.5$ T. The D coefficient is larger for the former case and smaller for the latter. At the same time, for the fixed $R_{ax} = 94.9$ cm, the diffusion is

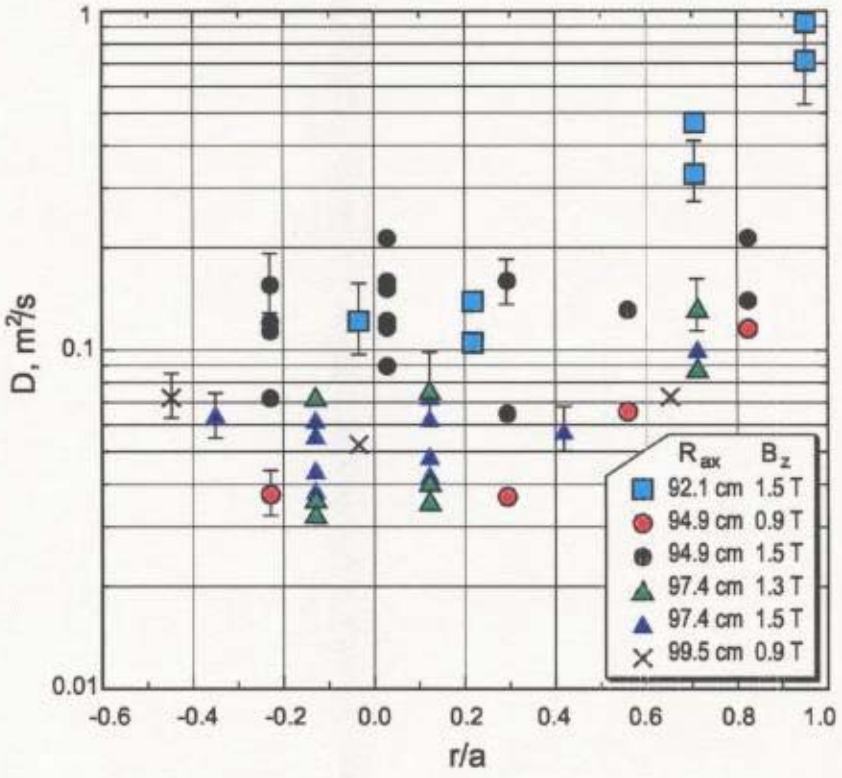

Fig. 53. Values of D are plotted in logarithmic scale versus minor radius using different symbols for different values of major radius R_{ax} and toroidal field B_z (see the legend in the lower-right corner).

smaller for the lower toroidal field (compare B_z = 0.9 T and B_z = 1.5 T). The observed differences can be explained by the different values of the main plasma parameters (such as density and temperature), which are specific for a particular magnetic configuration.

This hypothesis has been tested by studying the dependence of D coefficient on the electron temperature and density (of the post-injection plasma). From the data presented in Fig. 53 only the points belonging to central region (with $-0.3 < r/a < 0.3$) have been selected in order to maintain the similar conditions for all data. As a result, the dependencies presented in Fig. 54 have been obtained. As it is seen from the figure, that for the case of the dependence on the plasma density (Fig. 54 a), no clear tendency can be observed. At the same time, from Fig. 54 b) one can see that larger values of D were measured for the shots with higher electron temperature. Thus, it can be concluded that, for the tested to date range of plasma conditions, the diffusion coefficient depends weakly on the plasma density and increases with the electron temperature. This also corresponds to the widely observed tendency for the heat conductivity χ_e to be increasing with the electron temperature.

Because of the limited accuracy of the measurements of Li^{3+} density achieved for CHS plasma, a more detailed analysis is not appropriate. However, the two main tendencies for D to increase with radius and with electron temperature are clearly observed. Thus, the obtained results have demonstrated the efficiency of the described time-delay method of D measurement for the local transport measurements.

5.5.3. Simulation of the impurity transport

In the calculation above, the velocity of inward pinch V was not taken into account, which can be justified for the initial phase of the diffusion. However, in the longer time scale (as it is seen from Fig. 51), the signals of Li III intensity are slowly increasing in the core region and almost unchanged in the periphery. This corresponds to a gradual peaking of the impurity profile as a whole after the initial perturbation created by TESPEL has become smeared. Such a peaking can be described by including the inward pinch velocity into the consideration. For this reason, the experimental data were simulated by means of the impurity transport code which was employed for the case of pure Li pellet injection, as described in Section 2.7.2.

Result of the simulation is presented in Fig. 55, where simulated curves are overlapped on the experimental signals of Li III intensity at various radii. In this case R_{ax} = 92.1 cm, B = 1.5 T, tracer deposition locati on r_0/a = 0.66, deposition width Δr = 2.3 cm. Diffusion coefficient D and pinch velocity V were adjusted so as to achieve optimal agreement with the experimental data. The best fitting is achieved for

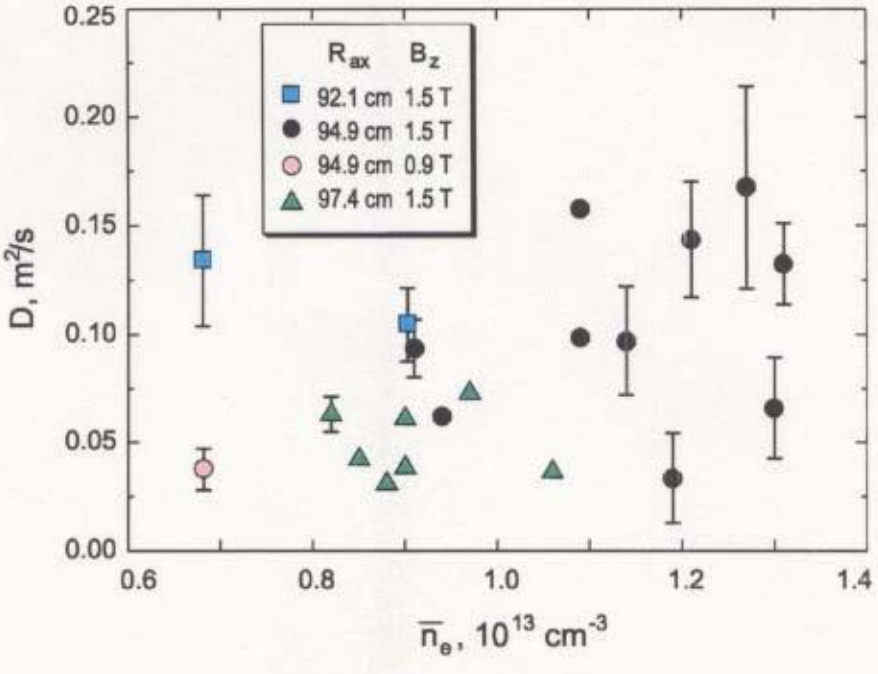

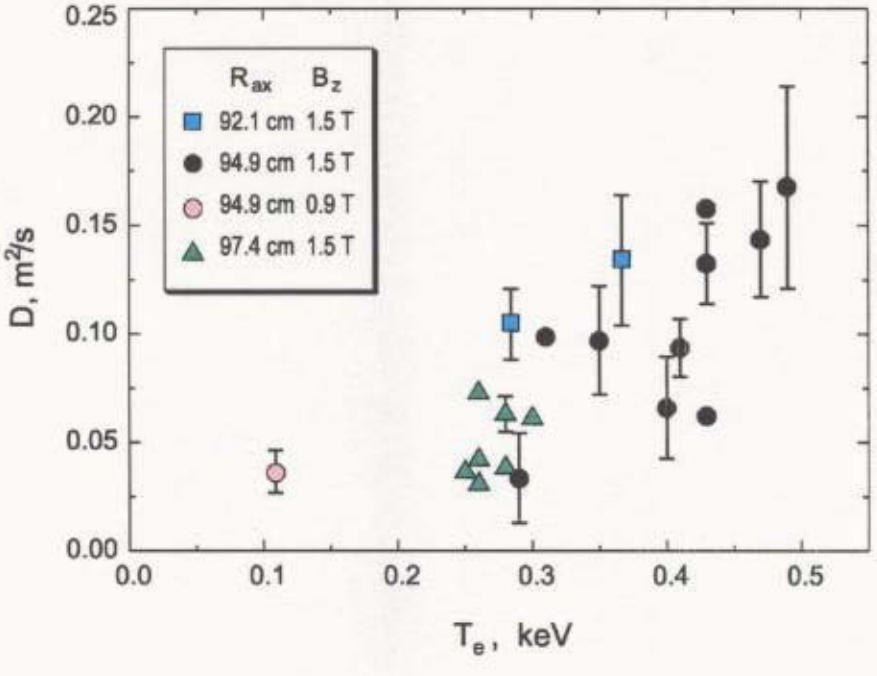

Fig. 54. Dependence of the diffusion coefficient for the central plasma on the plasma density (a) and on the electron temperature (b), for various plasma configurations (see the legends on the plots).

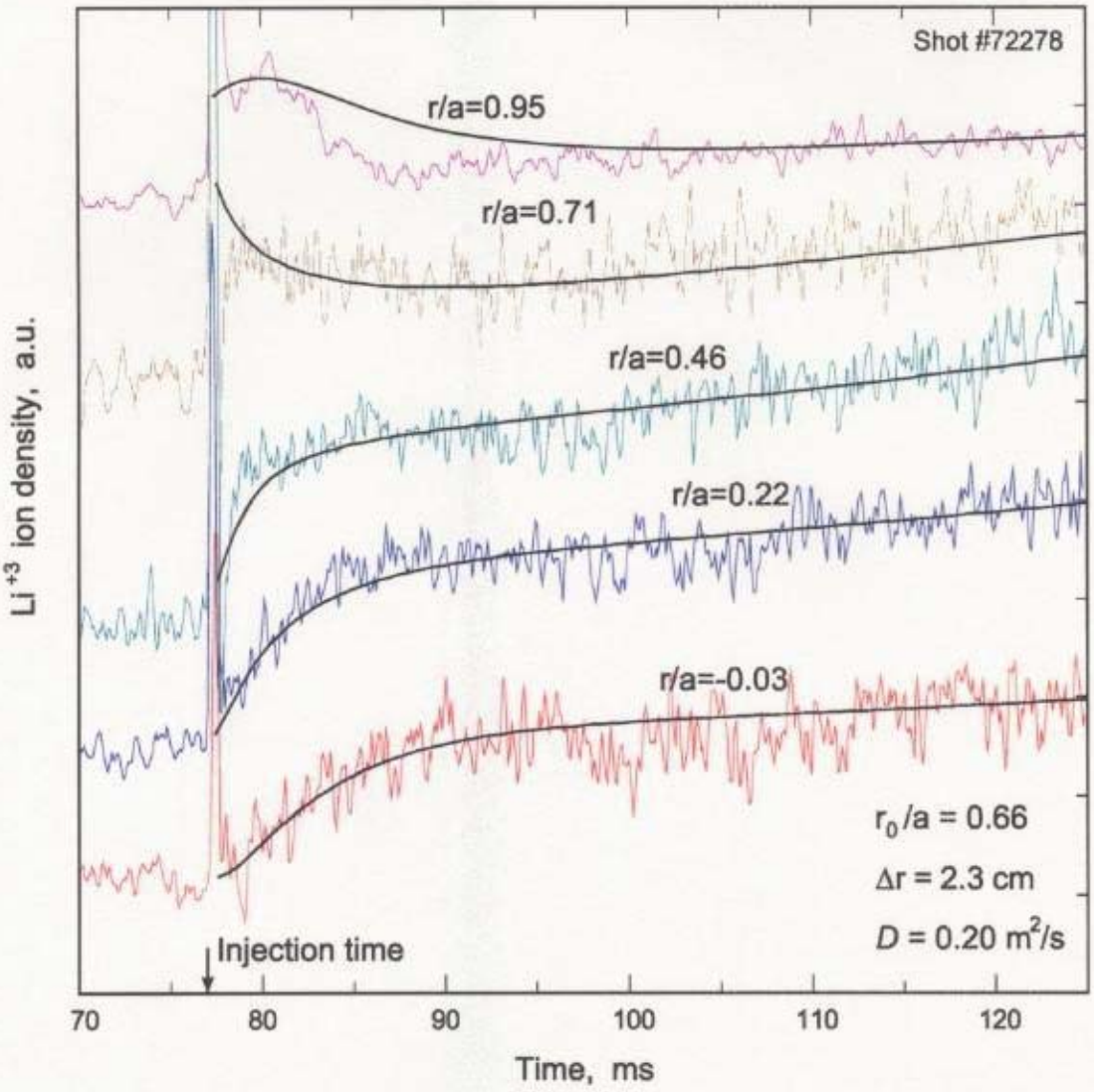

Fig. 55. Comparison of the simulated diffusion of Li^{3+} density (smooth curves) with the experimental data of Li III intensity at different radial positions. TESPEL was injected at $t = 77$ ms.

the average value of $D = 0.19$ m^2/s and $V = 1.0$ m/s, as shown in the Figure. The simulated evolution depends differently on the variation of D and V. The fast transient phase (during first 15–20 ms) is more sensitive to the value of D, while the later phase is affected mainly by the value of V. However, the sensitivity of simulation to the variation of V is rather small and, besides, the later phase of the evolution is affected by other factors, which are difficult to estimate. Thus, the accuracy of the D value obtained by the simulation is higher than that of the V value.

It is seen from Fig. 55, that the experimental behavior is simulated fairly good for all radii, except for the outermost chord with $r/a = 0.95$. The experimentally observed

diffusion is faster at that location than the simulated one. This can be explained by a faster transport at the plasma periphery comparing to the central region, which was also demonstrated by the data presented in Fig. 52.

It should be noted that the values of D and V obtained from the simulation contain a certain error, which is originated mainly from the low signal/noise ratio of the Li III data. The error of the method itself should be much smaller, as the calculations involved in this method do not require an account of many factors such as the particle source, electron density balance and others. The efficiency of the method can be further improved by increasing the S/N ratio, which can be achieved by TESPEL injection into plasma of a larger scale:

1) Higher temperature provides good localization even for a larger size of the tracer;
2) Higher NBI density increases Li^{2+} production rate;
3) Area of CXRS light collection can be enlarged with conservation of the relative dimensions.

5.6. Summary

In this chapter we have described the first experiments with TESPEL injection as a new diagnostic method for local particle transport study.

The smaller dimensions of a TESPEL and more compact configuration of the injector comparing to a cryogenic system have made the injection possible for a medium size plasma device, such as CHS. The light emission from the ablating pellet was measured in H_α and L I (or Li II) lines simultaneously with high time resolution. The pellet cloud was also photographed through H_α and Li I (or Li II) filters by CCD cameras from two directions. From the measured TESPEL ablation rate, the information was obtained about the exact location and width of the deposition of tracer material, and this confirmed that a good localization of the tracer has been achieved. The obtained experimental data were compared with the calculation based on the impurity pellet ablation model, and a good agreement has been found.

The behavior of the tracer ions deposited locally in the core plasma region was observed by CXRS method with high time resolution. The heating neutral beam was used as a source of neutral atoms for the charge-exchange reaction with Li ions. The produced Li III emission is observed at five different radial positions at the location of NBI and at five corresponding positions without NBI. The difference between two signals in each pair appears only during NBI, which confirms that the subtracted signals represent the Li III light produced by the charge-exchange reaction. With this system the diffusion of Li ions has been observed and found to be consistent with the calculation made in Section 1.4 for a localized origin of the perturbation. This made

possible the calculation of the diffusion coefficient D directly from the experimental data at several radial positions. With this method, the coefficient D has been calculated for different plasma configurations and the observed tendencies have been discussed.

For a more accurate calculation of the transport coefficients including the pinch velocity V, the experimental data were simulated by means of the impurity transport code. With this simulation, the experimental curves are reproduced satisfactorily, within the accuracy of the measurements. It is expected that a higher accuracy will be achieved for the case of TESPEL injection into a larger scale plasma.

Thus, a new diagnostic method for particle transport study with TESPEL has been experimentally implemented for the first time. The results from CHS have proved the new diagnostic concept from the both viewpoints of the production method of a tracer-encapsulated pellet and observation of the transport properties of the tracer particles.

6. CONCLUSIONS

This work was devoted to the impurity transport study in plasmas by means of the pellet injection. Several methods of the particle transport diagnostics have been described and tested experimentally, including the tracer-encapsulated pellet injection. The main results of the present work can be summarized as follows:

1) High purity lithium pellets have been injected into Heliotron E plasmas in order to measure the ablation properties of a Li pellet, to analyze the Li ions transport, and to study the plasma conditioning by Li coating on the wall. A substantial increase of the stored plasma energy has been found to take place after the injection. The main characteristics of the Li ions during the pellet ablation have been measured. The subsequent transport motion of Li ions has been simulated by means of the impurity transport code, and the diffusion coefficient D and the pinch velocity V have been calculated.

2) For the accurate measurement of the particle transport, the concept of TECPEL (tracer-encapsulated cryogenic pellet) injection has been proposed. The method of analytical calculation of the diffusion coefficient D has been described, which allows obtaining D directly from the experimentally observed density evolution of the tracer deposited by TECPEL in a limited plasma volume.

3) A device for production and acceleration of the TECPEL has been constructed and tested experimentally. The 3D geometry of TECPEL has been reconstructed from the pellet photography and found to be consistent with the projected dimensions. Thus, the proof-of-principle of the device operation has been successfully demonstrated.

4) For application to a medium scale plasma, the concept of tracer-encapsulated solid pellet (TESPEL) has been developed. From various TESPEL configurations tested, the most appropriate one has been selected in the form of a polystyrene shell containing a lithium hydride core. This configuration has been experimentally realized and the produced TESPELs have been successfully accelerated with conservation of the TESPEL's integrity.

5) A series of experiments with TESPEL injection has been carried out for the case of CHS plasmas. The measured location and width of the tracer deposition are in a good agreement with the calculations by impurity ablation model. It was demonstrated that the current TESPEL configuration allows achieving the necessary localization of the tracer material in CHS plasmas.

6) Diffusion of the tracer ions was observed by CXRS and found to be consistent with the calculations. From these data, the diffusion coefficient D has been determined at several radial positions for various plasma configurations. A more accurate calculation of D and pinch velocity V has been achieved by simulation with the impurity transport code.

The results of this work has proved the advantages of a new method of the local particle transport study by means of the tracer-encapsulated pellet injection. The first successful experimental implementation of the new method allows a definite conclusion about the feasibility of the tracer-encapsulated pellet injection as a new diagnostic concept for analyzing the transport properties of fusion plasmas.

ACKNOWLEDGEMENTS

I owe a debt of gratitude to my family that has been supporting my spirit through the years and giving me the energy to continue my scientific work.

I would like to express my gratefulness to Prof. S. Sudo, who made my participation in this research program possible and whose help and cooperation during these years have been invaluable. I wish also to thank Director-General A. Iiyoshi for continuous encouragement to this work.

The experiments with lithium pellet injection have been carried out in Kyoto University. I would like to thank the group of Heliotron E for the collaboration and help in the experiments, and in particular, K. Kondo, H. Zushi, T. Mizuuchi, K. Nagasaki and K. Sakamoto.

The injector of TECPEL was produced mainly by Nippon Sanso, Corp., and I express my thanks especially to H. Itoh for his cooperation and for the h elpful experience in the injector operation. I also acknowledge S. Goto of Torisha, Corp. for the lithium pellet injector design and, from NIFS, S. Kato and S. Mizusawa for the technical support in the overall experiments.

My thanks are also extended to the group of CHS device for the support to our experiments. Particularly, I would like to thank K. Matsuoka, S. Okamura, S. Nishimura, M. Isobe, S. Kado, T. Minami, S. Morita, I. Nomura, R. Pavlichenko, C. Takahashi.

I am grateful to M. Takagi and T. Norimatsu of Osaka Laser Fusion Institute for the help on the shell fabrication and for providing the necessary equipment and materials for the TESPEL production.

I wish to thank T. Amano who kindly provided the numerical code used in the simulations and participated in the useful discussions. I am also grateful to T. Kato and I. Murakami for supplying the necessary atomic data.

My sincere thanks are addressed to V. G. Kapralov and I. V. Viniar from St. Petersburg Technical University for their help in preparation of experiments on CHS and for their priceless experience which they generously shared with me. The fruitful discussions with B. V. Kuteev and V. Yu. Sergeev are kindly appreciated.

I am indebted to C. Namba, B. Peterson and many others who helped me as a foreigner to survive in Japan and to solve various problems.

This work was supported partly by the grant № 10026 of Daiko Foundation. The financial support of the Ministry of Education of Japan is gratefully acknowledged.

REFERENCES

[1] F. L. Hinton, R. D. Hazeltine, Rev. Mod. Phys. **48**, 239 (1976).

[2] P. P. Lallia, P. H. Rebut, Preprint JET-IR(89)08, July (1989).

[3] Yu. N. Dnestrovsky, D. P. Kostomarov, Mathematical Modeling of Plasma (in Russian), 2nd edition, Moscow - Nauka, (1993).

[4] M. Soler, J. D. Callen, Nuclear Fusion **19**, 703 (1979).

[5] J. D. Callen, G. L. Jahns, Phys. Rev. Letters **38**, 491 (1977).

[6] G. L. Jahns, M. Soler, B. V. Waddell *et al.*, Nuclear Fusion **18**, 609 (1978).

[7] E. D. Fredrickson, J. D. Callen, K. McGuire *et al.*, Princeton, Preprint PPL-2255 (1986).

[8] A. A. Bagdasarov, N. L. Vasin, S. V. Neudatchin *et al.*, In proc. of 13th International Conf. on Pl. Phys. and Contr. Nucl. Fus. Research, Washington, 1-6 October 1990, IAEA-CN-53/A-7-5-2.

[9] T-10 group of Kurchatov Institute of Atomic Energy, Plasma Phys. **22**, (1986).

[10] G. L. Jahns, S. K. Wong, R. Prater *et al.*, Nucl. Fus. **26**, 226 (1986).

[11] A. A. Bagdasarov, S. M. Egorov, B. V. Kuteev *et al.* Sov. J. Fizika Plasmy (in Russian) **13**, 781 (1987).

[12] W. J. Goedneer, Nuclear Fusion **26**, 1043 (1986).

[13] E. S. Marmar, J. L. Terry, Rev. Sci. Instrum. **61**, 3081 (1990).

[14] S. K. Combs, Rev. Sci. Instrum. **64**, 1679 (1993).

[15] V. G. Kapralov, K. V. Khlopenkov, B. V. Kuteev, M. L. Svoiskaya. Intern. school on Plasma Physics. Local Transport Studies in Fusion Plasmas. Editors J. D. Callen, G. Gorini, E. Sindoni, SIF, Bologna, 169 (1993).

[16] V. G. Kapralov, B. V. Kuteev, M. A. Parshin *et al.* In Controlled Fusion and Plasma Physics (Proc. 18th Eur. Conf. Berlin. 1991) **15A**, Part 1, European Physical Society, 345 (1991).

[17] H. Kaneko, K. Kondo, O. Motojima *et al.*, Nuclear Fusion **27**, 1075 (1987).

[18] B. V. Kuteev, P. T. Lang, S. Sudo *et al.*, Fusion technology **26**, 938 (1994).

[19] K. V. Khlopenkov, V. Yu. Sergeev, S. Sudo *et al.*, Fusion Engineering and Design **34-35**, 337 (1997).

[20] M. Wakatani and S. Sudo, Plasma Phys. Control. Fusion **38**, 937 (1996).

[21] S. Itoh and K. Itoh, Jpn. J. Appl. Phys. **26**, L1338 (1987).

[22] S. Sudo, J. Plasma Fusion Res. **69**, 1349 (1993).

[23] D. L. Jassby, D. R. Cohn, R. R. Parker, Nucl. Fusion **16**, 1045 (1976).

[24] H. Sugai *et al.*, J. of Nucl. Mater. **220-222**, 254 (1995).

[25] J. D. Strachan *et al.*, J. of Nucl. Mater. **217**, 145 (1994).

[26] G. W. Barnes, R. C. Gemhardt, D. Mansfield, "Operation of the Lithium Pellet Injector during D-T operations on TFTR", Symposium on Fusion Engineering, Illinois, Abstract 0605, p. 176 (1995).

[27] K. Kondo, T. Mizuuchi *et al.*, J. Nucl. Mater. **220-222**, 1052 (1995).

[28] K. Kondo, K. Ida, C. Christou *et al.*, J. Nucl. Mater. **241-243**, 956 (1997).

[29] T. Kato, K. Masai and M. Arnaud, National Institute for Fusion Science Research Report NIFS-DATA-14, Japan (1991).

[30] S. Sudo, K. Kondo, H. Zushi *et al.*, In Proc. of 21st EPS Conf. On Controlled Fusion and Plasma Physics. Montpellier, France, Part III, p. 1546 (1994).

[31] P. B. Parks, R. J. Turnbull and C. A. Foster, Nucl. Fusion **17**, 539 (1977).

[32] B. V. Kuteev, V. Yu. Sergeev, and L. D. Tsendin, Sov. J. Plasma Phys. **10**, 675 (1984).

[33] V. Yu. Sergeev *et al.*, National Institute for Fusion Science Research Report NIFS-428, Japan (1996).

[34] T. Amano, J. Mizuno and M. Kako, National Institute for Fusion Science Research Report IPPJ-616, Japan (1982).

[35] A. Iiyoshi, M. Fujiwara, O. Motojima *et al.*, Fusion Technology **17**, 169 (1990).

[36] S. L. Milora, *et al.*, Fusion Engeneering (Proc. 14th IEEE Symp. San Diego, 1991), v. 2, IEEE, New York, p. 716 (1991).

[37] I. Viniar and S. Sudo, Rev. Sci. Instrum., **68**, 1444 (1997).

[38] A. A. Lovtsyus, V. G. Kapralov, K. V. Khlopenkov et al., Rus. J. Questions of Atomic Science and Technology, Moscow, **1-2**, 53 (1993).

[39] I. Viniar et al. Rus. J. Techn. Phys., **65**, 167 (1995).

[40] M. Kanno, *et al.*, Pellet Injection and Toroidal Confinement (Proc. Tech. Comm. Mtg, Gut Ising, 1988), IAEA-TECDOC-534, IAEA, Vienna, p. 1721 (1989).

[41] K. Kawasaki, *et al.*, Fusion Technology (Proc. 15th Symp. Utrecht, 1988, v. 1, North-Holland, Amsterdam, p. 724 (1989).

[42] S. Sudo, H. Itoh, K. Khlopenkov, Rev. Sci. Inst. **68**, 2717 (1997).

[43] I. V. Miroshnikov, *et al.*, Nucl. Fusion **32**, 2025 (1992).

[44] R. D. Durst, *et al.*, Nucl. Fusion **30**, 3 (1990).

[45] M. Takagi, T. Norimatsu, T. Yamanaka, and S. Nakai, J. Vac. Sci. Technol. A, **9**, 2145 (1991).

[46] M. Takagi and T. Norimatsu, Annual Progress Report, Institute of Laser Engineering, Osaka Univ., 209 (1996).

[47] K. Matsuoka, S. Kubo, M. Hosokawa *et al.*, Proc. 12th *Inter. Conf. on Plasma Physics and Control led Nucl ear Fu sion Research* (IAEA, Vienna, 1989) **2**, p. 411 (1998).

[48] P. B. Parks and R. J. Turnbull, Phys. Fluids, **21**, 1735 (1978).

[49] J. Dean, Lange's Handbook of Chemistry, McGraw Hill, Inc., 14th edition, p. 6.117 (1992).

[50] S. Okamura, K. Matsuoka *et al.*, Proc. 17th *Inter. Conf. on Plasma Physics and Controlled Nuclear Fusion Research* (IAEA, Yokogama, 1998).

[51] K. Ida *et al.*, Rev. Sci. Instrum., **60**, 867 (1989).

[52] K. Ida *et al.*, Phys. Rev. Lett., **76**, 1268 (1996).

[53] K. Narihara *et al.*, Rev. Sci. Instrum. **66**, 4607 (1995).

[54] H. Ryufuku, JAERI Memo-82-031, Japan Atomic Energy Institute (1982).

APPENDIX

A. Absolute calibration of the CXRS measurements.

For the present purpose of calculating the transport coefficients from the observed evolution of the Li^{3+} ions density, the absolute value of the density is not required. However, in order to verify that the level of the observed LiIII intensity corresponds to the rate of the charge-exchange reaction, and thus to ensure that our observation method is correct, it is necessary to perform the absolute calibration of experimental measurements made with the photo-multipliers and then compare the result with the theoretical estimation.

Calibration with standard lamp.

The typical device used for the absolute calibration of the light intensity is the standard lamp with the known radiation in a given wavelength range. In our experiments we used a standard lamp № EPT-1297 with the working body of a tungsten ribbon filament heated by electric current. In the wavelength range of 450 nm (Li III line) the spectral radiance of the lamp operated at 38.00 amperes D.C. is given as

$$N_\lambda = 4.614 \cdot 10^{14} \text{ photon} / \text{cm}^2 \cdot \text{Å} \cdot \text{sr} \cdot \text{s} \qquad \text{(A.1)}$$

The radiant flux P, in photons per second which enters the detector is computed from the formula:

$$P = R\, N_\lambda\, s\, A / D^2 \qquad \text{(A.2)}$$

where R is the reflectance of the combination of mirrors used, s is the area of the radiating filament, A is the sensitive area of the detector, and D is the distance of the detector from the lamp (See Fig. 56).

The detector used consists of the lens and the opening of the optical fiber. The lens is located at the focal length distance from fiber, and is specified to collect the light from the parallel beam of 7 mm diameter. However, there should certainly be the maximal angle δ of divergence of the light from the parallel direction, which is

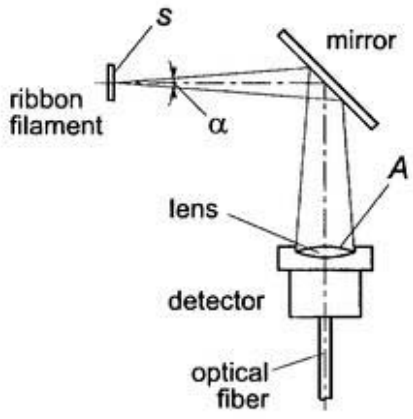

Fig. 56. Optical layout of the calibration with the standard lamp.

collected by the lens and enters the fiber. This divergence angle has been measured with a simple optical setup including a point light target made by a He-Ne laser. The value obtained for δ is 1.6° (full angle), which is larger than the angle $\alpha = 0.8°$ (from the lens diameter of 7 mm and $D = 500$ mm). This means that for the layout shown in Fig. 56, all the light falling on the detector lens is lying within the maximal divergence angle δ, and thus, enters the optical fiber.

The reflectance R of the mirror can be obtained from a series of three measurements using two different mirrors: $P_1 = R_1 N$ (mirror R_1 used), $P_2 = R_2 N$ (mirror R_2 used), and $P_3 = R_1 R_2 N$ (both mirrors used). From these relations it is easy to obtain: $R_1 = P_3 / P_2$ and $R_2 = P_3 / P_1$. For example, the mirror used in the calibration had $R = 0.887$.

The Li III optical filters used in the experiments had an average bandwidth of 1.00±0.04 nm and peak transmission at $\lambda = 449.9$ nm of 50±4%. This gives the value for W of about 5.0 Å.

The area of the radiating filament was limited by a circular aperture with diameter of 1.2 mm, from which the value for s is calculated as 1.131 mm^2.

In order to reduce the light intensity of the standard lamp and to imitate the level of the real light from the plasma, a set of three neutral density filters was used (total attenuation $F = 0.2 \cdot 0.15 \cdot 0.15 = 4.5 \cdot 10^{-3}$).

Taking into account all these parameters, the typical level of the radiant flu measured in the experiments is

$$P_{exper} = 1.6 \cdot 10^7 \text{ photon/s} \qquad (A.3)$$

It is worth mentioning that the high time resolution of the photo-multipliers allows observation of discrete photons with the average rate of about 1-3 photons per microsecond. This level agrees with the above value of P, if the photo-multiplier efficiency (10-20%) and the losses in the lens-fiber couplings are taken into account.

Comparison of calibration results with theory.

The radiant flux originated from the charge-exchange reaction can be calculated as follows. From the typical NBI power at CHS is 600–700 kW and the operating voltage of 36 kV, one can obtain the equivalent current as 16.7–19.4 A. Assuming the elliptical form of cross section of the neutral beam with half-axes of $a = 5$ and $b = 10$ cm, the equivalent flux density of neutral atoms is calculated as $3.3–5.4 \cdot 10^{17}$ $cm^{-2} \cdot sec^{-1}$.

The density of the Li^{3+} ions in plasma is estimated as $2.6–8.7 \cdot 10^9$ cm^{-3} for the LiH tracer diameter of 0.04–0.06 mm. The theoretical data on the c ross-section of the reaction

$$Li^{3+} + H^0 \rightarrow Li^{2+}(5g \rightarrow 4f) + H^+ + h\nu \quad (\lambda = 449.9\ \text{nm}) \tag{A.4}$$

is given by Ryufuku [54] as $2 \cdot 10^{-17}$ cm^2 for the beam energy range of 30–50 keV.

With these data, the rate of the charge-exchange reaction can be estimated as

$$S_{CXR} = 1.7 - 9.5 \cdot 10^{10}\ \text{cm}^{-3} \cdot \text{s}^{-1} \tag{A.5}$$

The resulting radiant flux from the plasma can be calculated as

$$P_{theor} = S_{CXR} V \gamma F \tag{A.6}$$

where V is the observable plasma volume, γ is the solid angle for collected light, and F is the attenuation by the Li III filter (equals 0.5).

The value of V is estimated as 9.2–12.2 cm^3 (from D = 50 cm, $\alpha = 0.8°$, height of the neutral beam along the observation line of 6–8 cm). The value of γ is obtained from the detector diameter (7 mm) and D as $1.54 \cdot 10^{-4}$ sr. From these, one can finally obtain:

$$P_{theor} = 1.2 - 8.9 \cdot 10^{7}\ \text{s}^{-1} \tag{A.7}$$

Comparing this result with the value in Eq. (A.3), we can conclude that the level of the Li III intensity measured experimentally lies within the range predicted by the theory.

B. Improvement of the TESPEL production routine.

It was shown in Section 4.3 that the sublimation energy for polystyrene is relatively low, which enhances the ablation and may make difficult achieving a deep penetration of the TESPEL into plasma if the pellet velocity is low. On the other hand, the shell ablation time can be prolonged using the shells with larger thickness and smaller diameter (for minimizing the perturbation to the background plasma).

For example, a shell with diameter of 350 μm and wall thickness of 50 μm has approximately the same amount of atoms as the one with 300 μm diameter and 125 μm wall thickness, but the ablation time is significantly longer for the latter.

Such a "shell" has the inner diameter of 50 μm which is equal to the tracer diameter. It can be produced from a solid polystyrene sphere by drilling a vertical channel of 50 μm diameter until the level of 25 μm below the center of the sphere. The process is clarified in Fig. 57. At the final stage, the channel is closed by a segment of a 50 μm polystyrene thread and moistened by toluene. With this configuration of the TESPEL, a better uniformity of the shell thickness can be achieved, which results in deeper penetration of the TESPEL and higher localization of the deposited tracer.

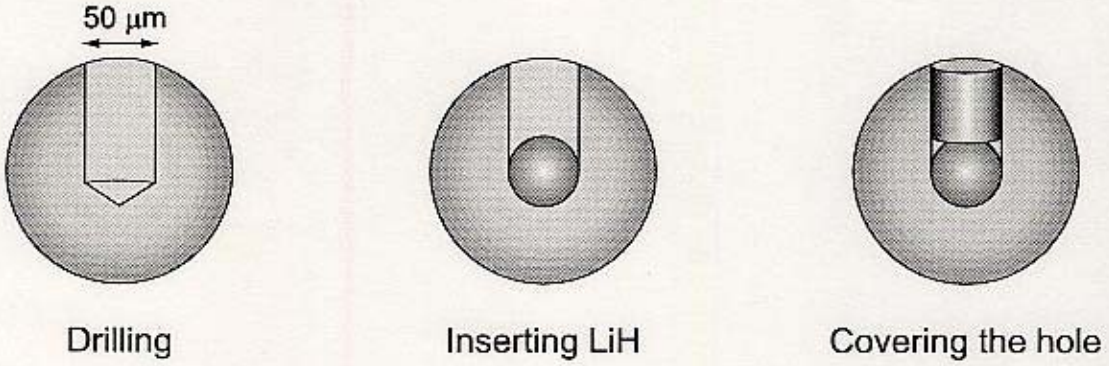

Fig. 57. Alternative process for TESPEL production.